Title
Interfacial Engineering of Nanoscale LiCoO2 for Lithium Ion Batteries

Author
Dahl, Spencer Zosel

Publication Date
2022

Peer reviewed|Thesis/dissertation

Interfacial Engineering of Nanoscale $LiCoO_2$ for Lithium Ion Batteries

By

SPENCER DAHL
DISSERTATION

Submitted in partial satisfaction of the requirements for the degree of

DOCTOR OF PHILOSOPHY

in

Chemical Engineering

in the

OFFICE OF GRADUATE STUDIES

of the

UNIVERSITY OF CALIFORNIA

DAVIS

Approved:

Ricardo H. R. Castro, Chair

Blas P. Uberuaga

Sabyasachi Sen

Committee in Charge

2022

Table of Contents

Abstract

Lithium ion batteries are a critical part of the energy storage infrastructure and their utilization has expanded significantly over the past few decades. Batteries have improved greatly over that time; however, capacity, electrochemical performance, and charge/discharge rates are still insufficient for the growing energy needs. Nanoscale materials provide some enhancement in these areas due to the shorter diffusion path lengths and increased rates of lithium intercalation. Coarsening of nanomaterials during processing and operation is one of the critical problems for the implementation of novel technologies based on 'nanoscale' effects. In the context of batteries, nanomaterials inherently come with benefits, but also excess interfacial energies that cause parasitic reactions, intergranular cracking, and high surface reactivity that lead to accelerated cathode degradation. Additionally, the excess energies cause coarsening during the manufacturing of the nanoparticles as well as during battery operation through cycle induced coarsening.

This work studied nanoscale $LiCoO_2$ (LCO) particles to help improve the overall interfacial stability through dopant segregation. Currently, dopant selection can be an arduous experimental process to select the best dopant for segregation and lowering the interfacial energies. Molecular static calculations were used to screen a variety of dopants with differing ionic sizes and oxidations states. The simulations demonstrated a clear trend of increasing segregation energy with size and oxidation state for two surface planes, {001} and {104}, and two grain boundary structures, Sigma 3 and Sigma 5. From the model, lanthanum exhibited strong segregation to all interfaces and was selected as the best candidate for experimental synthesis.

La-doped LCO and undoped LCO nanoparticles were synthesized through a hydrothermal synthesis method and produced nanoplatelet layered structures of LCO. STEM-EELS was used to confirm the presence of segregated La to grain boundaries and surfaces of the nanoplatelet morphology. Calorimetric sintering studies revealed that the La segregation lowers the average surface energy of the particles. The La also inhibited coarsening and grain growth in the nanoparticles during sintering resulting in doped nanoparticles with high surface areas and smaller crystallite sizes. In addition, water adsorption microcalorimetry was used to study chemically delithiated structures of the LCO particles. Water adsorption showed that delithiation results in a decrease of surface energy in the undoped particles, but the La stabilizes the surface energy of the nanoparticle. These results demonstrate a computational and thermodynamic framework for improving the interfacial stability of nanoscale cathode materials and could be used to optimize morphology of particles for battery operation.

Acknowledgement

I would like to give a very important acknowledgement to Professor Ricardo Castro for being an exceptional mentor and major professor during my PhD. His support in my research activities was crucial in my successful completion of the degree and the examinations. Although he was a great research advisor, he also supported me in my personal aspirations and stressed the importance of a positive work life balance. He encouraged collaborations with other groups and went out his way to explore my research interests like atomistic simulations and electrochemistry. Perhaps most importantly, he opened my eyes from a background as a chemical engineer to the world of materials science and engineering to show me the power of ceramic materials. It has been a truly rewarding experience to learn from him about a new field of study and be able to utilize what I have learned as I move forward in my career.

I would also like to thank Professor Sabyasachi Sen and Dr. Blas Uberuaga from Los Alamos National Laboratory for serving on my dissertation committee and for the valuable feedback on my research. Additionally, Blas was a great mentor as I learned about atomistic simulations and how they can inform experimental synthesis and design of nanoparticles. His guidance and patience throughout the process was very much appreciated and I enjoyed collaborating with him throughout my studies. I would also like to thank Dr. Toshihiro Aoki form UC Irvine for the expertise and consultations during our STEM-EELS microscopy sessions. The Center for Nano-Micro Manufacturing and the Advanced Materials Characterization and Testing Laboratory were also integral for the completion of my degree and for in depth training on the microscopy equipment. Lastly, thank you to the National Science Foundation for funding my research over the last four years.

I have to thank all of my lab group members in the Nanoceramics Thermochemistry Laboratory and the Peter A. Rock Thermochemistry Laboratory for helping me work through research issues. I would especially like to thank Dr. Kimiko Nakajima, Dr. Luis Sotelo Martin, Isabella Costa, and Victor Gin He Leong for the fun collaborative environment in the lab. I also greatly enjoyed my research stay at Jülich Forschungszentrum in Germany thanks to the funding from the IIE-GIRE Fellowship and the collaboration with Dr. Olivier Guillon, Dr. Dina Fattakhova-Rohlfing, Dr. Martin Finsterbusch, and Dr. Christoph Roitzheim. The American Ceramics Society was also an incredible resource for networking events and disseminating my research to my colleagues in similar fields. The President's Council of Student Advisors within ACerS was especially helpful in meeting other graduate students in ceramic engineering, growing my leadership skills, and performing outreach activities.

Finally, I want to thank my parents for all the love and support over the years. I especially want to thank my wife and our new son for the patience and support throughout my studies. They inspire me to be a better person and becoming a father while we lived in Davis will ensure it remains a special place in our hearts. Thank you to everyone for your contribution and I am sincerely grateful for all the amazing memories and people I met through UC Davis.

List of Figures

List of Tables

Chapter 1: Introduction and Background

Introduction

Lithium-ion batteries are an integral part of the rechargeable battery industry; however, after decades of use, lithium-ion technology still has several failure mechanisms that lead to performance issues, capacity fading, and overall safety concerns.[1,2] The problems with lithium-based energy storage have hindered the impact of batteries and prevented the technology from having broader impacts on renewable energy, climate change, and lightweight portable energy storage. The lithium-ion battery functions by moving lithium ions from the anode to the cathode during discharging to allow for the flow of electrons through the circuit, as shown in **Figure 1.1**.[3] This intercalation process is heavily dependent upon the structure of the cathode material and the number of active sites for diffusion. As the battery experiences more cycles, the microstructure can change drastically due to instabilities in the delithiated structure and alter the battery's performance.[4] Nanostructured materials can improve some of the performance issues in batteries by decreasing diffusion path lengths and enhancing the charge/discharge rates in cathodes, but also experience many of these degradation mechanisms. Microstructural changes can be caused by high interfacial energies at the surface and grain boundaries of materials, which accelerates the shift to a more thermodynamically favorable state and promotes instabilities like intergranular crack propagation. The interfacial energies can be manipulated through several strategies during the synthesis of materials and this becomes exceedingly important as cathode materials progress into the nanoscale. This project seeks to study the thermodynamics of materials and explores the possibility of manipulating interfacial energies to design ultra-stable nanomaterials, in turn enhancing the electrochemical stability of batteries. Ultra-stable

nanomaterials can result in high energy density for batteries, which leads to light weight energy storage and utilizing more of the theoretical capacity of the battery.

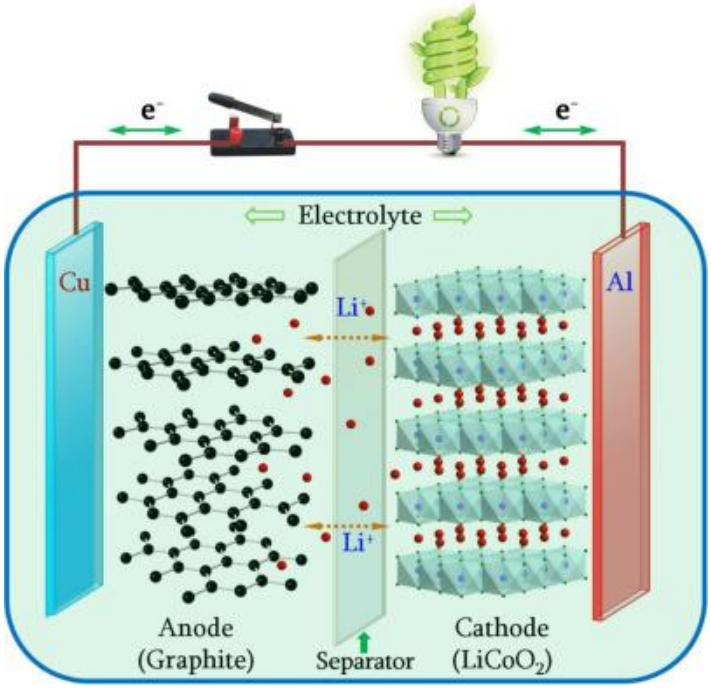

Figure 1.1. Battery schematic illustrating lithium diffusion between the cathode and anode.[3]

Hypothesis

This project hypothesizes that nanomaterials' interfaces can be thermodynamically controlled and manipulated to create ultra-stable nanomaterials for lithium ion battery cathodes. The degradation pathways seen in lithium-ion battery materials are closely correlated to structural changes and surface reactivity. If the surfaces and grain boundaries in nanoparticles can be thermodynamically stabilized, the overall battery performance will improve. In addition, the proposed design of interfaces will hypothetically enhance the stability of delithiated structures existing during battery operation.

Objective 1: Develop an atomistic model for screening dopants to inform dopant selection in nanomaterial synthesis.

Objective 2: Synthesize undoped and doped $LiCoO_2$ nanoparticles and confirm segregation of dopants.

Objective 3: Utilize rare earth element doping and segregation to manipulate interfacial stability of nanoparticles and directly measure interfacial energies.

Objective 4: Delithiate structures and measure the change in interfacial energies as a function of lithium content.

Background

The theory behind utilizing nanomaterials for lithium-ion batteries is rooted in reducing diffusion path lengths for lithium ions and enhancing the surface area by crystallite size reduction. By increasing the specific surface area, the battery has more contact with the electrolyte at the solid electrolyte interface (SEI), cycles faster with fewer transport limitations, and increases the number of surface sites for lithium intercalation.[5]

Beyond batteries, nanomaterials have been reported to improve materials' properties, such as hardness and surface reactivity, due to the high fraction of atoms at or near surfaces.[6,7] A general drawback of nanomaterials is the high fraction of atoms near surfaces, which contributes excess energy to the total energy of a system, differing from larger particles where the large majority of the total energy is in the bulk material.[8,9] Although ceramics typically have low interfacial energies on the order of a few joules per meter squared, the surface area term can drastically increase by several orders of magnitude in nanoparticles to make the surface energy a significant fraction of the total energy. For this work, an interface will be defined as a surface or grain boundary, and consequently, the interfacial energies will refer to the surface energy and grain boundary energy.

Equation 1 shows the influence of the interfacial areas on the total energy G_{sys}, where γ_{SV} and γ_{SS} are the solid-vapor and solid-solid interfacial energies, respectively, and

$$\delta G_{sys} = \delta \int \gamma_{SV}\, dA_{SV} + \delta \int \gamma_{SS}\, dA_{SS} \tag{1}$$

A_{SV} and A_{SS} are the solid-vapor and solid-solid interfacial areas, respectively. High surface energies lead to a more reactive surface that can readily interact with the electrolyte solution, promote intergranular cracking, and facilitate the transition into a new phase as lithium moves to the anode. The literature reports methodologies for reducing interfacial energies through dopant

segregation in order to stabilize ceramic interfaces.[10–12] The reduction of interfacial energies can lead to a reduced driving force for microstructural evolution during synthesis and help maintain the unique properties gained by utilizing nanoscale materials.

Dopant Segregation

Elemental doping will be used to change the interfacial energies by segregating dopants to the interfaces in this project. The main mechanisms driving segregation are captured in a quantity called segregation enthalpy, systematically affected by parameters such as ionic charge, and ionic size differences between the dopant and the host composition. The electrostatic effects on segregation can change based on the valency of the dopant and the specific electronic nature of the grain boundary or surface. The elastic effects due to ionic size impact the diffusion of the dopant and the strain the dopant causes on the lattice.[13] For example, a dopant with a larger ionic radius than the element it is replacing will provide strain on the lattice structure and benefit spontaneous segregation of the dopant to an interface, a region that can more easily accommodate the dopant in terms of strain.

The impact of dopant segregation can be described by the Gibbs adsorption isotherm shown in **Equation 2**, where γ_{gb} is the grain boundary energy, Γ_B is the excess of the dopant at

$$d\gamma_{gb} = -\Gamma_B d\mu_B \tag{2}$$

the grain boundary, and μ_B is the chemical potential of the dopant. The Γ_B term describes the amount of excess dopant at the interface relative to the fraction in the bulk material. **Figure 1.2** below also shows how the grain boundary energy changes as a function of the chemical potential.[14] The initial grain boundary energy, γ_o, remains unchanged until the segregation enthalpy, H_{seg}, is reached. In this phase of the plot the dopant will remain in solid solution because of the low concentration of dopant and the ability of the bulk structure to accommodate

the dopant. In the second stage, the dopant reaches the enthalpy of segregation and the interfacial energy begins to decrease linearly as a function of the surface excess of the dopant. If too much dopant is added to the system, the interfacial energy will plateau and cause a dopant-rich secondary phase to precipitate from the interface, becoming saturated. The middle region is the ideal space for operation where the excess dopant is maximized for interfacial energy reduction without precipitating a secondary phase during synthesis or processing.

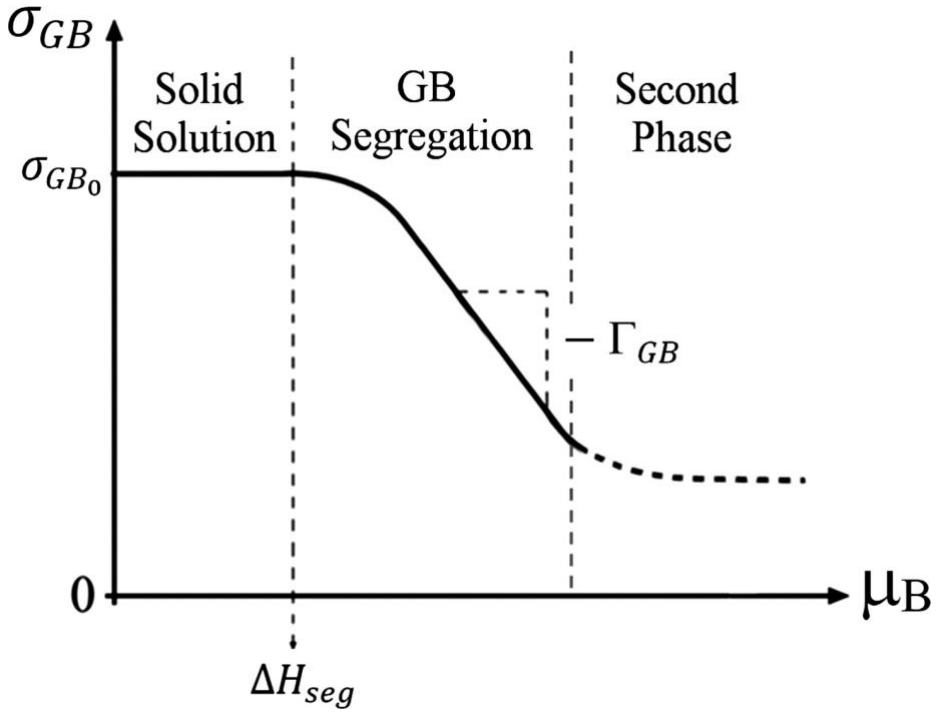

Figure 1.2. Grain boundary energy dependence on the chemical potential of the dopant according to the Gibbs adsorption isotherm.[14]

Despite the extensive reports in the literature confirming that dopant segregation helps stabilize ceramic interfaces, the experimental selection of dopants is still a long and arduous process of synthesis variations. Therefore, a model to describe the complexity of dopant segregation is a valuable methodology to reduce the number of experiments run and screen several dopants in a short time. Weissmüller's work demonstrated the effect of dopant

segregation on the grain boundary energy depended on several thermodynamic parameters, including the enthalpy change in the bulk, excess of enthalpy change at the grain boundaries, amount of solute atoms in the bulk, and the excess dopant at the grain boundaries.[15] An analytical method like Weissmüller's can be useful for understanding the fundamental driving forces and critical thermodynamic properties dictating the dopant segregation. However, collecting all these values for different systems requires careful experimental protocols or trustworthy calculated values in the literature, which are difficult to attain for doped systems studying unique new chemistries. Additionally, studying the segregation behavior of dopants to specific grain boundaries and surfaces can be valuable information in dopant selection that analytical models cannot currently provide.

Recently, Hasan et al. studied the segregation potentials of dopants in $MgAl_2O_4$ structures to study how ionic size impacted the segregation of the dopants.[16] The atomistic calculations show the segregation energy increases with ionic size for isovalent dopants and that the oxidation state can play a role in dopant segregation. The dopant segregation also caused a surface energy decrease in all six of the surface constructions studied relative to the undoped surface energies. Motivated by those findings, the present work utilizes molecular static calculations in the LAMMPS framework to calculate segregation potentials for two surface structures and two grain boundary structures in $LiCoO_2$ (LCO). Additionally, this work expanded to study ten dopants that ranged in ionic radius and explored divalent, trivalent, and quadrivalent oxidation states. This expansive dopant selection process allows dopants of various oxidation states and ionic sizes to be studied and provides a more thorough understanding of segregation behavior. The addition of surface and grain boundary structures also expands the knowledge of how dopants may preferentially segregate to interfaces of different types.

Interfacial Energy Measurements

Interfacial energies are critical for nanoparticle stability and control of the sintering and grain growth mechanisms for maintaining the nanoscale nature of the particles during synthesis and processing. Several models have been developed to describe sintering and densification processes, and the model developed by Lange et al. relates the sintering process to the interfacial energies.[17,18] The relationship between the grain boundary energy, γ_{GB}, and surface energy, γ_S, is shown in **Equation 3** relative to the dihedral angle, φ_e.

$$\frac{\gamma_{GB}}{\gamma_S} = 2\cos\left(\frac{\varphi_e}{2}\right) \quad (3)$$

The dihedral angle is defined as the angle between two particles, as shown in the inset in **Figure 1.3**. **Figure 1.3** also demonstrates the relationship between the energy of the system and the dihedral angle.[19] When the dihedral angle reaches the lowest energy point, the angle is now referred to as the equilibrium angle. Although it is termed 'equilibrium', these are truthfully metastable states as particle rotation and grain growth can kinetically alter the angles and reinitiate sintering mechanisms.[20] However, the figure clearly shows the dependence of the dihedral angle minima on the ratio of grain boundary energy to surface energy. As the ratio of the interfacial energies decrease, the equilibrium angle increases and drives the system to a lower energy state. This thermodynamic data can help inform if a system of nanoparticles will likely continue to sinter or has globally reached an equilibrium and now has low driving forces for coarsening.

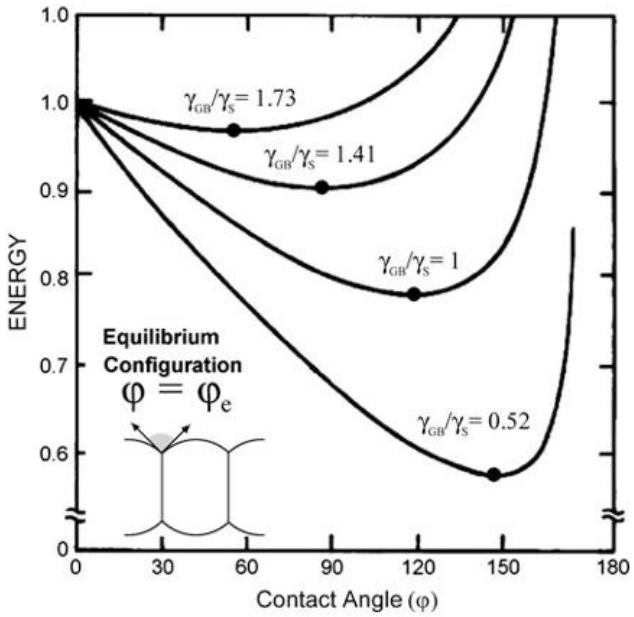

Figure 1.3. Energy change related to the contact angle between particles for different ratios of interfacial energies.[19]

The role that dopants can play in the grain growth process is also essential to understand, and there have been several models attempting to explain this phenomenon. An equation explaining the velocity, v, at the grain boundary during a normal grain growth process is shown in **Equation 4**, where M_{GB} is the grain boundary mobility, and r is the grain size.[20]

$$v = M_{GB} \frac{\gamma_{GB}}{r} \tag{4}$$

$$f = \frac{r M_{GB} \gamma_{GB}}{r_{max}^2} \tag{5}$$

The effect of dopants on the mobility of that interface can be seen in **Equation 5** developed by Michels et al., where f is the drag force and r_{max} is a max grain size introduced to account for the addition of the dopant or impurity.[21] The drag force acts in the opposite direction of the velocity term in **Equation 4**, so the drag force can be subtracted from the velocity to calculate the new mobility of the grain boundary. The excess dopant at the interface provides a

drag force since the dopant sits directly at the interface, and typically, the dopants have a larger ionic radius and can change the energy landscape at the grain boundary. Other imperfections in lattice structure have also been found to impact the grain boundary mobility like impurities, vacancies, and dislocations.[22] Nagpure et al. studied coarsening effects in $LiFePO_4$ nanoparticles cycled in a lithium-ion battery.[23] The TEM images of the cycled nanoparticles are shown in **Figure 1.4** for the unaged and aged nanoparticles. The unaged nanoparticles show more porosity, and individual nanoparticles are separated throughout the image. The aged nanoparticles were cycled until capacity dropped by 20% and showed more agglomerated particles and less porosity. This cycle-induced coarsening can cause nanoparticles to undergo grain growth and fundamentally change the morphology and nanostructure of the material. Additionally, intergranular cracking can be a major issue in small-scale cathode materials,[24] but La doping has shown to reduce the amount of intergranular cracking and improve the high rate capabilities of micron-size cathode materials.[25,26]

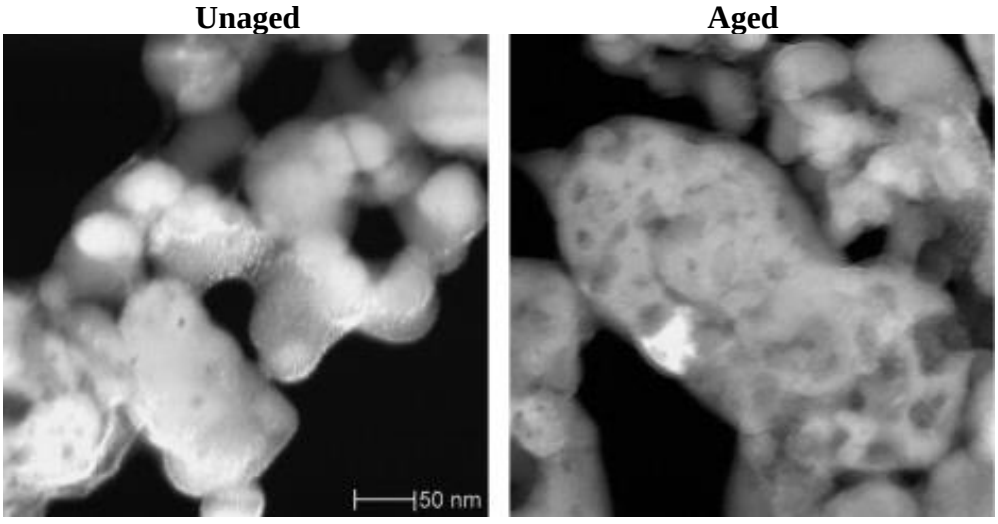

Figure 1.4. TEM images of unaged and aged $LiFePO_4$ nanoparticles after cycling. The aged nanoparticles were cycled in a cell until capacity was reduced by 20%.[23]

The Gibbs adsorption equation shown previously demonstrated the dopants can reduce the grain boundary energy as a function of the excess at the interface.[14,27] This indicates by **Equation 4** the reduced grain boundary energy will decrease the grain boundary's driving force for grain growth and the grain boundary's velocity, making particles kinetically slower to grow. In addition, the drag force provided by dopants at the interface limits the mobility of grain boundaries, and the reduction in surface energy provides less driving force for coarsening mechanisms like Ostwald ripening.[28] Nakajima et al. studied Sc-doped $LiMn_2O_4$ and showed that Sc reduced the surface energy through dopant segregation to interfaces.[29] They also showed this reduction in surface energy and the segregation to grain boundaries produced smaller crystallite sizes and higher specific surface areas in the doped nanoparticles due to the stabilization effect. Leong et al. performed further electrochemical studies on these particles and confirmed higher capacity retention and lower charge transfer resistance in doped nanoparticles.[30] Doping has shown to improve interfacial stability and maintain the nanostructure, but there are still very few thermodynamic studies of doped cathode materials. Therefore, in this study doped LCO nanoparticles were synthesized to study the effect of dopant segregation.

Building upon the work of Maram et al. and Okubo et al.,[31,32] a method was developed in this study to synthesize homogeneous and stoichiometric $LiCoO_2$ nanoparticles. The process uses coprecipitation to obtain $Co(OH)_2$ nanoparticles, which are then oxidized into CoOOH by bubbling air through the suspension to obtain cobalt in the trivalent charge state. Then the nanoparticles are hydrothermally synthesized in a LiOH solution at 180°C to form the final $LiCoO_2$ phase. This synthesis method can easily be expanded to doped samples of lithium cobalt oxide by replacing a small amount of the cobalt precursor in the coprecipitation with the dopant precursor.

The interfacial energies will be determined using differential scanning calorimetry (DSC) to measure the heat of grain growth and sintering in nanocrystalline material to determine the interfacial energies. The method measures the heat flow while sintering the sample between two states and utilizes properties like specific surface area and solid-solid interfacial areas at the initial state and final state to determine the heat of sintering.[33,34] **Equation 6** shows the relation,

$$\Delta H_{sintering} = \gamma_s \Delta A_s + \gamma_{GB} \Delta A_{GB} \quad (6)$$

where $\Delta H_{sintering}$ is the heat of sintering, the subscript *s* is the solid-vapor interfaces or surface, and the subscript *GB* is the solid-solid interfaces or grain boundaries. The heat of sintering can be measured for different samples by changing the initial or final grain size/surface area, and then a system of equations can be solved to give the interfacial energies. The experimental operating space will be modified to account for other contributions to the heat flow, like phase transformation, gas desorption, and reduction/oxidation reactions. These adjustments on the temperature ramp and gas environment are made to ensure all contributions to the heat flow are from sintering and grain growth mechanisms. This methodology gives a direct comparison for doped and undoped nanoparticles while monitoring the microstructure evolution throughout the sintering process.

Delithiated Thermodynamic Studies

Delithiated structures of $LiCoO_2$ are known to have chemical and structural instabilities as lithium is removed, making it a poor candidate for the DSC method above because the instabilities grow as the temperature is increased.[3,35] For this reason, a water adsorption technique will be used to measure the surface energy of the material as lithium is removed from the structure. Lithium can be removed chemically to emulate electrochemical delithiation through a nitric acid washing process. This process is easier for recovery of the delithiated

materials and has been shown to be a useful method for studying thermodynamic properties of materials.[36–38]

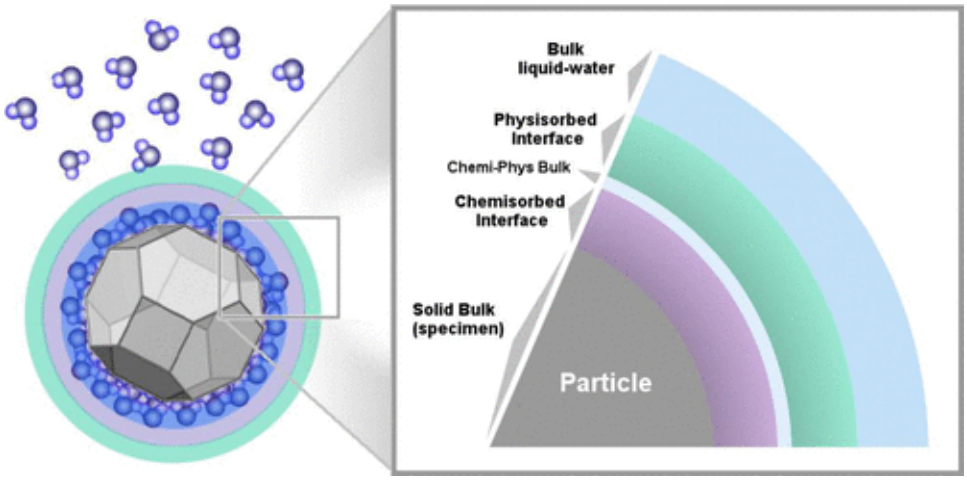

Figure 1.5. Schematic showing the water adsorption layers as water is dosed onto an anhydrous surface and transitions towards a fully saturated interface.[39]

The water adsorption technique measures the heat of adsorption of water molecules as they are dosed onto an anhydrous surface and builds on the theory of water wetting high energy surfaces.[39,40] The water adsorption follows a two interface model of the Gibbs Adsorption Isotherm shown in **Equation 7**, where SA is the Brunauer–Emmett–Teller (BET) measured surface area, γ is the surface energy, I_1 is the chemisorbed interface, I_2 is the physisorbed

$$SAd\gamma = -\sum_{I_1,I_2}(\sum_i \theta_i d\mu_i) \quad (7)$$

interface, θ is the surface coverage, and μ is the chemical potential. A physical representation of this is shown in **Figure 1.5**, with the anhydrous particle building up water layers on the surface.[39] The chemisorption phase causes water to dissociate onto the surface and transitions to a physisorbed layer at higher water coverages that still interacts with the surface before finally reaching a fully saturated surface that is equivalent to a liquid water surface.[41] As water is slowly dosed onto the anhydrous surface of the nanoparticle, the initial heats of adsorption are strongly

exothermic as the water chemisorbs to the surface and becomes less exothermic in the physisorbed interface. The experiment reaches completion when the surface energy is equivalent to the surface tension of water and is indicated by the heat of adsorption plateauing at -44 kJ/mol, which is the heat of adsorption of a molecule of water onto a droplet of water. The experiment develops an adsorption isotherm and individual heats of adsorption for each dosing event that can be used to calculate the average surface energy of particles. The calorimetry measurements capture the heat as the experiment proceeds through the layers, which provides a more robust calculation method compared to other surface energy measurements that require you to know the exact transition points between layers. This is particularly useful as water adsorption is a complex and dynamic process that can transition from icelike adsorbed surface species towards bulk liquid water, and can frequently reconstruct as more water is adsorbed.[41–43]

This method will give experimentally determined quantitative values for the surface energy of delithiated $LiCoO_2$ for the first time and can be compared to computational efforts to quantify surface energies.[44,45] As previously pointed out, the stability of delithiated structures while electrochemically cycling is a persistent issue in cathode materials. The understanding of interfacial stability can inform the design of more stable nanomaterials. If the surface energies are drastically changing from delithiation, perhaps dopant segregation can lower the surface energies of the undoped materials and help normalize the energy landscape on the surface of the particles. Additionally, this method will corroborate the results of the sintering studies and confirm the surface reactivity of doped nanoparticles. The thermodynamic understanding of nanoscale materials is a crucial step in the process of expanding their utility and application.

References

(1) Hausbrand, R.; Cherkashinin, G.; Ehrenberg, H.; Gröting, M.; Albe, K.; Hess, C.;

Jaegermann, W. Fundamental Degradation Mechanisms of Layered Oxide Li-Ion Battery Cathode Materials: Methodology, Insights and Novel Approaches. *Mater. Sci. Eng. B Solid-State Mater. Adv. Technol.* **2015**, *192* (C), 3–25. https://doi.org/10.1016/J.MSEB.2014.11.014.

(2) Pender, J. P.; Jha, G.; Hyun Youn, D.; Ziegler, J. M.; Andoni, I.; Choi, E. J.; Heller, A.; Dunn, B. S.; Weiss, P. S.; Penner, R. M.; Buddie Mullins, C. Electrode Degradation in Lithium-Ion Batteries. *ACS Nano* **2020**, *14*, 59. https://doi.org/10.1021/acsnano.9b04365.

(3) Liu, C.; Neale, Z. G.; Cao, G. Understanding Electrochemical Potentials of Cathode Materials in Rechargeable Batteries. *Mater. Today* **2016**, *19* (2), 109–123. https://doi.org/10.1016/J.MATTOD.2015.10.009.

(4) Xia, H.; Meng, S. Y.; Lu, L.; Ceder, G. Electrochemical Behavior and Li Diffusion Study of $LiCoO_2$ Thin Film Electrodes Prepared by PLD. **2007**.

(5) Bruce, P. G.; Scrosati, B.; Tarascon, J. M. Nanomaterials for Rechargeable Lithium Batteries. *Angew. Chemie - Int. Ed.* **2008**, *47* (16), 2930–2946. https://doi.org/10.1002/ANIE.200702505.

(6) Sotelo Martin, L. E.; Castro, R. H. R. Al Excess Extends Hall-Petch Relation in Nanocrystalline Zinc Aluminate. *J. Am. Ceram. Soc.* **2022**, *105* (2), 1417–1427. https://doi.org/10.1111/JACE.18176.

(7) Bokov, A.; Zhang, S.; Feng, L.; Dillon, S. J.; Faller, R.; Castro, R. H. R. Energetic Design of Grain Boundary Networks for Toughening of Nanocrystalline Oxides. *J. Eur. Ceram. Soc.* **2018**, *38* (12), 4260–4267. https://doi.org/10.1016/j.jeurceramsoc.2018.05.007.

(8) McHale, J. M.; Auroux, A.; Perrotta, A. J.; Navrotsky, A. Surface Energies and Thermodynamic Phase Stability in Nanocrystalline Aluminas. *Science (80-.).* **1997**, *277*

(5327), 788–789. https://doi.org/10.1126/SCIENCE.277.5327.788/ASSET/3A6BDCD6-FC2E-4F3B-AC87-01630DAC7C8B/ASSETS/GRAPHIC/SE3275545004.JPEG.

(9) Castro, R. H. R.; T^ Orres, R. B.; Pereira, G. J.; Gouv^, D. Interface Energy Measurement of MgO and ZnO: Understanding the Thermodynamic Stability of Nanoparticles. *Chem. Mater* **2010**, *22*, 2502–2509. https://doi.org/10.1021/cm903404u.

(10) Dholabhai, P. P.; Aguiar, J. A.; Wu, L.; Holesinger, T. G.; Aoki, T.; Castro, R. H. R.; Uberuaga, B. P. Structure and Segregation of Dopant-Defect Complexes at Grain Boundaries in Nanocrystalline Doped Ceria. *Phys. Chem. Chem. Phys* **2015**, *17*, 15375. https://doi.org/10.1039/c5cp02200b.

(11) Murdoch, H. A.; Schuh, C. A. Estimation of Grain Boundary Segregation Enthalpy and Its Role in Stable Nanocrystalline Alloy Design. https://doi.org/10.1557/jmr.2013.211.

(12) Wu, L.; Dey, S.; Gong, M.; Liu, F.; Castro, R. H. R. Surface Segregation on Manganese Doped Ceria Nanoparticles and Relationship with Nanostability. *J. Phys. Chem. C* **2014**, *118* (51), 30187–30196. https://doi.org/10.1021/JP508663P/ASSET/IMAGES/LARGE/JP-2014-08663P_0008.JPEG.

(13) Hwang, S. -L; Chen, I. -W. Grain Size Control of Tetragonal Zirconia Polycrystals Using the Space Charge Concept. *J. Am. Ceram. Soc.* **1990**, *73* (11), 3269–3277. https://doi.org/10.1111/J.1151-2916.1990.TB06449.X.

(14) Kirchheim, R. Reducing Grain Boundary, Dislocation Line and Vacancy Formation Energies by Solute Segregation. I. Theoretical Background. *Acta Mater.* **2007**, *55* (15), 5129–5138. https://doi.org/10.1016/J.ACTAMAT.2007.05.047.

(15) Weissmüller, J. Alloy Effects in Nanostructures. *Nanostructured Mater.* **1993**, *3* (1–6),

261–272. https://doi.org/10.1016/0965-9773(93)90088-S.

(16) Hasan, M. M.; Dholabhai, P. P.; Castro, R. H. R.; Uberuaga, B. P. Stabilization of MgAl2O4 Spinel Surfaces via Doping. *Surf. Sci.* **2016**, *649*, 138–145. https://doi.org/10.1016/J.SUSC.2016.01.028.

(17) Kellett, B. J.; Lange, F. F. Thermodynamics of Densification: I, Sintering of Simple Particle Arrays, Equilibrium Configurations, Pore Stability, and Shrinkage. *J. Am. Ceram. Soc.* **1989**, *72* (5), 725–734. https://doi.org/10.1111/J.1151-2916.1989.TB06208.X.

(18) Lange, F. F.; Kellett, B. J. Thermodynamics of Densification: II, Grain Growth in Porous Compacts and Relation to Densification. *J. Am. Ceram. Soc.* **1989**, *72* (5), 735–741. https://doi.org/10.1111/J.1151-2916.1989.TB06209.X.

(19) Lange, F. F. Densification of Powder Compacts: An Unfinished Story. *J. Eur. Ceram. Soc.* **2008**, *28* (7), 1509–1516. https://doi.org/10.1016/J.JEURCERAMSOC.2007.12.016.

(20) Castro, R.; Benthem, K. Van. *Sintering: Mechanisms of Convention Nanodensification and Field Assisted Processes*; 2012.

(21) Michels, A.; Krill, C. E.; Ehrhardt, H.; Birringer, R.; Wu, D. T. Modelling the Influence of Grain-Size-Dependent Solute Drag on the Kinetics of Grain Growth in Nanocrystalline Materials. *Acta Mater.* **1999**, *47* (7), 2143–2152. https://doi.org/10.1016/S1359-6454(99)00079-8.

(22) Gottstein, G.; Shvindlerman, L. S. Grain Boundary Migration in Metals : Thermodynamics, Kinetics, Applications, Second Edition. *Grain Bound. Migr. Met.* **2009**. https://doi.org/10.1201/9781420054361.

(23) Nagpure, S. C.; Babu, S. S.; Bhushan, B.; Kumar, A.; Mishra, R.; Windl, W.; Kovarik, L.; Mills, M. Local Electronic Structure of LiFePO4 Nanoparticles in Aged Li-Ion Batteries.

Acta Mater. **2011**, *59* (18), 6917–6926. https://doi.org/10.1016/J.ACTAMAT.2011.07.043.

(24) Liu, H.; Wolfman, M.; Karki, K.; Yu, Y.-S.; Stach, E. A.; Cabana, J.; Chapman, K. W.; Chupas, P. J. Intergranular Cracking as a Major Cause of Long-Term Capacity Fading of Layered Cathodes. *Nano Lett.* **2017**, *17*, 3452–3457. https://doi.org/10.1021/acs.nanolett.7b00379.

(25) Liu, Q.; Su, X.; Lei, D.; Qin, Y.; Wen, J.; Guo, F.; Wu, Y. A.; Rong, Y.; Kou, R.; Xiao, X.; Aguesse, F.; Bareño, J.; Ren, Y.; Lu, W.; Li, Y. Approaching the Capacity Limit of Lithium Cobalt Oxide in Lithium Ion Batteries via Lanthanum and Aluminium Doping. *Nat. Energy 2018 311* **2018**, *3* (11), 936–943. https://doi.org/10.1038/s41560-018-0180-6.

(26) Ghosh, P.; Mahanty, S.; Basu, R. N. Lanthanum-Doped LiCoO2 Cathode with High Rate Capability. *Electrochim. Acta* **2009**, *54* (5), 1654–1661. https://doi.org/10.1016/J.ELECTACTA.2008.09.050.

(27) Bangham, D. H. THE GIBBS ADSORPTION EQUATION AND ADSORPTION ON SOLIDS. *Trans. Faraday Soc.* **1937**, *33*, 805–811.

(28) Fischmeister, H.; Grimvall, G. Ostwald Ripening — A Survey. *Sinter. Relat. Phenom.* **1973**, 119–149. https://doi.org/10.1007/978-1-4615-8999-0_9.

(29) Nakajima, K.; Souza, F. L.; Freitas, A. L. M.; Thron, A.; Castro, R. H. R. Improving Thermodynamic Stability of Nano-LiMn2O4for Li-Ion Battery Cathode. *Chem. Mater.* **2021**, *33* (11), 3915–3925. https://doi.org/10.1021/ACS.CHEMMATER.0C04305/SUPPL_FILE/CM0C04305_SI_001.PDF.

(30) Leong, V. G. H.; Hong, S. S.; Castro, R. H. R. Improved Electrochemical Performance in

Sc-Doped Nanocrystalline LiMn2O4. *Mater. Lett.* **2022**, *325*, 132824. https://doi.org/10.1016/J.MATLET.2022.132824.

(31) Maram, P. S.; Costa, G. C. C.; Navrotsky, A. Experimental Confirmation of Low Surface Energy in LiCoO 2 and Implications for Lithium Battery Electrodes . *Angew. Chemie* **2013**, *125* (46), 12361–12364. https://doi.org/10.1002/ANGE.201305375.

(32) Okubo, M.; Hosono, E.; Kim, J.; Enomoto, M.; Kojima, N.; Kudo, T.; Zhou, H.; Honma, I. Nanosize Effect on High-Rate Li-Ion Intercalation in LiCoO2 Electrode. *J. Am. Chem. Soc.* **2007**, *129* (23), 7444–7452. https://doi.org/10.1021/ja0681927.

(33) Castro, R. H. R.; Gouvêa, D. Sintering and Nanostability: The Thermodynamic Perspective. *J. Am. Ceram. Soc.* **2016**, *99* (4), 1105–1121. https://doi.org/10.1111/JACE.14176.

(34) Muche, D. N. F.; Marple, M. A. T.; Sen, S.; Castro, R. H. R. Grain Boundary Energy, Disordering Energy and Grain Growth Kinetics in Nanocrystalline MgAl2O4 Spinel. *Acta Mater.* **2018**, *149*, 302–311. https://doi.org/10.1016/J.ACTAMAT.2018.02.052.

(35) Reimers, J. N.; Dahn, J. R. Electrochemical and In Situ X-Ray Diffraction Studies of Lithium Intercalation in Li x CoO2. *J. Electrochem. Soc.* **1992**, *139* (8), 2091–2097. https://doi.org/10.1149/1.2221184/XML.

(36) Takahashi, Y.; Kijima, N.; Dokko, K.; Nishizawa, M.; Uchida, I.; Akimoto, J. Structure and Electron Density Analysis of Electrochemically and Chemically Delithiated LiCoO2 Single Crystals. *J. Solid State Chem.* **2007**, *180* (1), 313–321. https://doi.org/10.1016/J.JSSC.2006.10.018.

(37) Furushima, Y.; Yanagisawa, C.; Nakagawa, T.; Aoki, Y.; Muraki, N. Thermal Stability and Kinetics of Delithiated LiCoO2. *J. Power Sources* **2011**, *196* (4), 2260–2263.

https://doi.org/10.1016/J.JPOWSOUR.2010.09.076.

(38) Gupta, R.; Manthiram, A. Chemical Extraction of Lithium from Layered LiCoO2. *J. Solid State Chem.* **1996**, *121* (2), 483–491. https://doi.org/10.1006/JSSC.1996.0067.

(39) Drazin, J. W.; Castro, R. H. R. Water Adsorption Microcalorimetry Model: Deciphering Surface Energies and Water Chemical Potentials of Nanocrystalline Oxides. **2014**. https://doi.org/10.1021/jp5016356.

(40) Castro, R. H. R.; Quach, D. V; Rock, P. A. Analysis of Anhydrous and Hydrated Surface Energies of Gamma-Al 2 O 3 by Water Adsorption Microcalorimetry. **2012**. https://doi.org/10.1021/jp309319j.

(41) Asay, D. B.; Kim, S. H. Evolution of the Adsorbed Water Layer Structure on Silicon Oxide at Room Temperature. **2005**. https://doi.org/10.1021/jp053042o.

(42) Pérez-Hernández, G.; Schmidt, B. Anisotropy of the Water–Carbon Interaction: Molecular Simulations of Water in Low-Diameter Carbon Nanotubes. *Phys. Chem. Chem. Phys.* **2013**, *15* (14), 4995–5006. https://doi.org/10.1039/C3CP44278K.

(43) Yamada, T.; Tamamori, S.; Okuyama, H.; Aruga, T. Anisotropic Water Chain Growth on Cu(110) Observed with Scanning Tunneling Microscopy. **2006**. https://doi.org/10.1103/PhysRevLett.96.036105.

(44) Kramer, D.; Ceder, G. Tailoring the Morphology of LiCoO2: A First Principles Study. *Chem. Mater.* **2009**, *21* (16), 3799–3809. https://doi.org/10.1021/cm9008943.

(45) Qian, D.; Hinuma, Y.; Chen, H.; Du, L. S.; Carroll, K. J.; Ceder, G.; Grey, C. P.; Meng, Y. S. Electronic Spin Transition in Nanosize Stoichiometric Lithium Cobalt Oxide. *J. Am. Chem. Soc.* **2012**, *134* (14), 6096–6099. https://doi.org/10.1021/ja300868e.

Chapter 2: Atomistic Simulation Informs Interface Engineering of Nanoscale $LiCoO_2$

This work has been published in the American Chemical Society Chemistry of Materials Journal (2022). (https://doi.org/10.1021/acs.chemmater.2c01246)

Abstract

Lithium-ion batteries continue to be a critical part of the search for enhanced energy storage solutions. Understanding the stability of interfaces (surfaces and grain boundaries) is one of the most crucial aspects of cathode design to improve the capacity and cyclability of batteries. Interfacial engineering through chemical modification offers the opportunity to create metastable states in the cathodes to inhibit common degradation mechanisms. Here, we demonstrate how atomistic simulations can effectively evaluate dopant interfacial segregation trends and be an effective predictive tool for cathode design despite the intrinsic approximations. We computationally studied two surfaces, {001} and {104}, and grain boundaries, Σ3 and Σ5, of $LiCoO_2$ to investigate the segregation potential and stabilization effect of dopants. Isovalent and aliovalent dopants (Mg^{2+}, Ca^{2+}, Sr^{2+}, Sc^{3+}, Y^{3+}, Gd^{3+}, La^{3+}, Ti^{4+}, Sn^{4+}, Zr^{4+}) were studied by replacing the Co^{3+} sites in all four of the constructed interfaces. The segregation energies of the dopants increased with the ionic radius of the dopant. They exhibited a linear dependence on the ionic size for divalent, trivalent, and quadrivalent dopants for surfaces and grain boundaries. The magnitude of the segregation potential also depended on the surface chemistry and grain boundary structure, showing higher segregation energies for the Σ5 grain boundary compared with the lower energy Σ3 boundary and higher for the {104} surface compared to the {001}. Lanthanum doped nanoparticles were synthesized and imaged with STEM-EELS to validate the

computational results, revealing the predicted lanthanum enrichment at grain boundaries and both the {001} and the {104} surfaces.

Introduction

Lithium-ion batteries continue to be an integral part of the rechargeable battery industry and the search for sustainable energy storage. Although lithium-ion technologies have been widely utilized over the past few decades, energy content and charging rates are still insufficient to meet automotive energy demands.[1] Nanomaterials offer potential improvements to enhanced battery operation kinetics through the increased surface area, shortening of diffusion path lengths, and increased rates of lithium intercalation.[2] However, the main degradation mechanisms, transition metal dissolution, reactivity to the electrolyte, and intergranular cracking, are exacerbated at the nanoscale, leading to catastrophic decreases in capacity after a few cycles.[3] Many of the problems in nanoscale cathodes directly result from their thermodynamic instabilities. A significant fraction of atoms are located at interfacial regions in nanomaterials, bringing intrinsic excess energies to the system.[4,5] A potential method for stabilizing surfaces and grain boundaries is the compositional design to provoke dopant segregation, also known as interfacial excess. Following derivations from the Gibbs adsorption isotherm,[6] interfacial excesses of solid solutes can reduce stress energies and increase the overall stability of nanomaterials.[7] Nakajima et al. recently explored scandium doping of $LiMn_2O_4$ nanoparticles and directly measured the doping effects on surface and grain boundary energies.[8] The data showed decreasing interfacial energies with the scandium doping and preferential scandium segregation to the grain boundaries. The results align with other studies using this 'interfacial engineering' to stabilize catalytic supports and other nanostructured oxides.[9,10] In parallel, Wang et al. showed that dopant segregation enhances cathodes' cyclability through suppressed

intragranular cracking and increased mechanical strength.[11] Although the authors did not discuss interfacial energies; interfacial segregation always has a cause-effect relationship with the local energies. The work exploits the relationship between interfacial mechanical strength and thermodynamics, as recently reported.[12,13] It is important to note that interfacial excess differs from coating technologies.[14] The first is a spontaneous phenomenon driven by thermodynamics that does not require additional processing steps and does not constitute a separate phase.

There is still an overall lack of thermodynamic data on dopant segregation correlations with interfacial energies in relevant technological systems, such as lithium-ion structures, to enable effective design for performance.[15–17] In this work, we used atomistic simulations to study relevant interfaces in nanoscale $LiCoO_2$ (LCO) to investigate the segregation potentials of dopants to surfaces and grain boundaries. The goal is to inform experiments regarding dopant selection criteria for interfacial energy design. Two representative surfaces, {001} and {104}, and two low index grain boundaries, Σ3 and Σ5, were constructed using atomistic models and energetically minimized. Different dopants substituted individual cobalt sites in the structure to map the simulation cell energy at different dopant positions. Divalent, trivalent, and tetravalent dopants with different ionic radii were introduced into the systems to explore the physical-chemical impacts on the relative segregation energy. Overall, dopants showed higher segregation energy at {104} surfaces than at {001}, and higher segregation energies for Σ5 as compared to Σ3. Moreover, the segregation energies increased with the atomic radius. Informed by the simulation results, LCO nanoparticles were synthesized and doped with the element with the highest segregation energy, lanthanum. The results suggest simulations can satisfactorily predict segregation in cathode materials despite the assumptions made, but more quantitative segregation experiments are needed to establish more reliable models for engineering applications.

Methods

Atomic Simulations

The atomistic simulations were performed within the LAMMPS framework,[18] and all simulations were conducted with three-dimensional periodic boundary conditions in all directions. We applied standard Coulomb-Buckingham potentials to model the two-body atomic interactions.[19] The Buckingham potential models the energy for the short-range interactions between particles. The additional Coulombic potential term models the electrostatic potential energy of the long-range interaction between ionic charges summed using Ewald's method.[20] The cutoff distance for all two-body interactions in the simulations was 8.0 Angstroms and the Buckingham potential parameters for all species considered are shown in **Table 2.1**. We note that, while there are other potentials for the Li-Co-O system, including some that describe charge transfer,[21,22] this parameter set is the only parameterization we found for which LCO was stable and that had transferable parameter sets consistent with the same O^{2-}-O^{2-} interaction for the dopant species.

Table 2.1. Interatomic pair potential parameters for LCO and dopant-oxygen interactions in the Buckingham Coulomb potential.

Ionic Pair	A (eV)	ρ (Å)	C (eV*Å^6)
$O^{2-} \cdots O^{2-}$ [23]	22764.3	0.149	43.0
$Li^{+} \cdots O^{2-}$ [23]	15785	0.1964	0
$Co^{3+} \cdots O^{2-}$ [23]	1195	0.3087	0
$La^{3+} \cdots O^{2-}$ [24]	1545.21	0.3590	0
$Gd^{3+} \cdots O^{2-}$ [25]	1885.75	0.3399	20.34
$Y^{3+} \cdots O^{2-}$ [26]	1310.00	0.3561	0
$Sc^{3+} \cdots O^{2-}$ [27]	1337.63	0.34303	0
$Ti^{4+} \cdots O^{2-}$ [28]	754.2	0.3879	0
$Sn^{4+} \cdots O^{2-}$ [29]	938.7	0.3813	0
$Zr^{4+} \cdots O^{2-}$ [30]	1057.03	0.376	0
$Mg^{2+} \cdots O^{2-}$ [31]	821.60	0.3242	0
$Ca^{2+} \cdots O^{2-}$ [31]	1228.90	0.3372	0
$Sr^{2+} \cdots O^{2-}$ [31]	1400.0	0.3500	0

The layered O3 trigonal $LiCoO_2$ (Space Group R-3m) unit cell was obtained from The Materials Project (ID: mp-22526).[32] Two low-index surfaces and grain boundaries were constructed to study the segregation profile of ten different dopants. The two design constraints used for building the interfaces were (a) maintaining the stoichiometry of the structure by not deleting or adding any atoms and (b) modifying polar surfaces to remove any surface dipoles. One polar surface, {001}, and one nonpolar surface, {104}, were studied due to their stability,

prevalence in the LCO structure, and expected low surface energies.[33] For the polar {001} surface, several terminations could be considered based on the cleavage plane chosen. According to Hu et al., the cobalt layer termination is an unstable configuration that causes a mix of trivalent and tetravalent cobalt ions on the surface layer, leading to numerous surface configurations of cobalt ions with different oxidation states.[34] The two possible oxygen terminations also have low stability and require a strongly reducing environment to stabilize the surface oxygen. Due to the instability of the cobalt and oxygen terminations, the lithium termination is the preferred orientation for the {001} surface.[35] One crucial consideration of the slab geometry for Tasker Type III surfaces, such as the {001} surface studied here, is to prevent surface dipole moments that cause the surface energy to diverge.[36] The surface dipole is counteracted by moving half of a monolayer of lithium from the top surface to the bottom surface; the resulting surface is illustrated in **Figure 2.1a**. As described by Kramer and Ceder,[35] that structure has an equal charge of +1/2 at both surface layers and a net charge of -1 in the bulk. This leads to a global charge balance of the stoichiometric slab while ensuring Co remains in the trivalent oxidation state. It also provides that the two resulting surfaces have a very similar, if not identical, atomic structure. The vacancy configuration of the surface was modeled after the work of Ceder and Van Der Ven and moved every other lithium row to the opposite surface of the structure.[37] This configuration of the surface lithium atoms is the lowest surface energy arrangement that Ceder and Van Der Ven constructed. The designed slab had dimensions of 1.7 x 1.5 x 5.5 nm^3 with 0.85 nm of skew in the xy plane and 2 nm of vacuum introduced for both the top and bottom surface.

For the nonpolar Tasker Type I {104} surface,[36] there is only one possible termination of O-Li-O-Co and no surface dipole to cause surface energy divergence. The structure dimensions

for this surface were 1.7 x 1.7 x 4.6 nm^3 with 2 nm of vacuum introduced at both surfaces, as shown in **Figure 2.1b**. The same LCO (Space Group R-3m) structure from Materials Project was used to create the slab-surface model of the {104} surface.

Two low index grain boundaries were also studied to understand dopant segregation profiles and interface stabilization at grain boundaries. An atomic model of a Σ3 grain boundary of LCO was constructed by using GB-code[38] and VESTA[39] with a common rotation axis of {110} and an orientation plane of $\{1\bar{1}2\}$ (**Figure 2.1c**). We considered the conventional cell of LCO first to construct the Σ3 GB using GB-code without specifying the chemical identity of the atoms. Next, we used VESTA to assign the chemical identities. That boundary represents the simplest and lowest energy GB structure in most materials and has dimensions of 0.8 x 1.0 x 10.3 nm^3.

The Σ5 grain boundary, representing a higher energy interface but still structurally simple, was designed using the Aimsgb Python framework for building periodic grain boundaries.[40] The tilt boundary was constructed with a common rotation axis between the two grains along the {001} plane and by orienting the grain boundary plane along the {120} plane. An additional interfacial distance of 1.0 Angstrom was added between the two grains to prevent overlapping atoms and allow the minimizations to converge. The structure dimensions were 0.8 x 8.8 x 1.4 nm^3 with an xy skew of 3.2 nm, as shown in **Figure 2.1d**.

All four designed structures were energetically minimized by anisotropically relaxing the atoms and simulation cells before any dopant replacements. The grains were translated in both directions parallel to the grain boundary in 0.1 Angstrom increments and energetically minimized at each position for the two grain boundaries. The gamma surface mapping provides

an energy landscape of the grain boundary with respect to the relative translation of the grains. The lowest energy structure was used for the dopant studies.

The dopants selected for this study covered a range of ionic radii and oxidation states: isovalent dopants were chosen (Sc^{3+}, Y^{3+}, Gd^{3+}, La^{3+}), as well as six aliovalent dopants consisting of three divalent dopants (Mg^{2+}, Ca^{2+}, Sr^{2+}) and three tetravalent dopants (Ti^{4+}, Sn^{4+}, Zr^{4+}). The segregation profiles of these dopants were studied by replacing one Co^{3+} atom with a dopant and allowing the structure to relax through energy minimization while holding the simulation cell dimensions constant. The process was repeated, one by one, for each Co^{3+} in the structure, and the system's energy was computed for each dopant position. The difference between the energy of a dopant in the bulk compared to the dopant at a surface or a grain boundary was used to calculate the segregation energy, (E_{seg}).

$$\gamma = \frac{1}{2A}(E_{int} - E_{bulk}) \quad (1)$$

The surface energy or grain boundary energy (γ) of the undoped interfaces was calculated by finding the energy difference between a slab with two interfaces (surfaces/grain boundaries, (E_{int}) and a bulk slab geometry with the same number of atoms (E_{bulk}). This is shown in **Equation 1**,[41] where $2A$ accounts for the interfacial area of the two surfaces/grain boundaries.

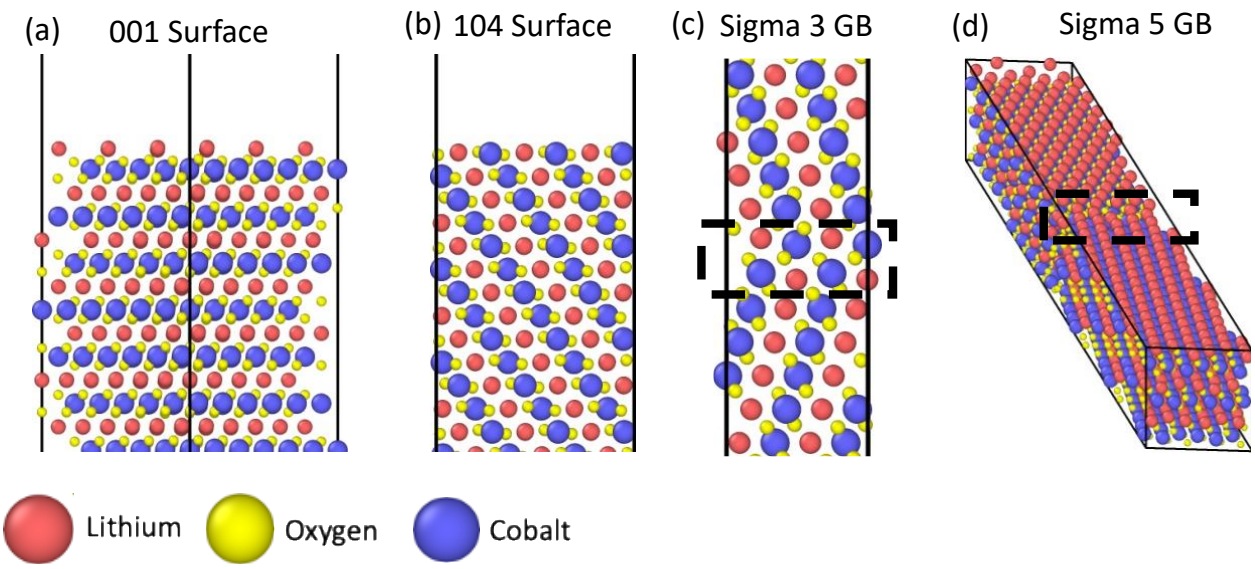

Figure 2.1. Structures of the LCO interfaces used for the atomic calculations. (a) {001} Surface, (b) {104} surface, (c) Σ3 grain boundary, (d) Σ5 grain boundary. The dashed boxes denote the coincidence site lattice of the grain boundary between the two grains.

Experimental

Doped and undoped nanoparticles of LCO were synthesized by adapting protocols developed by Okubo et al.[3] The coprecipitation method was performed by dissolving 20 mmol of $Co(NO_3)_2 \cdot 6H_2O$ into 100 mL of deionized (DI) water and preparing a 100 mL 5 M NaOH solution. For the doped nanoparticles, cobalt nitrate amount was reduced and replaced with 1 or 2 mole percent of the dopant in the nitrate form. The nitrate solution was slowly added to the basic NaOH solution to precipitate the $Co(OH)_2$ nanoparticles and then diluted into 1,800 mL of DI water. The diluted suspension was oxidized by bubbling air through the stirred suspension for 48 hours to yield the CoOOH nanoparticles. The CoOOH nanoparticles were centrifuged and washed with DI water five times and dried at 80°C overnight. The precipitates were ground in a mortar and pestle, and 500 mg was stirred into a 133 mL aqueous solution containing 1 M LiOH. The suspension was added to a 200 mL stainless steel autoclave with a PTFE liner and placed in

a furnace. The furnace was heated to 180°C at 0.5°C/min and held for 12 hours, then the autoclave was cooled at 1°C/min to 100°C and removed to cool at room temperature. The LCO precipitate was washed and centrifuged in water four times and dried at 80°C overnight. X-ray diffraction patterns were obtained with a Bruker AXS D8 Advance powder diffractometer (CuKα radiation, λ=1.5406 Å) at 40 kV and 40 mA. The Jade MDI software was used to confirm crystallographic phases and lattice constants. Crystallite sizes were calculated using the Scherrer equation using whole profile fitting.[42] Raman spectra were collected on a Renishaw Confocal Raman Microscope with a 785 nm laser at 50% intensity and 30 second measurement time. The Scanning Transmission Electron Microscopy (STEM) coupled with Electron Energy Loss Spectroscopy (EELS) revealed the morphology of the nanoparticles and mapped dopant distribution. JEOL Grand ARM 300CF equipped with Gatan GIF Quantum with K2-summit was used for the study, operating at 300keV.

Results: Atomistic Simulations

The first studies focused on the segregation potential of isovalent and aliovalent dopants on the minimized LCO surface structures. **Figure 2.2** shows an example segregation profile acquired for La^{3+} at the nonpolar {104} surface. The plot shows the minimized energy of the system versus the dopant position in the crystal structure. Each cobalt atom was substituted by La^{3+} one at a time and the structural energy minimized to evaluate the most favorable replacement site. The presented graph had surfaces on both sides of the cell, at +24 Å and -24 Å, with the positions near 0 Å representing the crystal bulk. In these calculations, the dopant minimizes the system energy further when placed near the surfaces. The energy difference between the state with the dopant replaced in the bulk value and the surface substituted dopants gives the segregation energy for the individual atom, which is 5.7 eV for La^{3+} at the {104}

surface. These simulations also explain the energetic trends and associated structural arrangements at and near the surface regions. For example, as seen in **Figure 2.2**, La^{3+} ions located at the surface and in the second atomic layer from the surface both protrude outwards toward the surface. The behavior shifts the dopant from the cobalt site and can displace other ions around it. The bulk energy values are nearly achieved when La^{3+} is at the third atomic layer from the surface, and the dopant remains close to the initial cobalt position. The relative asymmetry in the plot between surfaces, particularly for the 2nd and 3rd internal atomic layers, refers to local energy minima associated with the large ionic radius of La^{3+}. Small shifts in the La^{3+} positions may impact the stability of neighboring sites and, therefore, the system's overall energy. However, the primary conclusions regarding the most stable sites and the segregation energy are similar for both surfaces.

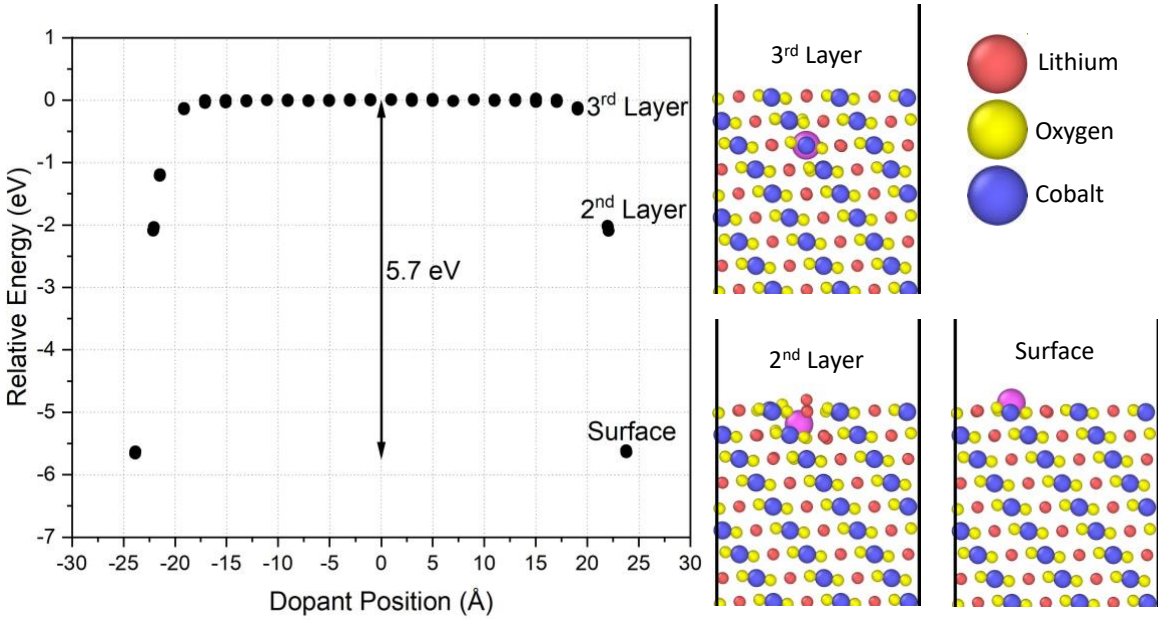

Figure 2.2. Segregation profile of La3+ doping each cobalt position in the {104} surface structure. The structure has two surfaces at either side of the simulation cell. The images depict the dopant position near the top surface at 23.8Å.

Figure 2.3 shows an example of the energy profile when doping LCO with La^{3+} in the presence of Σ3 grain boundaries. This profile illustrates two grain boundaries, with one in the middle of the structure at 0 Å and another located on the edges of the cell created as a consequence of the periodic boundary conditions. Similar to the surface case, La^{3+} promotes lower energy to the system when segregated to the grain boundary regions. This case results in spontaneous segregation energy of 3.3 eV, which is slightly lower than the {104} surface and highlights that the dopants may have different affinities for different interfaces based on the thermodynamic stability and coordination of the atoms at the given interface. The calculations also provide insights into the favorable dopant positions. For the Σ3 grain boundary, the system shows the lowest energy when the atoms sit exactly at the interface. However, if substituted in the second atomic layer from the interface, the dopant causes an increase in the energy, suggesting this substitution is less likely to occur. Since the unfavorable energy is mirrored on both sides of the grain boundary, the phenomenon creates an energetic trap that should limit the dopant mobility across grain boundaries. The pattern was observed for all tested dopants, but the magnitude of the second layer energy deviation depended on their ionic radius. In general, dopants with larger ionic radii, such as lanthanum, presented higher segregation energies (~3.3 eV) and higher energy aberration in the second layer (~0.4 eV), while smaller dopants, such as scandium, showed lower segregation energies (~2.0 eV) and lower energy aberrations (~0.3eV).

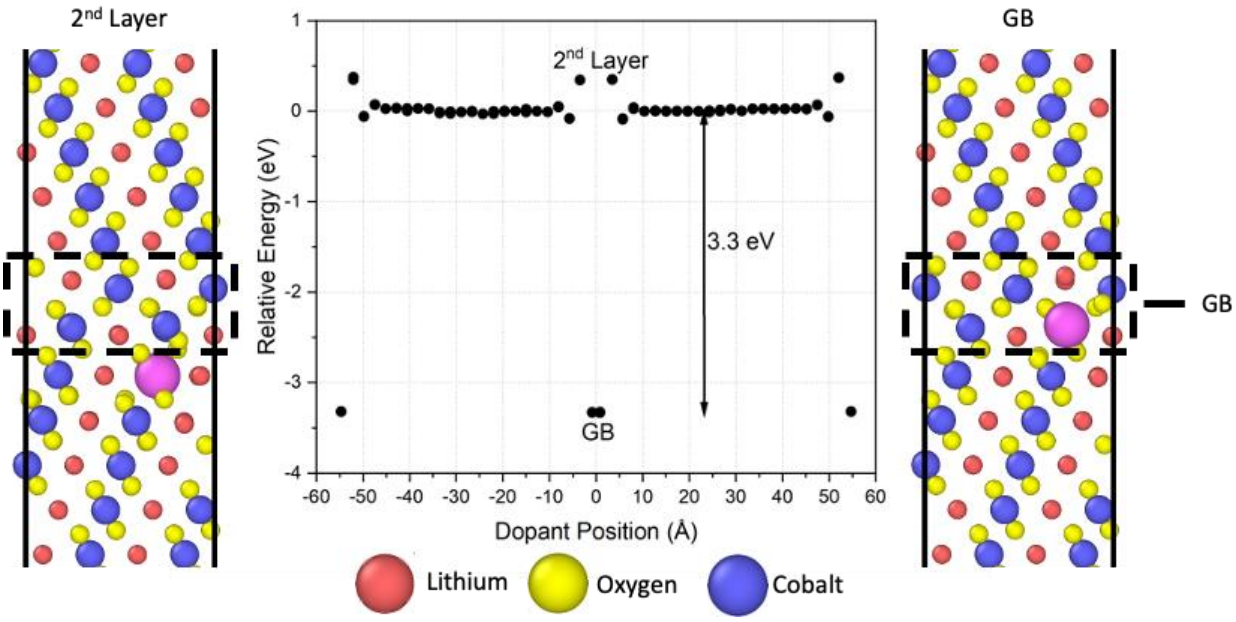

Figure 2.3. Segregation profile of La3+ doping each cobalt position in the Σ3 grain boundary structure. The structure has a grain boundary at the center and a periodic boundary at either end of the simulation cell. Images depict the dopant position at the center boundary and in the layer adjacent to the GB.

Figure 2.4 shows the compiled results of the segregation energy plotted against the ionic radius of the isovalent dopants for the two surfaces and two grain boundaries. The segregation energy increases with the ionic size of the dopant with a clear, albeit different, linear trend for each of the interfaces in the tested range of ionic radii. The linear behavior likely relates to the elastic strain induced by the dopants when in solid solution and the respective ability of the interfaces to accommodate the dopant at the less coordinated and more disordered placement. The ability of an interface to accommodate a foreign ion is related to its intrinsic thermodynamic stability. According to DFT studies by Kramer and Ceder, the {001} surface is one of the most stable surface planes in the LCO structure, with a theoretical surface energy of 1.00 J/m^2 for the

termination with a one-half monolayer of lithium at the surface.[35] Their study also points out the {104} surface is one of the most stable nonpolar surfaces because it has minimal coordination loss compared to other nonpolar surfaces. However, it does have a slightly higher surface energy of 1.05 J/m^2 compared to the polar {001} surface. This difference could be the cause for the stronger thermodynamic driving force for segregation to the {104} surface. This driving force leads to higher segregation energies to {104} surfaces, a consequent more significant reduction in the surface energy, and an overall more thermodynamically favorable accommodation.

In the present study, the calculated surface energies from **Equation 1** were 2.21 J/m^2 for {001} and 1.75 J/m^2 for {104} surfaces. Despite the numerical differences when compared to Kramer and Ceder's report[35] and other first-principles DFT studies,[43] we also found the surface energies to be close in relative values, with {001} surface having higher energy. The fact DFT yields lower energies indicates a limitation of the used potentials in the present work. However, those were the only set of potentials that both predicted a stable LCO surface structure and had interactions for the numerous dopant species considered in this study. The relative consistency with recent results, the self-consistency, and experimental confirmations presented later in this work indicate that although the absolute values may be off, the predicted basic physical trends concerning segregation are reliable.

The two studied grain boundaries, Σ3 and Σ5, also presented energetic differences affecting the segregation trends. At the Σ3, the atoms are more coordinated, and the structure shares more atoms at the coincidence site lattice. **Equation 1** enabled the estimation of the difference in grain boundary energy between the two structures by using the bulk energy of a slab structure with no interfaces and the same number of atoms. From this calculation, the Σ3 boundary showed excess energy of 0.59 J/m^2, while the energy for Σ5 boundary was 3.63 J/m^2.

The Σ5 boundary shows significantly higher energy than the Σ3 and supports the inference that the Σ5 is more disordered and atomically less coordinated. High energies are consistent with the covalent nature of $LiCoO_2$. The directional characteristic of covalent bonds increases energies due to the significant bond angle distortions. The higher energy leads to stronger segregation potentials, as dopants can alleviate the local stresses by increasing coordination.

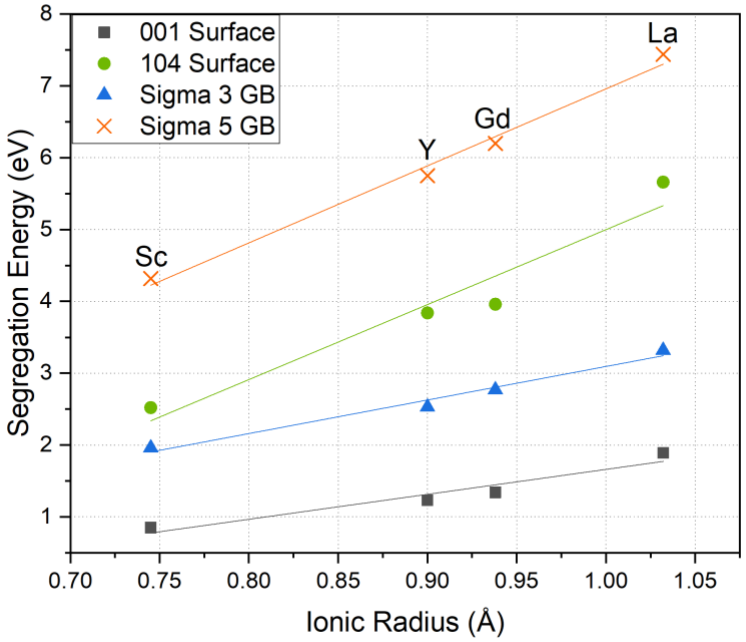

Figure 2.4. Calculated segregation energies of trivalent dopants (Sc^{3+}, Y^{3+}, Gd^{3+}, La^{3+}) plotted against ionic radius for all four constructed interfaces.

In addition to the isovalent doping, several aliovalent ions (Mg^{2+}, Ca^{2+}, Sr^{2+}, Ti^{4+}, Sn^{4+}, Zr^{4+}) were tested to study the impact of dopant oxidation state on the segregation behavior. **Figure 2.5a** shows the segregation potential of all ten dopants as a function of the ionic radius for the Σ3 and Σ5 grain boundaries, while **Figure 2.5b** shows the segregation potentials for the studied surfaces. A few unique cases from the simulations with aliovalent dopants arose during

the dopant replacements and those are discussed briefly in the Appendix (**Figure 2.A1**). The linear trend of increasing segregation energy with ionic radius remained consistent for all oxidation states of the dopants. However, the linear dependence is different for each oxidation state and interface, providing interesting insights for dopant selection.

One observation is that the segregation energy increases as the oxidation state of the dopant increases. For example, dopants of similar ionic radius but different charge states, e.g. Mg^{2+} and Zr^{4+}, had segregation energies scaling with the charges, i.e. 0.7 eV and 2.0 eV, respectively, for the Σ3 boundary. Consistently, the Σ5 boundary again had higher segregation energies than the Σ3 boundary due to the higher structural disorder, but similar trends with the oxidation state of dopants. Interestingly, results show that all dopants, regardless of the size and charge, had favorable segregation energy. The doped surface structures shown in **Figure 2.5b** exhibit similar linear trends to the grain boundaries. This implies all could potentially be used to control interfacial energies, but some had a more pronounced impact.

It is tempting to select the dopants with the highest computed segregation energies, La^{3+} or Sr^{2+}, to attempt an interfacial engineering protocol as those would present the highest thermodynamic driving force. However, one should keep in mind that the presented atomistic simulations do not consider the possibility of nucleation of a second phase. As discussed in more detail by Castro,[44] a saturation of interfacial sites by a dopant can eventually lead to the formation of second phases. The formation of a precipitate is typically undesirable as it compromises electrochemical properties. This was recently observed in La^{3+} doped $MgAl_2O_4$, in which a lanthanum-rich precipitate formed after saturation of the interfacial sites.[45]

While the extremes of segregation energies may not be positive, similarly, low segregation energies, as found for Ti^{4+}, which is much closer to the ionic radius of Co^{3+}, may not

have a high enough segregation potential at dilute concentrations and will provide very little stability enhancement at the interfaces. Additionally, Al^{3+} and V^{5+} dopants were studied due to their small ionic size and ability to enhance some aspects of battery stability (**Table 2.A1** and **Figure 2.A2**).[46,47] The aluminum dopant shows low segregation energies for both the {104} surface and Σ3 boundary, which follows what has been observed in the literature.[46] The aluminum dopant has no electrostatic charge or elastic strain to drive the dopant to the interface and therefore remains a bulk dopant. The vanadium also remains a bulk dopant for the {104} surface, but also appears to be thermodynamically unstable at the surface. This could be due to the limitation of a different O^{2-}-O^{2-} potential parameter or a strong repulsion on the surface from the higher oxidation state ion. There is a small segregation energy of 0.86 eV for the Σ3 boundary that shows the grain boundaries ability to accommodate the excess charge from the vanadium ion. There are mixed results on the ability of vanadium doping to improve electrochemical performance, however the impact of vanadium as an interfacial dopant in nanoscale materials could be vastly different from bulk doping cathodes.[48] The segregation energies also show that ions of a similar ionic size to cobalt can still segregate due to the higher oxidation state of the dopant, but the driving force may be small depending on the oxidation state.

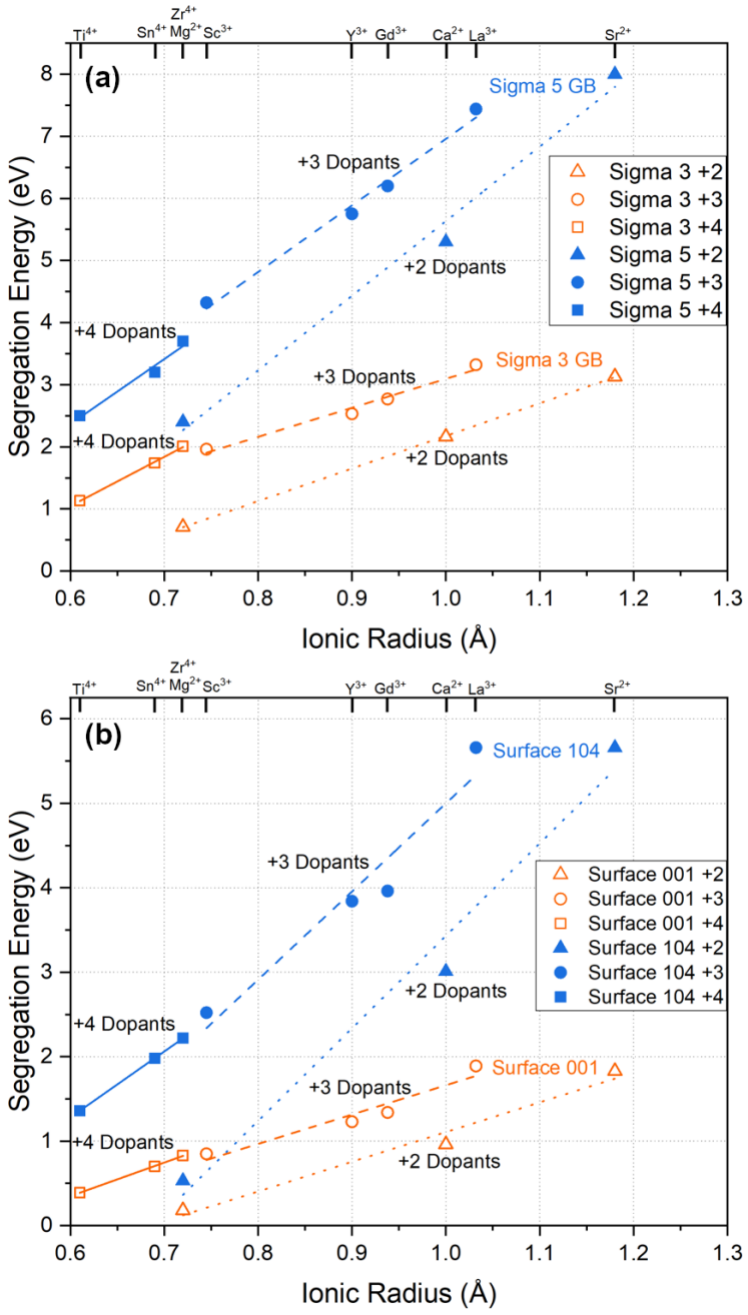

Figure 2.5. Segregation energies of all divalent, trivalent, and quadrivalent dopants as a function of ionic radius for (a) the two constructed grain boundary structures and (b) the two surface structures.

Results: Experimental

To confirm the segregation predictions, we selected La^{3+} as a dopant at a concentration low enough not to saturate the available interfacial areas assuming the limit as a monolayer coverage (below 2 mol%). Nanoparticles of lanthanum doped and undoped LCO were synthesized through a hydrothermal synthesis method. The XRD patterns of the undoped and doped LCO are shown in **Figure 2.6** and show no evidence of secondary phase formation due to the dopant. Traces of Co_3O_4 secondary phase are present in all three samples, but compared to the intensity of the LCO peaks, the amount of the second phase is estimated to be below 1 wt.% by Rietveld refinement.[49] Raman spectra of the doped and undoped LCO in **Figure 2.7** also provide support for no secondary phases caused by excess dopant segregation. The spectra confirm the presence of LCO with the characteristic peaks around 485 and 495 cm^{-1}.[50] The Co_3O_4 secondary phase peaks were also confirmed in both samples.[51] The Raman measurements corroborate the XRD results and show none of the expected lanthanum secondary phases (La_2O_3 and $LaCoO_3$) forming from excess dopant segregation.[52,53] **Table 2.2** shows the calculated lattice parameters from a whole pattern fitting. The synthesized LCO can crystallize into either a layered or spinel-type structure with similar XRD patterns.[54] Gummow and Thackeray showed that a *c*/*a* parameter of ~5.0 indicates a layered type structure, and values closer to 4.9 indicate a spinel-type form. The doped and undoped *c*/*a* parameters are close to 5.0 and show that the doped system maintains the layered structure. The lanthanum doping caused a minimal effect on parameter *a*, and a slight decrease on parameter *c*. In truth, dopants forming a solid solution within the LCO structure would cause lattice expansion, as observed by Wang et al. when doping with Mn^{3+} or Ni^{2+}.[55] That would be particularly expected in this case since La^{3+} has a

significantly larger ionic radius than Co^{3+}. Therefore, the lack of structural expansion is already indirect evidence of segregation.

The lattice shrinkage could be attributed to the stress induced by the segregated dopants or the observed reduction in crystallite size, as seen in **Table 2.2**. The interfacial energy reduction caused by segregation inhibits coarsening driving force independent of the growth mechanisms, leading to smaller crystallite and particle sizes at a given annealing temperature.[56,57] The results are consistent with the BET surface area shown in **Table 2.2**, indicating higher surface areas for the doped samples due to surface stabilization.

The XRD patterns also show La^{3+} doping changes in the relative intensities of certain planes in the LCO structure. In undoped LCO, the ratio of the {104} peak to the {003} is 0.90, but for the doped samples, it is above 1.05. The observation is consistent with the work from Okubo et al. where they show the {003} peak intensity decreases as particle size decreases due to the nanoplatelet morphology of the particles.[3]

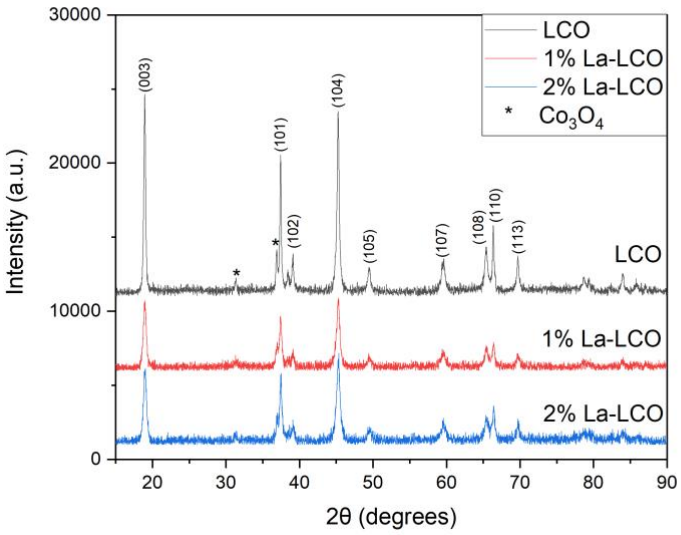

Figure 2.6. X-ray diffraction patterns of 600°C calcined undoped LCO, 1 mol%, and 2 mol% lanthanum doped LCO.

Table 2.2. Calculated lattice parameters, peak ratios, and crystallite sizes from X-ray diffraction and BET surface area for La doped and undoped LCO calcined at 600°C.

	LCO	1% La-LCO	2% La-LCO
a (Å)	2.8174	2.8175	2.8177
c (Å)	14.0702	14.0664	14.0656
c/*a*	4.994	4.992	4.992
{104}/{003}	0.90	1.05	1.18
Crystallite Size (nm)	28.1	18.1	17.8
BET Surface Area (m^2/g)	20.3	29.1	25.6

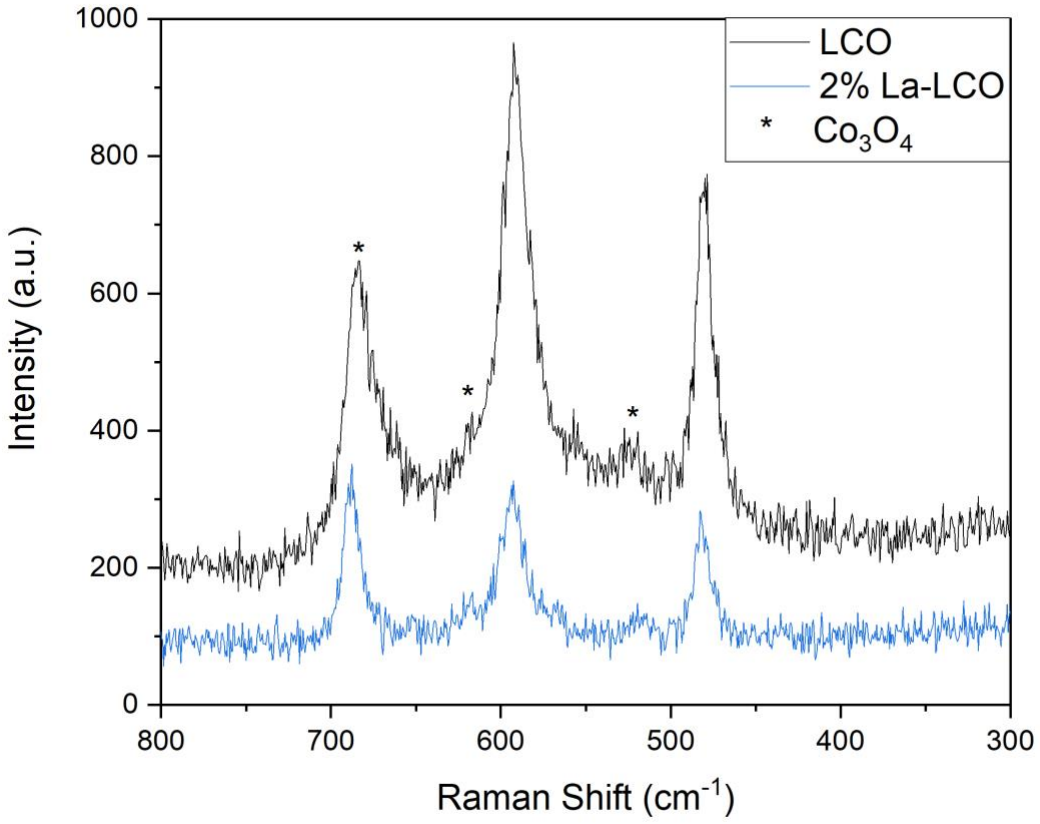

Figure 2.7. Raman spectra of LiCoO2 calcined at 300°C after synthesis and 2 mol% lanthanum doped LiCoO2 calcined at 600°C.

Figure 2.8 shows the STEM and EELS images of the 2% La doped LCO nanoparticles after calcination at 600 °C. **Figure 2.8a** and **8c** confirm the nanoscale dimension and show the expected nanoplatelet morphology with varying thicknesses of 10-20 nm. **Figure 2.8a** indicates particles are partially connected, with a grain boundary indicated by arrows. **Figure 2.8b** shows the EELS composed color mapping demonstrating a concentrated green color around the edges of the particles, depicting the La^{3+} enrichment at both the surfaces and the grain boundaries. The center of the particles had a more purple hue because of the higher fraction of cobalt (blue) and oxygen (red). **Figure 2.8b** still shows lanthanum atoms in the center of the nanoparticles. However, most of the nanoparticles in the image are lying flat and showing the {001} surface on the top and bottom of the particle.[43] The platelike morphology makes it challenging to determine if the lanthanum is at the {001} plane or remains in the bulk structure since electrons are transmitting through the sample. **Figure 2.8c** shows a particle oriented perpendicularly, allowing visualization axially along with the *a* parameter to identify the fringes of the *c*-spacing consistently with LCO layered structure. While the top surface is attributed to {001} plane, the edges of the particles can be assigned to {104} and {012} surfaces.[43] **Figure 2.8c** also shows evidence of lanthanum enrichment along the {001} surface plane indicated by the phase contrast between cobalt and lanthanum atoms. The segregation of La^{3+} to {001} is confirmed in the color mapping in **Figure 2.8d**.

Figure 2.9a shows the box scan measurement of the {001} surface from **Figure 2.8d** and displays the highest peak intensity of lanthanum at 8 nm near the surface of the particle. At the same distance, the cobalt and oxygen normalized intensity dips near the surface, which confirms the lanthanum enrichment near the {001} surface. Note that because the particles overlap (see box in **Figure 2.8d**), the scan shows positive signals for O, Co and La on either side of the peak

position despite the fact the measurement is looking at a surface. Atoms that are from background particles are marked by hollow symbols in the box scan plots to allow better visualization.

Figure 2.9b shows the box scan results from the {104} surface shown in **Figure 2.8d**. This scan also shows an enrichment of La near the surface and confirms the thermodynamic driving force directing La atoms to all interfaces in LCO. It appears the lanthanum has such a strong segregation potential that there is no preferential doping of specific interfaces and it distributes across all surfaces and grain boundaries shown here. This conclusion matches the atomistic calculations of lanthanum segregation that revealed lanthanum had one of the highest segregation energies compared to the dopants studied in all four of the constructed interfaces. Noteworthy, in both segregation profiles one observes that oxygen dips when La peaks at the interfacial regions. That suggests that La does not simply replace Co, as assumed in our atomistic calculations, but that more complex reactions might be occurring. However, the observed experimental segregations confirm the trends regarding the relative segregation potential of different dopants are reasonable despite this approximation.

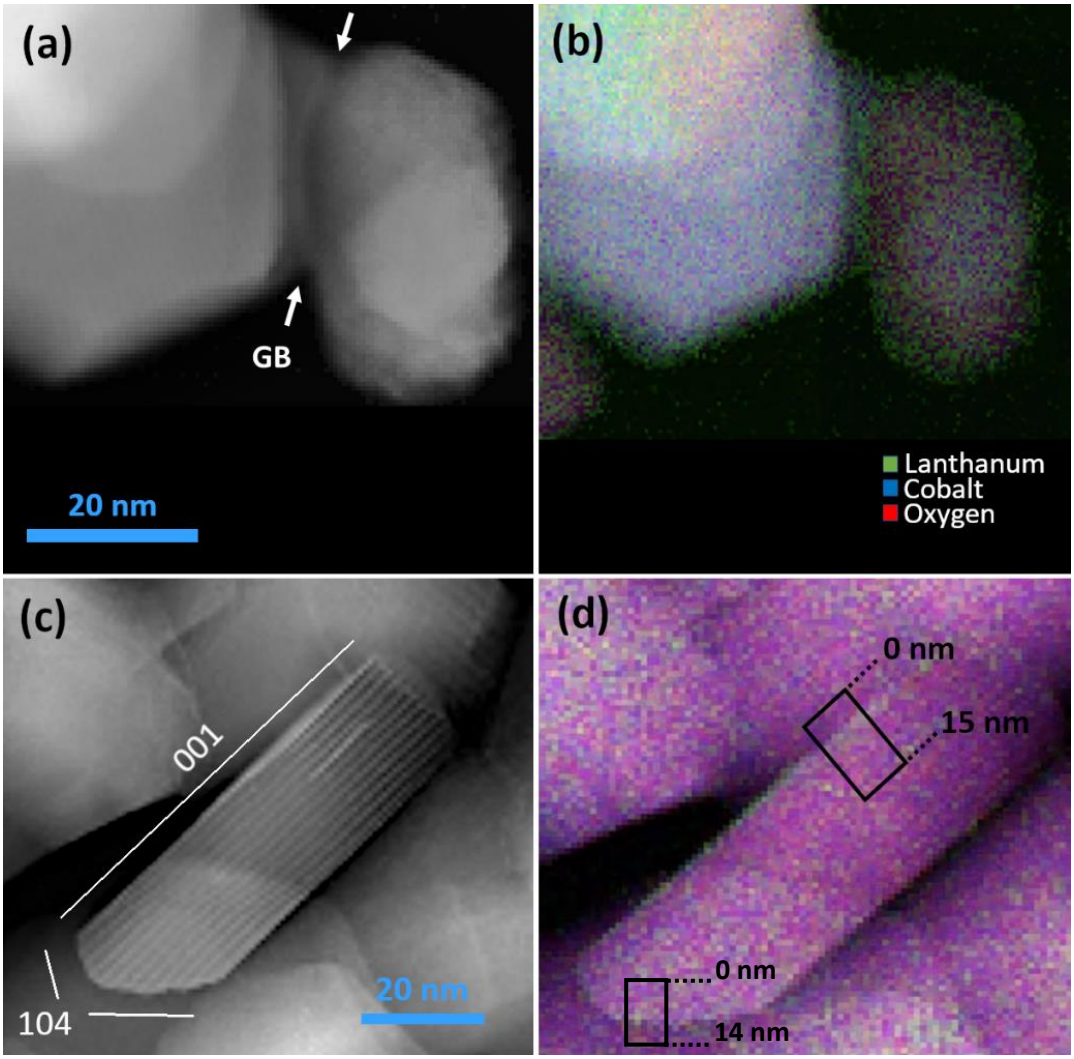

Figure 2.8. STEM-EELS images of 2% La doped LCO calcined at 600°C. (a) and (c) show the STEM ADF images of the particles and (b) and (d) show the EELS color mapping of the particles for lanthanum, cobalt, and oxygen. **Figure 2.8d** shows the elemental box scans performed at the interfaces with the results shown in **Figure 2.9a** and **9b**.

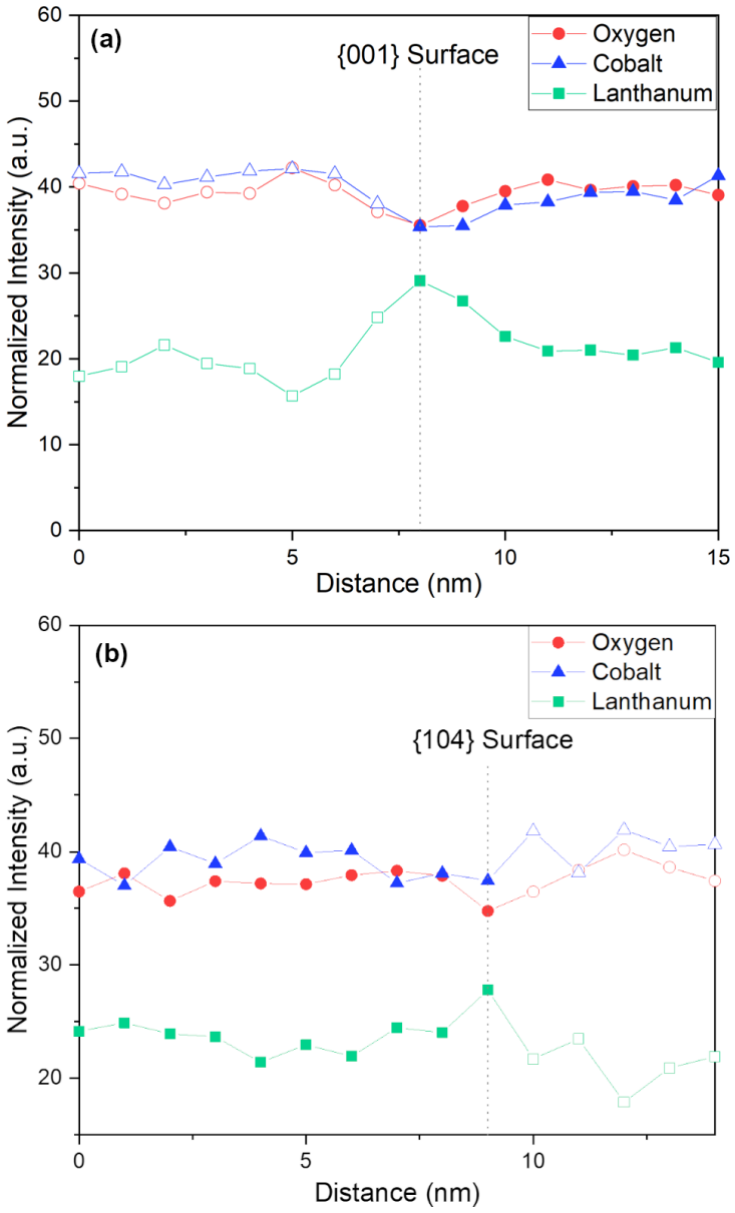

Figure 2.9. Box scans plotting the atomic concentrations of lanthanum, cobalt, and oxygen of the particles shown in **Figure 2.8d**. (a). Box scan of the {001} surface and the dotted line at the 8 nm position portrays the lanthanum enrichment near the {001} surface of the nanoplatelet morphology shown in the figure. (b) Box scan of the {104} surface with the dotted line at 9 nm position portraying the position of the surface. The hollow symbols show the data from the background particles below the platelet being measured and solid symbols depict the atomic concentrations of the platelet shown in **Figure 2.8d**.

Discussion

The atomistic simulations enabled screening over many dopants that could potentially segregate to surfaces and grain boundaries of LCO. The motivation was to find dopants that would potentially lower excess energies in the system, enabling greater thermodynamic stability in nanocrystalline cathodes. Out of the proposed dopants, La^{3+} had one of the highest segregation energies and therefore was selected for the experimental studies. The synthesis and characterization demonstrated La^{3+} ions segregated to surfaces and grain boundaries as predicted by the simulations. The results are very encouraging since a simulation-informed design of experiments provides a methodology for relatively quickly and inexpensively streamlining experimental investigations. The method helps overcome the existing challenges in obtaining experimental thermodynamic data on interfacial energies and segregation enthalpies in oxides, and could open new opportunities in other complex oxides for batteries or other applications.

Although segregation is not a new concept in cathode doping, the connection between ion segregation and interface thermodynamic stability makes this work very relevant to the development of stable nanomaterials (and micro) for lithium ion battery technologies, which can extend battery lifetime.[58] Additionally to improve cyclability, the computational model helps determine the tendencies of segregation for different dopant chemistries to specific interfaces for the design of purposefully anisotropic particles. In LCO, the {001} surface is not an active surface for lithium diffusion and the {104} surface is one of the most active surfaces since lithium ions prefer to move along layers and not across cobalt layers.[59] This model can design specific morphology particles with an optimized fraction of {104} surfaces that in turn will enhance the lithium diffusion and battery performance. Additionally, it is reported that lithium diffusion along grain boundaries can play a critical role in the electrochemical performance of

cathodes.[60,61] The stabilization of grain boundary networks can be critical for preventing failure mechanisms like intergranular cracking or coarsening and morphological changes during electrochemical cycling.[1,62-64] In theory, future models could be developed to design ionically and electronically conductive grain boundaries for fast lithium and electron transport. This type of energetic and morphological engineering is only possible due to the segregation behavior of dopants in nanoscale materials and more thermodynamic understanding is necessary.

In truth, there were a number of assumptions and limitations in the atomistic simulations that enabled the extensive search through ten different dopants with varying ionic size and charge across the four structures considered. One of the most relevant approximations in the interatomic potentials was fixing the cobalt oxidation state to the trivalent state. It is well known that the cobalt can assume several oxidation states in LCO, especially during lithium cycling. Hence, some changes to segregation energy values may occur if the cobalt was allowed to change oxidation state near an interface or in the presence of aliovalent dopants. However, despite multiple attempts, the study could not find interatomic potential parameters for a charge transfer model that could accommodate the wide range of studied dopants. A charge transfer potential that could accommodate a subset of dopants and delithiated structures could provide insight into segregation behavior as cathodes are cycled within the battery. Related to this point, particularly when aliovalent dopants are considered, other charge-compensating reactions might also occur to stabilize the incorporation of those dopants. Indeed, past work has shown such effects at grain boundaries.[65] However, we expect that our results are still useful for identifying dopants with higher tendencies to segregate to surfaces and interfaces. Finally, only low surface energy surfaces and low index grain boundaries were evaluated for this work. It would be

valuable for future work to construct higher energy interfaces and more surfaces to look for other trends in more complex structures and as a predictive tool for morphology evolution.

Conclusion

Atomistic simulations were used to construct four interfaces, two low energy surfaces and two low index grain boundaries, and study the dopant segregation behavior. By inserting dopants into the bulk of the structure and at the interface, the segregation energies of ten dopants with different ionic radii and charges were calculated. The results demonstrated the linear dependence of segregation energy on the ionic radius of the dopant, where dopants with larger ionic radius had higher segregation energies. Additionally, dopants with a higher oxidation state exhibited higher segregation energy than other dopants of the same ionic size but lower oxidation state. For example, Zr^{4+} and Mg^{2+} have similar ionic radius, but Zr^{4+} had larger segregation energies for all four interfaces studied. The magnitude of the segregation energy was highly dependent upon the specific surface and grain boundary structure. This behavior shows the thermodynamic driving forces of each dopant depend not only on the chemical nature of the dopant, but also on the detailed interfacial atomic environment.

The results were validated by experimentally synthesizing LCO nanoparticles with a dopant showing favorable segregation energy, lanthanum, and observing the segregation behavior with STEM-EELS. The hydrothermal synthesis yielded platelike nanoparticles and the STEM-EELS images revealed clear lanthanum segregation to both surfaces, {001} and {104}, and grain boundaries. The consistency with the simulation data suggests that, despite the assumptions and approximations, atomistic modelling is a viable tool for informing the experimental design and limiting the number of synthesis experiments during dopant selection for improving performance of nanocrystalline materials.

References

(1) Hausbrand, R.; Cherkashinin, G.; Ehrenberg, H.; Gröting, M.; Albe, K.; Hess, C.; Jaegermann, W. Fundamental Degradation Mechanisms of Layered Oxide Li-Ion Battery Cathode Materials: Methodology, Insights and Novel Approaches. *Mater. Sci. Eng. B* **2015**, *192*, 3–25. https://doi.org/https://doi.org/10.1016/j.mseb.2014.11.014.

(2) Bruce, P. G.; Scrosati, B.; Tarascon, J. M. Nanomaterials for Rechargeable Lithium Batteries. *Angew. Chemie - Int. Ed.* **2008**, *47* (16), 2930–2946. https://doi.org/10.1002/anie.200702505.

(3) Okubo, M.; Hosono, E.; Kim, J.; Enomoto, M.; Kojima, N.; Kudo, T.; Zhou, H.; Honma, I. Nanosize Effect on High-Rate Li-Ion Intercalation in LiCoO2 Electrode. *J. Am. Chem. Soc.* **2007**, *129* (23), 7444–7452. https://doi.org/10.1021/ja0681927.

(4) McHale, J. M.; Auroux, A.; Perrotta, A. J.; Navrotsky, A. Surface Energies and Thermodynamic Phase Stability in Nanocrystalline Aluminas. *Science (80-.).* **1997**, *277* (5327), 788–791.

(5) Castro, R. H. R.; Tŏrres, R. B.; Pereira, G. J.; Gouvěa, D. Interface Energy Measurement of MgO and ZnO: Understanding the Thermodynamic Stability of Nanoparticles. *Chem. Mater.* **2010**, *22* (8), 2502–2509. https://doi.org/10.1021/cm903404u.

(6) Bangham, D. H. The Gibbs Adsorption Equation and Adsorption on Solids. *Trans. Faraday Soc.* **1937**, *33*, 805–811.

(7) Kirchheim, R. Reducing Grain Boundary, Dislocation Line and Vacancy Formation Energies by Solute Segregation. I. Theoretical Background. *Acta Mater.* **2007**, *55* (15), 5129–5138. https://doi.org/10.1016/j.actamat.2007.05.047.

(8) Nakajima, K.; Souza, F. L.; Freitas, A. L. M.; Thron, A.; Castro, R. H. R. Improving

Thermodynamic Stability of Nano-LiMn2O4for Li-Ion Battery Cathode. *Chem. Mater.* **2021**, *33* (11), 3915–3925. https://doi.org/10.1021/acs.chemmater.0c04305.

(9) Chang, C. H.; Gong, M.; Dey, S.; Liu, F.; Castro, R. H. R. Thermodynamic Stability of SnO2 Nanoparticles: The Role of Interface Energies and Dopants. *J. Phys. Chem. C* **2015**, *119* (11), 6389–6397. https://doi.org/10.1021/JP512969K/ASSET/IMAGES/JP512969K.SOCIAL.JPEG_V03.

(10) Gouvêa, D.; Pereira, G. J.; Gengembre, L.; Steil, M. C.; Roussel, P.; Rubbens, A.; Hidalgo, P.; Castro, R. H. R. Quantification of MgO Surface Excess on the SnO2 Nanoparticles and Relationship with Nanostability and Growth. *Appl. Surf. Sci.* **2011**, *257* (9), 4219–4226. https://doi.org/10.1016/J.APSUSC.2010.12.023.

(11) Wang, K.; Wan, H.; Yan, P.; Chen, X.; Fu, J.; Liu, Z.; Deng, H.; Gao, F.; Sui, M. Dopant Segregation Boosting High-Voltage Cyclability of Layered Cathode for Sodium Ion Batteries. *Adv. Mater.* **2019**, *31* (46). https://doi.org/10.1002/ADMA.201904816.

(12) Wu, L.; Dey, S.; Mardinly, J.; Hasan, M.; Castro, R. H. R. Thermodynamic Strengthening of Heterointerfaces in Nanoceramics. *Chem. Mater.* **2016**, *28* (9), 2897–2901. https://doi.org/10.1021/acs.chemmater.6b00074.

(13) Bokov, A.; Zhang, S.; Feng, L.; Dillon, S. J.; Faller, R.; Castro, R. H. R. Energetic Design of Grain Boundary Networks for Toughening of Nanocrystalline Oxides. *J. Eur. Ceram. Soc.* **2018**, *38* (12), 4260–4267. https://doi.org/10.1016/j.jeurceramsoc.2018.05.007.

(14) Arumugam, D.; Paruthimal Kalaignan, G. Synthesis and Electrochemical Characterizations of Nano-La 2O3-Coated Nanostructure LiMn2O4 Cathode Materials for Rechargeable Lithium Batteries. *Mater. Res. Bull.* **2010**, *45* (12), 1825–1831. https://doi.org/10.1016/j.materresbull.2010.09.021.

(15) Maram, P. S.; Costa, G. C. C.; Navrotsky, A. Experimental Confirmation of Low Surface Energy in LiCoO 2 and Implications for Lithium Battery Electrodes . *Angew. Chemie* **2013**, *125* (46), 12361–12364. https://doi.org/10.1002/ANGE.201305375.

(16) Yan, P.; Zheng, J.; Liu, J.; Wang, B.; Cheng, X.; Zhang, Y.; Sun, X.; Wang, C.; Zhang, J.-G. Tailoring Grain Boundary Structures and Chemistry of Ni-Rich Layered Cathodes for Enhanced Cycle Stability of Lithium-Ion Batteries. *Nat. Energy*. https://doi.org/10.1038/s41560-018-0191-3.

(17) Moriwake, H.; Kuwabara, A.; Fisher, C. A. J.; Huang, R.; Hitosugi, T.; Ikuhara, Y. H.; Oki, H.; Ikuhara, Y. First-Principles Calculations of Lithium-Ion Migration at a Coherent Grain Boundary in a Cathode Material, LiCoO2. *Adv. Mater.* **2013**, *25* (4), 618–622. https://doi.org/10.1002/ADMA.201202805.

(18) Plimpton, S. Fast Parallel Algorithms for Short-Range Molecular Dynamics. *Journal of Computational Physics*. 1995, pp 1–19. https://doi.org/10.1006/jcph.1995.1039.

(19) Buckingham, R. A. The Classical Equation of State of Gaseous Helium, Neon and Argon. *Proc. R. Soc. London. Ser. A. Math. Phys. Sci.* **1938**, No. 1938, 264–283.

(20) Ewald, P. P. Die Berechnung Optischer Und Elektrostatischer Gitterpotentiale. *Ann. Phys.* **1921**, *369* (3), 253–287. https://doi.org/10.1002/andp.19213690304.

(21) Lee, E.; Lee, K. R.; Lee, B. J. An Interatomic Potential for the Li-Co-O Ternary System. *Comput. Mater. Sci.* **2018**, *142*, 47–58. https://doi.org/10.1016/J.COMMATSCI.2017.10.010.

(22) Kong, F.; Longo, R. C.; Liang, C.; Nie, Y.; Zheng, Y.; Zhang, C.; Cho, K. Charge-Transfer Modified Embedded Atom Method Dynamic Charge Potential for Li-Co-O System. *J. Phys. Condens. Matter* **2017**, *29* (47). https://doi.org/10.1088/1361-648X/aa9420.

(23) Hart, F. X.; Bates, J. B. Lattice Model Calculation of the Strain Energy Density and

Other Properties of Crystalline LiCoO2. *J. Appl. Phys.* **1998**, *83* (12), 7560–7566. https://doi.org/10.1063/1.367521.

(24) Cherry, M.; Islam, M. S.; Catlow, C. R. A. Oxygen Ion Migration in Perovskite-Type Oxides. *J. Solid State Chem.* **1995**, *118* (1), 125–132. https://doi.org/10.1006/jssc.1995.1320.

(25) Vives, S.; Meunier, C. Defect Cluster Arrangements and Oxygen Vacancy Migration in Gd Doped Ceria for Different Interatomic Potentials. *Solid State Ionics* **2015**, *283*, 137–144. https://doi.org/10.1016/j.ssi.2015.10.003.

(26) Ruiz-Trejo, E.; Islam, M. S.; Kilner, J. A. Atomistic Simulation of Defects and Ion Migration in LaYO3. *Solid State Ionics* **1999**, *123* (1), 121–129. https://doi.org/10.1016/S0167-2738(99)00092-2.

(27) Cormack, A. N.; Catlow, C. R. A.; Nowick, A. S. Theoretical Studies of Off-Centre Sc3+ Impurities in CeO2. *J. Phys. Chem. Solids* **1989**, *50* (2), 177–181. https://doi.org/10.1016/0022-3697(89)90415-0.

(28) Ramadan, A. H. H.; Allan, N. L.; De Souza, R. A. Simulation Studies of the Phase Stability of the Srn+1Ti NO3n+1 Ruddlesden-Popper Phases. *J. Am. Ceram. Soc.* **2013**, *96* (7), 2316–2321. https://doi.org/10.1111/jace.12300.

(29) Sun, Y.; Liu, T.; Chang, Q.; Ma, C. Study on the Intrinsic Defects in Tin Oxide with First-Principles Method. *J. Phys. Chem. Solids* **2018**, *115*, 228–232. https://doi.org/10.1016/j.jpcs.2017.12.044.

(30) Evarestov, R. A.; Bandura, A. V.; Blokhin, E. N. The Water Adsorption on the Surfaces of SrMO3 (M= Ti, Zr, and Hf) Crystalline Oxides: Quantum and Classical Modelling. *J. Phys. Conf. Ser.* **2007**, *93* (1), 012001. https://doi.org/10.1088/1742-6596/93/1/012001.

(31) Jones, A.; Islam, M. S. Atomic-Scale Insight into LaFeO3 Perovskite: Defect

Nanoclusters and Ion Migration. *J. Phys. Chem. C* **2008**, *112* (12), 4455–4462. https://doi.org/10.1021/jp710463x.

(32) Jain, A.; Ong, S. P.; Hautier, G.; Chen, W.; Richards, W. D.; Dacek, S.; Cholia, S.; Gunter, D.; Skinner, D.; Ceder, G.; Persson, K. A. Commentary: The Materials Project: A Materials Genome Approach to Accelerating Materials Innovation. *APL Materials*. American Institute of Physics Inc. July 2013, p 11002. https://doi.org/10.1063/1.4812323.

(33) Qian, D.; Hinuma, Y.; Chen, H.; Du, L. S.; Carroll, K. J.; Ceder, G.; Grey, C. P.; Meng, Y. S. Electronic Spin Transition in Nanosize Stoichiometric Lithium Cobalt Oxide. *J. Am. Chem. Soc.* **2012**, *134* (14), 6096–6099. https://doi.org/10.1021/ja300868e.

(34) Hu, L.; Xiong, Z.; Ouyang, C.; Shi, S.; Ji, Y.; Lei, M.; Wang, Z.; Li, H.; Huang, X.; Chen, L. Ab Initio Studies on the Stability and Electronic Structure of LiCoO 2 (003) Surfaces. *Phys. Rev. B - Condens. Matter Mater. Phys.* **2005**, *71* (12), 125433. https://doi.org/10.1103/PhysRevB.71.125433.

(35) Kramer, D.; Ceder, G. Tailoring the Morphology of LiCoO2: A First Principles Study. *Chem. Mater.* **2009**, *21* (16), 3799–3809. https://doi.org/10.1021/cm9008943.

(36) Tasker, P. W. The Stability of Ionic Crystal Surfaces. *J. Phys. C Solid State Phys.* **1979**, *12* (22), 4977–4984. https://doi.org/10.1088/0022-3719/12/22/036.

(37) Ceder, G.; Van Der Ven, A. Phase Diagrams of Lithium Transition Metal Oxides: Investigations from First Principles. *Electrochim. Acta* **1999**, *45* (1), 131–150. https://doi.org/10.1016/S0013-4686(99)00199-1.

(38) Hadian, R.; Grabowski, B.; Neugebauer, J. GB Code: A Grain Boundary Generation Code. *J. Open Source Softw.* **2018**, *3* (29), 900. https://doi.org/10.21105/JOSS.00900.

(39) Momma, K.; Izumi, F. VESTA 3 for Three-Dimensional Visualization of Crystal,

Volumetric and Morphology Data. *J. Appl. Crystallogr.* **2011**, *44* (6), 1272–1276. https://doi.org/10.1107/S0021889811038970.

(40) Cheng, J.; Luo, J.; Yang, K. Aimsgb: An Algorithm and Open-Source Python Library to Generate Periodic Grain Boundary Structures. *Comput. Mater. Sci.* **2018**, *155*, 92–103. https://doi.org/10.1016/j.commatsci.2018.08.029.

(41) Van Der Laag, N. J.; Fang, C. M.; De With, G.; De Wijs, G. A.; Brongersma, H. H. Geometry of {001} Surfaces of Spinel (MgAl2O4): First-Principles Simulations and Experimental Measurements. *J. Am. Ceram. Soc.* **2005**, *88* (6), 1544–1548. https://doi.org/10.1111/j.1551-2916.2005.00315.x.

(42) Patterson, A. L. The Scherrer Formula for X-Ray Particle Size Determination. *Phys. Rev.* **1939**, *56* (10), 978. https://doi.org/10.1103/PhysRev.56.978.

(43) Hong, L.; Hu, L.; Freeland, J. W.; Cabana, J.; Serdar, ‡; Ğ Ü, O.¨; Klie, R. F. Electronic Structure of LiCoO 2 Surfaces and Effect of Al Substitution. *J. Phys. Chem. C* **2019**, *123*, 8851–8858. https://doi.org/10.1021/acs.jpcc.8b11661.

(44) Castro, R. H. R. Interfacial Energies in Nanocrystalline Complex Oxides. *Curr. Opin. Solid State Mater. Sci.* **2021**, *25* (3), 100911. https://doi.org/https://doi.org/10.1016/j.cossms.2021.100911.

(45) Hasan, M. M.; Dholabhai, P. P.; Dey, S.; Uberuaga, B. P.; Castro, R. H. R. Reduced Grain Boundary Energies in Rare-Earth Doped MgAl2O4 Spinel and Consequent Grain Growth Inhibition. *J. Eur. Ceram. Soc.* **2017**, *37* (13), 4043–4050. https://doi.org/10.1016/j.jeurceramsoc.2017.04.073.

(46) Myung, S. T.; Kumagai, N.; Komaba, S.; Chung, H. T. Effects of Al Doping on the Microstructure of LiCoO2 Cathode Materials. *Solid State Ionics* **2001**, *139* (1–2), 47–56.

https://doi.org/10.1016/S0167-2738(00)00828-6.

(47) Hu, Z., Wang, L., Luo, Y., Wei, Q., Yan, M., Zhou, L., Mai, L. Vanadium-Doped LiNi 1/3 Co 1/3 Mn 1/3 O 2 with Decreased Lithium/Nickel Disorder as High-Rate and Long-Life Lithium Ion Battery Cathode. *Sci. Adv. Today* **2015**, *1*, 25218.

(48) Needham, S. A.; Wang, G. X.; Liu, H. K.; Drozd, V. A.; Liu, R. S. Synthesis and Electrochemical Performance of Doped LiCoO2 Materials. *J. Power Sources* **2007**, *174* (2), 828–831. https://doi.org/10.1016/J.JPOWSOUR.2007.06.228.

(49) Rodriguez-Carvajal, J. FULLPROF: A Program for Rietveld Refinement and Pattern Matching Analysis. In *In satellite meeting on powder diffraction of the XV congress of the IUCr, vol 127*; 1990.

(50) Inaba, M.; Iriyama, Y.; Ogumi, Z.; Todzuka, Y.; Tasaka, A. Raman Study of Layered Rock-Salt LiCoO2 and Its Electrochemical Lithium Deintercalation. *J. Raman Spectrosc.* **1997**, *28*, 613–617.

(51) Hadjiev, V. G., Iliev, M.N., Vergilov, I. V. The Raman Spectra of Co3O4. *J. Phys. C Solid State Phys.* **1988**, *21* (7), L199. https://doi.org/10.1088/0022-3719/21/7/007.

(52) Cui, J.; Hope, G. A. Raman and Fluorescence Spectroscopy of CeO2, Er2O3, Nd2O3, Tm2O3, Yb2O3, La2O3, and Tb4O7. *J. Spectrosc.* **2015**, *2015*. https://doi.org/10.1155/2015/940172.

(53) Orlovskaya, N.; Steinmetz, D.; Yarmolenko, S.; Pai, D.; Sankar, J.; Goodenough, J. Detection of Temperature- and Stress-Induced Modifications of LaCoO3 by Micro-Raman Spectroscopy. *Phys. Rev. B - Condens. Matter Mater. Phys.* **2005**, *72* (1), 014122. https://doi.org/10.1103/PHYSREVB.72.014122/FIGURES/6/MEDIUM.

(54) Gummow, R. J.; Thackeray, M. M. STRUCTURE AND ELECTROCHEMISTRY OF

LITHIUM COBALT OXIDE SYNTHESISED AT 400°C. *Mat. Res. Bull* **1992**, *27*, 327–337.

(55) Wang, Y.; Cheng, T.; Yu, Z.-E.; Lyu, Y.; Guo, B. Study on the Effect of Ni and Mn Doping on the Structural Evolution of LiCoO2 under 4.6 V High-Voltage Cycling. *J. Alloys Compd.* **2020**, *842*, 155827. https://doi.org/https://doi.org/10.1016/j.jallcom.2020.155827.

(56) Hasan, M. M.; Dey, S.; Nafsin, N.; Mardinly, J.; Dholabhai, P. P.; Uberuaga, B. P.; Castro, R. H. R. Improving the Thermodynamic Stability of Aluminate Spinel Nanoparticles with Rare Earths. *Chem. Mater.* **2016**, *28* (14), 5163–5171. https://doi.org/10.1021/ACS.CHEMMATER.6B02577/ASSET/IMAGES/ACS.CHEMMATER.6B02577.SOCIAL.JPEG_V03.

(57) Li, H.; Dey, S.; Castro, R. H. R. Kinetics and Thermodynamics of Densification and Grain Growth: Insights from Lanthanum Doped Zirconia. *Acta Mater.* **2018**, *150*, 394–402. https://doi.org/10.1016/j.actamat.2018.03.033.

(58) Gin He Leong, V.; Sae Hong, S.; Castro, R. H. R. Improved Electrochemical Performance in Sc-Doped Nanocrystalline LiMn2O4. *Mater. Lett.* **2022**, 132824. https://doi.org/10.1016/J.MATLET.2022.132824.

(59) Takeuchi, S.; Tan, H.; Bharathi, K. K.; Stafford, G. R.; Shin, J.; Yasui, S.; Takeuchi, I.; Bendersky, L. A. Epitaxial LiCoO 2 Films as a Model System for Fundamental Electrochemical Studies of Positive Electrodes. **2015**. https://doi.org/10.1021/am508512q.

(60) Bates, J. B.; Dudney, N. J.; Neudecker, B. J.; Hart, F. X.; Jun, H. P.; Hackney, S. A. Preferred Orientation of Polycrystalline LiCoO 2 Films. *J. Electrochem. Soc.* **2000**, *147* (1), 59–70.

(61) Xia, H.; Lu, L. Texture Effect on the Electrochemical Properties of LiCoO2 Thin Films Prepared by PLD. *Electrochim. Acta* **2007**, *52* (24), 7014–7021.

https://doi.org/10.1016/J.ELECTACTA.2007.05.019.

(62) Jiang, Y.; Yan, P.; Yu, M.; Li, J.; Jiao, H.; Zhou, B.; Sui, M. Atomistic Mechanism of Cracking Degradation at Twin Boundary of LiCoO2. *Nano Energy* **2020**, *78*. https://doi.org/10.1016/J.NANOEN.2020.105364.

(63) Nagpure, S. C.; Babu, S. S.; Bhushan, B.; Kumar, A.; Mishra, R.; Windl, W.; Kovarik, L.; Mills, M. Local Electronic Structure of LiFePO4 Nanoparticles in Aged Li-Ion Batteries. *Acta Mater.* **2011**, *59* (18), 6917–6926. https://doi.org/10.1016/J.ACTAMAT.2011.07.043.

(64) Pender, J. P.; Jha, G.; Hyun Youn, D.; Ziegler, J. M.; Andoni, I.; Choi, E. J.; Heller, A.; Dunn, B. S.; Weiss, P. S.; Penner, R. M.; Buddie Mullins, C. Electrode Degradation in Lithium-Ion Batteries. *ACS Nano* **2020**, *14*, 59. https://doi.org/10.1021/acsnano.9b04365.

(65) Dholabhai, P. P.; Aguiar, J. A.; Wu, L.; Holesinger, T. G.; Aoki, T.; Castro, R. H. R.; Uberuaga, B. P. Structure and Segregation of Dopant-Defect Complexes at Grain Boundaries in Nanocrystalline Doped Ceria. *Phys. Chem. Chem. Phys* **2015**, *17*, 15375. https://doi.org/10.1039/c5cp02200b.

Appendix A

Atomistic Simulation

A few unique cases from the simulations with aliovalent dopants arose during the dopant replacements. **Figure A1a** illustrates the effect of Mg^{2+} doping at different positions on the relative energy of the simulation cell for the {001} surface. During the doping study of the original structure size, it was observed that aliovalent dopants prefer to remain in the bulk structure; however, a stable or constant energy profile in the bulk region in between the surfaces was never established in this cell (in contrast to the profiles shown in **Figure 2.2** and **2.3**). To resolve this issue, the structure was expanded in the z direction (the surface normal direction) and in the x/y directions (the in-plane directions of the surface). The expanded z direction structures followed the same trend and never achieved a constant bulk energy, but the expanded structure in the x/y directions corrected the issue and achieved a similar segregation profile to the isovalent dopants. The hypothesis for this behavior is that the aliovalent dopants perturb the electroneutrality of the cell and in this surface structure the dopants cause strong interactions across the periodic boundary conditions in the x and y directions, leading to significant self-interaction, though why this becomes stronger as the z dimension of the structure is increased is not clear. Further studies using a charge transfer potential could be useful for studying the effect of aliovalent dopants as the cobalt will likely help accommodate the change in electroneutrality.

Figure A1b shows aliovalent doping behavior of the Σ5 grain boundary and the impact of dopant position on the simulation cell energy. Due to some slight reconstructions at the interface, a dipole forms, causing an electric field to form across the cell that results in a small negative slope for the bulk behavior of the tetravalent dopants and a positive slope for the divalent dopants. To account for the slope, we first fit a line to the energies of the dopants in the

bulk. We then used the value of this fit at the GB center as the bulk reference and measured the segregation energy of the lowest energy site relative to this value, as illustrated in **Figure A1b**. Although these effects from aliovalent dopants could have impacts on the absolute value of the segregation energies, the relative trends relating to ionic size and charge should remain consistent. The other interesting result of the Σ5 boundary doping for all oxidation states is the disorder that is seen at each grain boundary. When **Figure 2.3** and **Figure A1b** are compared, it can be seen that there are only a few stable sites near the boundary for the dopants in the Σ3 system while the Σ5 system shows several more local minimum positions for the dopants. This again confirms the higher structural disorder at the Σ5 interface and why the relative magnitudes of the dopant segregation energy increase with the higher index grain boundaries.

(a)

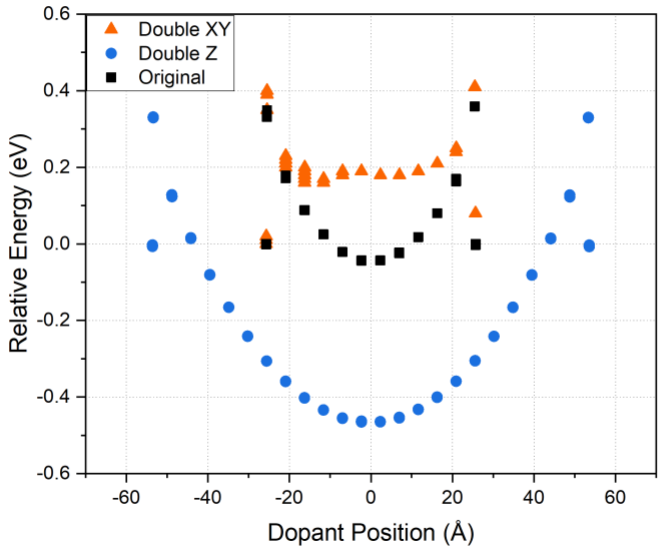

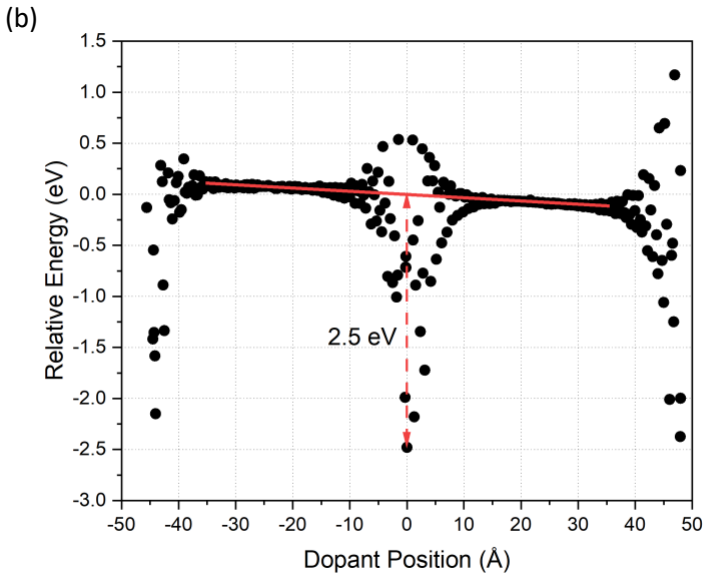

Figure A1. (a) Segregation profile of Mg^{2+} doping of {001} surface at the original structure size, structure doubled in the z direction, and structure doubled in both the x and y direction. In this plot, the surface site is located at a value of 0 eV instead of the bulk values for visualization of the data. The segregation energy can be determined from wherever the bulk energy stabilizes at the 0Å dopant position. (b) Segregation profile of Ti^{4+} doping of Σ5 grain boundary. The fitted red line shows the correction for the bulk energy value due to the dipole formation in the structure.

Table A1. Interatomic pair potential parameters for Al^{3+} and V^{5+} dopants.

Ionic Pair	A (eV)	ρ (Å)	C (eV*Å^6)
$Al^{3+} \cdots O^{2-}$ [1]	1474.4	0.3006	0
$V^{5+} \cdots O^{2-}$ [2]	2779.85	0.29185	0

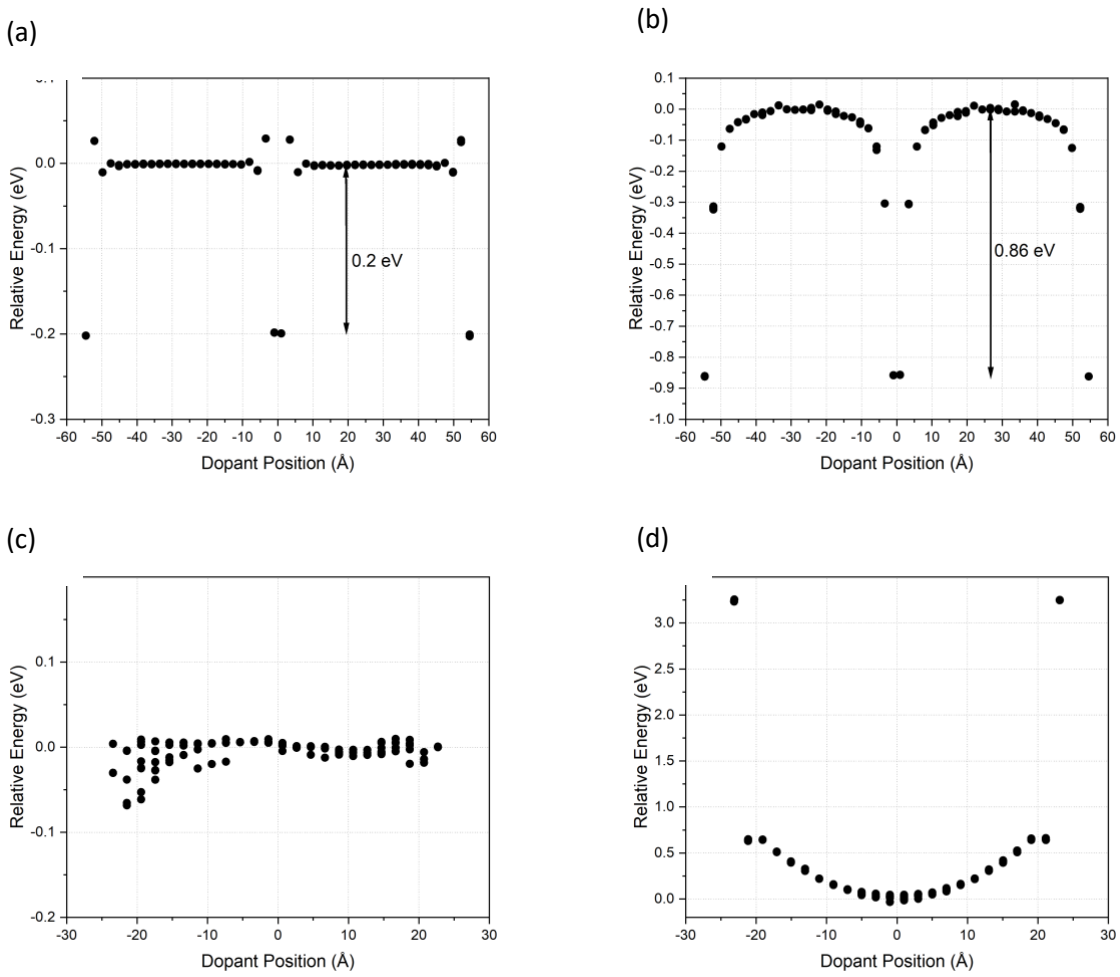

Figure A2. Segregation profile of (a) Al^{3+} to the Sigma 3 grain boundary, (b) V^{5+} to the Sigma 3 grain boundary, (c) Al^{3+} to the {104} surface, and (d) V^{5+} to the {104} surface.

References

(1) Sayle, D. C.; Sayle, T. X. T.; Parker, S. C.; Harding, J. H.; Catlow, C. R. A. The Stability of Defects in the Ceramic Interfaces, MgO MgO and CeO2 Al2O3. *Surf. Sci.* **1995**, *334* (1–3), 170–178. https://doi.org/10.1016/0039-6028(95)00396-7.

(2) Dietrich, A.; Catlow, C. R. A.; Maigret, B. Structural Modelling of Vanadium Pentoxide. *Mol. Simul.* **1993**, *11* (5), 251–265. https://doi.org/10.1080/08927029308022513.

Chapter 3: Improved Interfacial Stability of Doped $LiCoO_2$ Nanoparticles

Abstract

Nanoscale cathodes for lithium ion batteries continue to be limited in their application due to enhanced parasitic reactions, cycling induced coarsening, and capacity fading. Thermodynamic understanding of nanoparticle stability could help prevent critical failure mechanisms and improve the capacity retention in electrochemical cells. This study used calorimetric techniques to quantitatively study the interfacial energies, surface energy and grain boundary energy, of $LiCoO_2$ (LCO) nanoparticles. Dopant segregation was used to improve interfacial stability by synthesizing lanthanum doped LCO nanoparticles. The measurements show a surface energy decrease from 1.30 J/m^2 for the undoped LCO to a surface energy of 1.11 J/m^2 for the La-doped nanoparticles. A grain boundary energy of 0.29 J/m^2 was also experimentally measured for both nanoparticle chemistries. The undoped interfacial energies are consistent with the limited data previously reported and confirm the stabilization effect of La segregation. STEM-EELS revealed La segregation to the {104} and {001} surfaces and confirmed the strong segregation behavior of La. Coarsening data also confirmed that the La-doped nanoparticles maintained higher specific surface areas and smaller crystallite sizes than the undoped LCO. This surface stabilization through surface energy reduction could be useful in preventing degradation issues like cycling induced coarsening and intergranular cracking.

Introduction

Lithium ion technology is continuing to be used as a prominent energy storage technique and the technology is expanding into new applications. Despite the ample spectrum of applications, capacity, electrochemical performance, and charge/discharge rates are still

insufficient for the growing energy needs.[1] Nanostructured cathodes may provide enhancement in these areas due to the shorter diffusion path length and application in high charge/discharge rate applications.[2] However, as particle sizes are reduced below 100nm, the very same increased interfacial areas which are responsible for the improved performance[3–5] enhance parasitic reactions, facilitate cycle-induced intergranular cracking, accelerate cathode degradation due to the surface reactivity [6–9] and cycling induced coarsening.[10,11] The last degradation mechanism is critically connected to interfacial energies as the intrinsic driving force. Similar to the conventional Ostwald ripening process, the excess energies in high curvature particles cause dissolution and precipitation, resulting in growth, to reduce the total surface energy of the system.[12,13]

A number of studies have proposed the design of spontaneous dopant segregation to interfaces to reduce the driving force for coarsening, extending the lifetime of nanostructured materials.[14,15] This is related to the Gibbs adsorption isotherm describing the reduction of surface energies as a function of excess dopant at the interfaces.[16] Kirchheim showed that the interfacial energy will continue to decrease with increasing dopant excess at the interface until a second phase precipitates.[17] Following this principle, Nakajima et al. demonstrated scandium doped $LiMn_2O_4$ (LMO) nanoparticles show significantly reduced surface energy compared to the undoped LMO as a result of the dopant enrichment on both surfaces and grain boundaries.[18] The nanostructured LMO cathode showed greater resistance to grain growth during sintering and consistently maintained smaller crystallite size. Leong et al. later showed that this interfacial engineering led to improved cyclability when tested in a Li half-cell.[19] In another work, Wang et al. demonstrated that Mg doped cathodes for sodium batteries show Mg segregation, which

improves mechanical strength, reduces intergranular cracking, hence benefiting battery cyclability.[20]

In this work, we explore the possibility of extending the stability of $LiCoO_2$ (LCO) nanoparticles through interfacial doping. LCO was one of the original commercial cathode materials in Li-ion batteries but despite the extensive literature on both micro and nanoscale LCO, the thermodynamics of doped systems is still poorly understood. Maram et al. reported experimental average surface energies of 1.25 J/m^2 for LCO, representing a significant energetic driving force for coarsening for the high specific surface area nanoparticles.[21] The experimentally measured value is consistent with atomistic simulations measuring surface energies of {001}, {104}, and {110} planes, which are the most commonly found in LCO nanoparticles.[22,23] The possibility of reducing the surface energy of LCO was explored by atomistic simulations in the previous chapter.[24] Ionic segregation is a function of both ionic radius and valence state of the dopant, but no direct experimental data have correlated a reduction in surface energy as a function of dopant segregation in LCO. In this work, La-doped and undoped LCO nanoparticles were synthesized using a hydrothermal synthesis and La segregation was confirmed through STEM-EELS, consistently with the previously reported atomistic simulations. The utilization of calorimetric studies proved La segregation in LCO causes reduction of surface energy. The surface energy reduction leads to less coarsening during sintering and synthesis of the nanoparticles, demonstrating the potential of this methodology for stabilizing nanostructures in Li-ion battery applications.

Experimental Section

Synthesis

The synthesis method was adapted from Okubo et al. to synthesize lanthanum doped and undoped LCO nanoparticles.[7] The precursor solution of 20 mmol of $Co(NO_3)_2 \cdot 6H_2O$ (Sigma-Aldrich, ≥98%) in 100 mL of deionized (DI) water was slowly added to 100 mL of 5 M NaOH solution for the coprecipitation method. The doped nanoparticles were synthesized by reducing the amount of cobalt precursor and adding 0.5, 1.0, or 2.0 mole percent of lanthanum to the precursor solution as $La(NO_3)_3.6H_2O$ (Alfa Aesar, 99.9%). The coprecipitation yielded pink $Co(OH)_2$ nanoparticles that were then diluted into 1800 mL of DI Water. The suspension was oxidized to the brown colored CoOOH nanoparticles by bubbling air through the suspension for 48 hours. The suspension was centrifuged and washed with DI Water five times and then dried in an 80°C oven overnight. The dried pellet was ground with a mortar and pestle and 500 mg of CoOOH powder was added into 133 mL of 1 M LiOH (Sigma-Aldrich, 99.95%) aqueous solution. The suspension was stirred and added into a 200 mL stainless steel autoclave with a PTFE liner (4748A, Parr Instrument Company). The autoclave was then placed into the furnace at 100°C, heated at 0.5°C/min to 180°C, held for 12 hours at 180°C, then cooled at 1°C/min to 100°C, and removed to cool to room temperature. This hydrothermal process results in a dissolution of the CoOOH nanoparticles and then a crystallization of the LCO phase. The suspension of LCO nanoparticles was then centrifuged and washed four times and dried at 80°C overnight. The dried pellet was ground in a mortar and pestle again and then calcined at 300°C for 3 hours in air to ensure full oxidation of the LCO phase.

Characterization

Crystallographic phase of the nanoparticles was confirmed with a Bruker AXS D8 Advance powder diffractometer (CuKα radiation, λ=1.5406 Å) at a voltage of 40 kV and an emission current of 40 mA. Jade MDI software was used to confirm crystal phase and estimate crystallite size using the Scherrer equation with whole pattern fitting. The surface area of the nanoparticles was measured through the Brunauer Emmett Teller (BET) method with nitrogen adsorption using a Gemini VII (Micromeritics Instrument Corporation). Inductively coupled plasma mass spectrometry (ICP-MS, Agilent-7900) was performed to measure the Li, Co, and La concentrations in the nanoparticles. The instrument was equipped with a quartz spray chamber, a microMist concentric gas nebulizer, and nickel sampler and skimmer cones. The instrument was operated using 1.0 L/min of argon (Ar) carrier gas in helium (He) mode with the He flow maintained at 4.5 mL/min to reduce polyatomic interferences.

Scanning Electron Microscopy (SEM) was used to determine the grain size and morphology of the sintered pellets on a FEI 430 Nano-SEM Instrument (FEI Company). Scanning Transmission Electron Microscopy (STEM) coupled with Electron Energy Loss Spectroscopy (EELS) revealed the morphology of the nanoparticles and mapped dopant distribution. JEOL Grand ARM 300CF equipped with Gatan GIF Quantum with K2-summit was used for the study, operating at 300keV.

Surface Energy and Grain Boundary Energy Measurements

Measurement of surface and grain boundary energies was performed based on ‘sintering’ experiments carried out using a Differential Scanning Calorimeter (DSC) on a Netzsch DSC 404 F1 Pegasus (Netzsch Instruments). The design of the sintering experiments determined the enthalpy change (heat of sintering) associated with the morphological development and

densification of the nanoparticles. The theory of relating the heat of sintering and microstructural evolution directly to the interfacial energies of the particles has been extensively studied in the literature in other oxide systems.[25–27] The exothermic energy release during sintering can be related to the surface and grain boundary energies through **Equation 1**:

$$\Delta H_{sintering} = \Delta A_s \gamma_s + \Delta A_{GB} \gamma_{GB} \quad (1)$$

where $\Delta H_{sintering}$ is the heat of sintering, ΔA_s is the change in surface area during sintering, ΔA_{GB} is the change in grain boundary area during sintering, and γ_s and γ_{GB} are the surface enthalpy and grain boundary enthalpy, respectively. The heat of sintering term captures all exothermic processes associated with sintering (e.g. grain growth and densification) and the energy released during sintering is measured by the DSC during the heating profile. The change in surface area term is determined by the BET measurement before and after sintering. The change in grain boundary area is determined from the initial and final crystallite size, which are determined from XRD patterns and TEM images, and by subtracting the measured BET surface area. The grain boundary area is also determined from the morphology of the particles, as the calculated grain boundary area is dependent on the shape of the particles and can be accounted for through the appropriate shape factor.[28] This leaves only two unknowns, γ_s and γ_{GB}, in the equation which can be solved by running at least two different sintering experiments to solve the system of equations for the two values.

In truth, γ_s and γ_{GB} are the enthalpies and to calculate the surface and grain boundary energies the entropic contributions would need to be quantified. These specific DSC measurements will only measure enthalpic effects of sintering by directly measuring the heat flow during sintering and integrating the area under the curve. Wang et al. performed

calorimetric measurements of cobalt oxide (CoO) nanoparticles and bulk material to find the excess entropy associated with nanoparticle surfaces.[29] They compared 7 nm nanoparticles to 60 μm bulk particles and found an excess surface entropy to be on the order of 1.5 $JK^{-1}mol^{-1}$. In general, the surface entropy of oxides tends to be low.[30] Therefore, the surface entropy can be considered negligible at the low sintering temperatures used in these measurements (<700°C) and the surface enthalpy can be equated to the surface energy.[31]

The LCO powders were calcined at different temperatures to provide different initial states for the sintering measurements. The measurements were performed on ¼" diameter pellets pressed at 100 bar that were then equilibrated at 25°C and 50% relative humidity for 48 hours. The pellets were quickly transferred to the DSC after equilibration to ensure the same starting state for each sample at the beginning of the heating profile. Each sample was run under oxygen gas at 50 mL/min and the runs began with a 20 minute degassing period at 300°C. Then the samples were ramped from 150°C to the maximum sintering temperature and isothermally held for 20 minutes to ensure all grain growth and sintering was complete. This heating profile was repeated two more times to establish a baseline for the measurement and subtract any heat capacity effects from the heat of sintering peak. Then the peak was integrated to give the $\Delta H_{sintering}$ value. All experiments were carried out at a heating and cooling rate of 20 K/min.

One of the critical steps of this calorimetric measurement is to avoid the existence of parallel reactions other than sintering (coarsening) itself. That is, if other phenomena, such as redox reactions, desorption, decompositions, or phase transformations are happening concomitantly, the heat is a complex summation of all the processes and is extremely difficult to deconvolute. While the initial degassing at 300C is designed to minimize the impact of adsorbed species, the maximum temperature for the heating profile was determined from DSC/TGA

measurements on a Setsys Evolution (Setaram Inc.) to confirm sample stability throughout the experiment. This prevented other heat effects from Co redox reactions or lithium evaporation. For the LCO pellets, all pellets were sintered to 700°C and the powders before being pressed into pellets were calcined at 300°C, 350°C, 375°C, and 400°C for 1 hour to provide different starting grain sizes for the samples, which in turn yields different heats of sintering. The La doped samples were calcined at 300°C, 325°C, 350°C, and 400°C for 1 hour, and the 325°C pellet was sintered to 650°C while all the other samples were sintered to 700°C.

The TGA experiments revealed there was residual water on the surface of the nanoparticles beyond the degassing temperature. Therefore, the heat effect of water desorption needed to be quantified to account for the endothermic gas desorption. A 3Flex surface analyzer (Micromeritics Instrument Corporation) was used to preform water adsorption experiments connected to a Sensys Evolution DSC (Setaram Inc.) to capture the heat of adsorption of water molecules onto the surface. This complex method has been described in detail in past publications, so only parameters specific to this measurement will be outlined here.[32–35] This method can also be used to calculate surface energies, but this work will only discuss the impact of water desorption on the quantitative measurement for the heat of sintering. The particles are first degassed at 300°C for 12 hours under vacuum to achieve a completely anhydrous surface. After degassing, the nanoparticles are isothermally held at 25°C and the 3Flex is used to dose 2 μmol of water vapor per dose. The DSC measures the exothermic heats of adsorption for each water dose and the 3Flex measures the quantity of water adsorbed to the surface. The integrations of the DSC peaks give the collective heat of water desorption during sintering.

Results and Discussion

Synthesis

The undoped and 1 mol% lanthanum doped nanoparticles were synthesized with the hydrothermal synthesis method and calcined at different temperatures. **Figure 3.1** shows the XRD patterns of the nanoparticles calcined at 300°C and sintered at 700°C. The diffraction patterns confirm the nanoscale nature of our particles evidenced by peak broadening.[36,37] The patterns also verify there are no lanthanum rich secondary phases formed in the studied temperature range and the LCO crystallographic structure is maintained. Small amounts of Co_3O_4 exist as second phase being present in both the doped and undoped samples in similar amounts as the ICP supports. **Table 3.1** gives the stoichiometric ratios of Li/Co and La/Co from ICP-MS. The ICP data confirms the samples are slightly lithium deficient, which supports the formation of the Co_3O_4 phase.[22] However, doped and undoped samples have nearly identical Li/Co ratios. The La/Co ratio is nearly ~1 mol percent lanthanum, consistent with the nominal concentration, supporting coprecipitation synthesis as an effective method for synthesizing doped LCO.

The TEM images in **Figure 3.2** show the doped and undoped nanoparticles after calcining at 300°C. The images reveal a platelike morphology with thin particles that range from 7-20 nm in thickness, similarly to those reported by Okubo et al.[7] The nanoplatelets tend to stack along the {003} planes and the width and length had more variation in dimension than the thicknesses. Images for a variety of annealing conditions were collected and analyzed in terms of particles' dimensions as listed in **Table 3.2**. There was a size dependence on the calcination temperature and the doped nanoparticles consistently had smaller crystallite sizes than the

undoped. The BET surface area measurements also corroborate this result as the doped particle surface areas were higher than the undoped particles (**Table 3.2**).

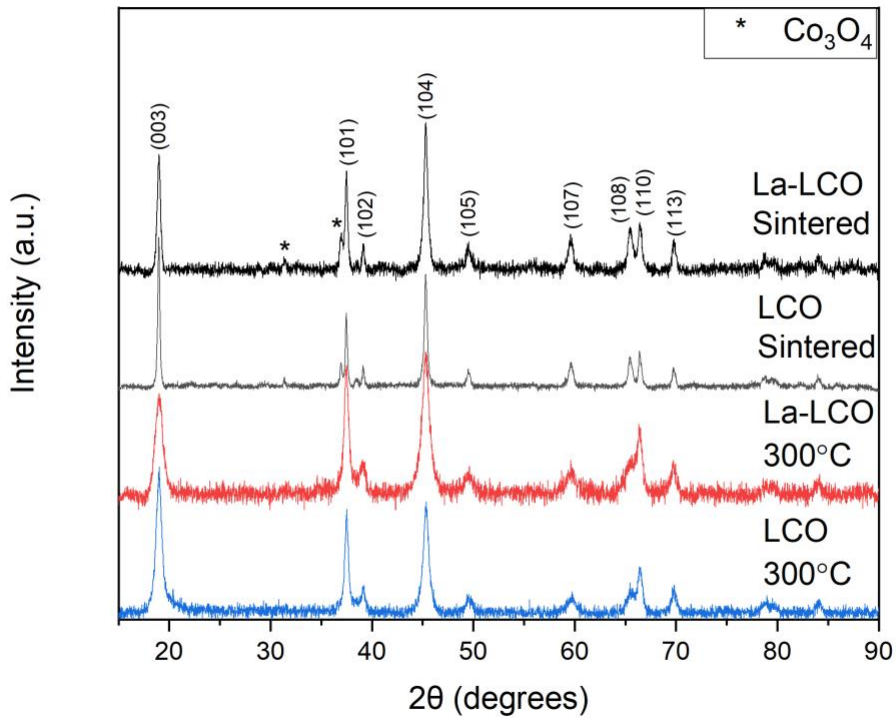

Figure 3.1. XRD patterns of the undoped and La doped LCO nanoparticles calcined at 300°C for 3 hours and after sintering at 700°C. The Co_3O_4 peaks are indicated by the * symbol.

Table 3.1. ICP-MS stoichiometric ratios of LCO nanoparticles and 1% La-LCO.

Sample	Li/Co	La/Co
LCO	0.92	–
1% La-LCO	0.91	0.011

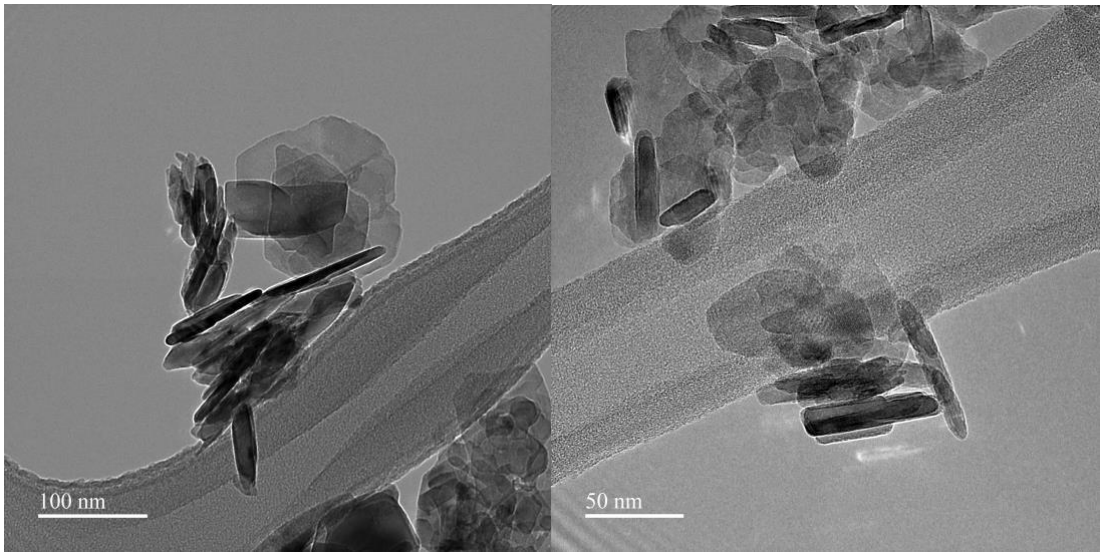

Figure 3.2. HR-TEM images of (a) LCO nanoparticles and (b) La-LCO nanoparticles calcined at 300°C for 3 hours.

Table 3.2. The measured values for undoped LCO and La-doped LCO showing the calcination/sintering temperatures, initial and final diameter, initial and final BET surface area (SA), initial and final grain boundary area (GBA), heats of water desorption, heats of sintering adjusted for the water desorption, and the surface energy and grain boundary energy.

Sample	Calcination/Sintering Temperature	Initial Diameter (nm)	Final Diameter (nm)	Initial SA (m^2/g)	Final SA (m^2/g)	Initial GBA (m^2/g)	Final GBA (m^2/g)	Water Desorption ΔH_{water} (J/g)	Adjusted $\Delta H_{sintering}$ (J/g)	γ_S (J/m^2)	γ_{GB} (J/m^2)
Undoped	300°C - 3hrs/700°C	27.5 ± 0.3	77.1 ± 1.2	53.1 ± 0.2	13.7 ± 0.1	14.6 ± 0.1	2.3 ± 0.1	32.8 ± 0.2	54.9 ± 0.9	1.3	0.29
Undoped	350°C - 1hr/700°C	32.7 ± 0.3	73.7 ± 1.1	40.9 ± 0.1	13.9 ± 0.1	14.1 ± 0.1	2.6 ± 0.1	18.7 ± 0.1	37.8 ± 0.6		
Undoped	375°C - 1hr/700°C	36.1 ± 0.3	66.2 ± 1.0	37.5 ± 0.2	13.5 ± 0.1	12.6 ± 0.1	3.9 ± 0.1	15.0 ± 0.1	32.6 ± 0.5		
Undoped	400°C - 1hr/700°C	39.2 ± 0.4	76.9 ± 1.2	34.0 ± 0.2	13.2 ± 0.1	11.9 ± 0.1	2.5 ± 0.1	11.1 ± 0.1	31.3 ± 0.5		
La-Doped	300°C - 3hrs/700°C	20.6 ± 0.2	56.8 ± 0.9	73.9 ± 0.3	22.2 ± 0.2	18.0 ± 0.2	2.3 ± 0.1	64.5 ± 0.3	75.1 ± 1.2	1.11	0.29
La-Doped	325°C - 1hr/650°C	22 ± 0.2	43.6 ± 0.7	65.2 ± 0.2	26.2 ± 0.1	18.8 ± 0.2	2.6 ± 0.1	53.1 ± 0.3	59.7 ± 1.0		
La-Doped	350°C - 1hr/700°C	24.1 ± 0.2	51.7 ± 0.8	57.5 ± 0.1	20.0 ± 0.1	18.2 ± 0.2	3.9 ± 0.1	44.6 ± 0.2	54.6 ± 0.9		
La-Doped	400°C - 1hr/700°C	26.6 ± 0.2	50.1 ± 0.8	47.9 ± 0.1	20.3 ± 0.1	18.6 ± 0.2	2.5 ± 0.1	35.9 ± 0.2	44.1 ± 0.7		

Thermodynamics of Interfaces

The reduced particle size is an indication of coarsening inhibition caused by lanthanum. LCO is expected to grow by Ostwald Ripening, having the surface energy as the key driving

force. To study the effect of lanthanum on the surface thermodynamics and discuss the implications in coarsening, the heat of sintering of the nanoparticles was analyzed using a DSC. **Figure 3.3a** shows the DSC measurements for the sintering of undoped nanoparticles pellets up to 700°C. The samples were previously annealed at different temperatures to induce distinct initial particle sizes in the DSC experiments. The sintering peaks give an exothermic heat signal due to the heat released during densification and grain growth. The onset of sintering shifts depending on the initial calcination temperature with the 300°C pellets starting sintering at the lowest temperature and 400°C at the highest temperature. The curves all have relatively noisy baselines at the low temperature range, but converge to similar baselines at the end of the sintering curve. The perceived noise is related to some gas evolution and differences in heat capacity as will be discussed later. By integrating the area under the curve, the heat of sintering was calculated and the particles calcined at 300°C exhibited the highest heat of sintering (**Table 3.2**). This is due to those particles having more interfacial area and the smallest particle size which leads to more microstructural evolution throughout sintering and more exothermic heat released. Four different initial states are chosen to provide different heats of sintering to allow a solvable linear system of equations based on **Equation 1** to converge to stable surface and grain boundary energy values.

Similarly, **Figure 3.3b** shows the DSC peaks for the 1% lanthanum doped LCO nanoparticles that take a similar shape to the undoped LCO. These pellets were also sintered to 700°C with the exception of the 325°C calcined sample that was sintered to 650°C in an effort to differentiate the initial and final states of sintering. In both samples there is no evidence of La rich secondary phase formation after sintering as shown in the XRD analysis (**Figure 3.1**). Again the samples with the smallest particle size and highest surface area have an earlier onset of

sintering due to the high interfacial area. Similarly, the sample sintered to 650°C has a lower intensity exothermic peak from the lower thermodynamic driving force compared to the 700°C pellets.

(a)

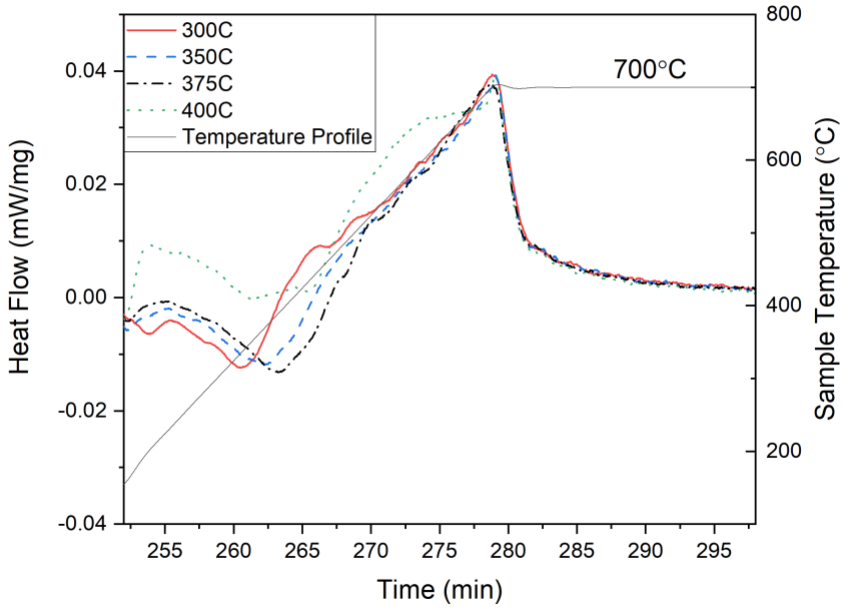

(b)

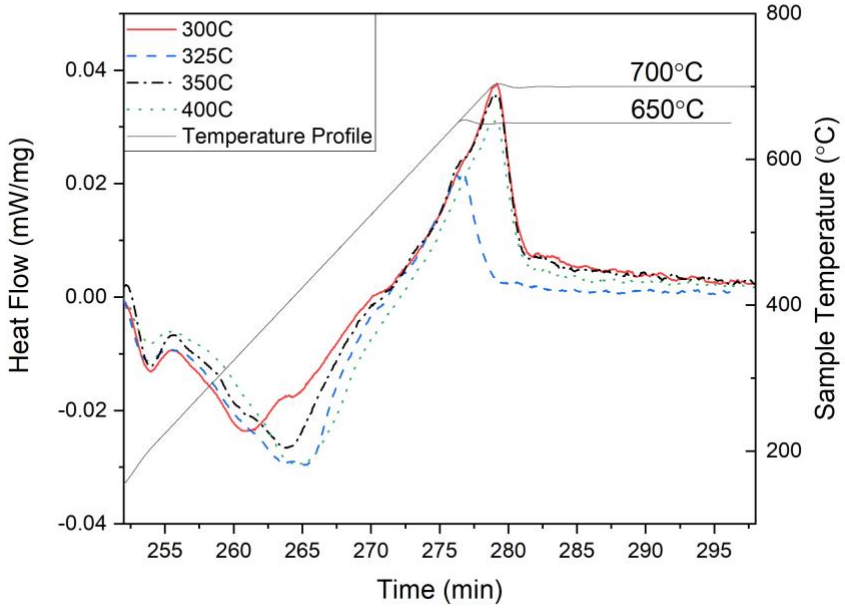

Figure 3.3. DSC sintering peaks measuring heat flow and sample temperature of (a) undoped LCO nanoparticles and (b) La-doped LCO nanoparticles.

The heat of sintering can be attributed to the evolution of microstructure according to **Equation 1** as long as there are no parallel heat effects taking place during the heating cycle, or that those phenomena are quantitatively accounted for as a 'heat correction'. There are a few factors that can cause endothermic effects that would impact the heat of sintering, including reduction of cobalt, lithium evaporation, phase transformations, heat capacity changes due to size evolution, and gas/vapor desorption. A DSC/TGA measurement tested for evaporating products, cobalt reduction, and any other heat effects that can impact the experiment. The results confirmed 700°C is a safe maximum temperature for the sintering experiments to avoid heat effects related to Co reduction and evaporation of Li. However, it became evident that endothermic effects appear to start at lower temperatures below 300°C. The XRD before and after sintering shows no precipitation of La rich secondary phases (**Figure 3.1**). Although it appears the Co_3O_4 phase could be precipitating during sintering, calcination experiments show that any unreacted CoOOH crystallizes into Co_3O_4 during the 300°C calcination. The Co_3O_4 particles are also extremely nanoscale in nature so the low intensity peaks are dwarfed by the LCO peak intensities and only the two highest intensity peaks present after sintering. These results leave heat capacity and water desorption as the most probable cause of the overlapping endothermic effects.

Heat capacity dependence on the particle size also impact the heat effects in the DSC studies.[38–40] As outlined in the experimental section, the heating profile ramping up to the maximum temperature profile is repeated three times in total. This is designed so that grain growth and sintering are completed in the first heating profile and no other heat effects occur

during the second and third heating profiles other than the heat capacity contributions. The DSC heat flow from the third curve is subtracted from the first heat flow that contains the heat of sintering to account for the heat capacity effect. However, the morphology, size, and microstructure of the pellets have changed by the second and third heating profile. If there is a heat capacity difference that arises from size dependence then we would see an artificial heat effect before the sintering peak. Although there is still debate on whether or not the size dependence of heat capacity is an artifact of improper degassing of samples, as some are attributed to hydration layers.[41–44] In order to correct for any heat capacity effects that may or may not be impacting the heat of sintering measurement, a Bezier background was drawn to ensure only sintering heat is included in the peak integration.

Even with degassing, the limited water desorption can still cause endothermic effects throughout the entirety of the sintering measurement. TGA results are shown in **Figure 3.4** of the doped and undoped samples going through a degassing period into the sintering heating profile. The nanoparticles were all held at 25°C and 50% RH for at least 48 hours to give them the same reference point and equilibration period. The powders were then ramped to 300°C for 20 minutes to degas and then ramped from 150°C to 700°C to simulate the sintering measurement. The results showed considerable mass loss (1.5-4.0%) during the degassing and then additional mass loss occurring during the sintering heat profile. The amount of water degassing from the surface is proportional to the surface area of the nanoparticles with the La-LCO calcined at 300°C having the highest surface area (smallest particle size) and the undoped LCO calcined at 400°C having the lowest surface area (largest particle size) (**Table 3.2**). From this data, the amount of water being degassed during the sintering measurement can be quantified by calculating the mass loss from the onset of sintering temperature to the isotherm at 700°C.

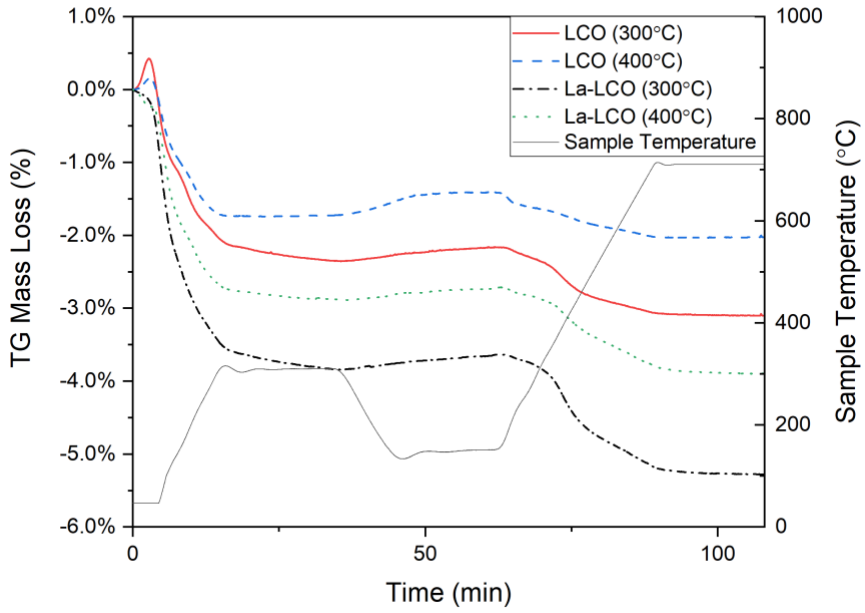

Figure 3.4. TGA results and sample temperature profile of the LCO and La-doped LCO nanoparticles calcined at 300°C and 400°C for 1 hour.

A water adsorption apparatus connected to a DSC was used to determine the heat associated with water desorption during sintering. This technique fully degasses the sample to the anhydrous state using heat and vacuum and then incrementally doses water onto the surface while the DSC measures the heat of adsorption. The water adsorption and desorption process is a reversible process, so the heat associated with water adsorption is equivalent to the desorption activation energy.[45,46] **Figure 3.5** shows the heats of adsorption plotted against the surface water coverage for the doped and undoped nanoparticles. The doped nanoparticles initially have higher heats of adsorption, but the curves invert at a coverage of about 5 H_2O/nm^2. Since the undoped nanoparticles' heats of adsorption remain higher with more surface water coverage, that is an indicator that the undoped particles have more higher energy surfaces than the doped nanoparticles. The coverage term can be calculated from the water adsorption apparatus that

measures the amount of water molecules adsorbed to the surface and the surface area. Similarly, the TGA and BET data can give the same data by finding the number of adsorbed water molecules from the mass loss and the specific surface area from BET. The coverage calculated is then used to get a cumulative heat effect from the heats of water adsorption. As expected, the particles with the most surface area and hydrated surface layers have the highest cumulative heats of desorption (**Table 3.2**).

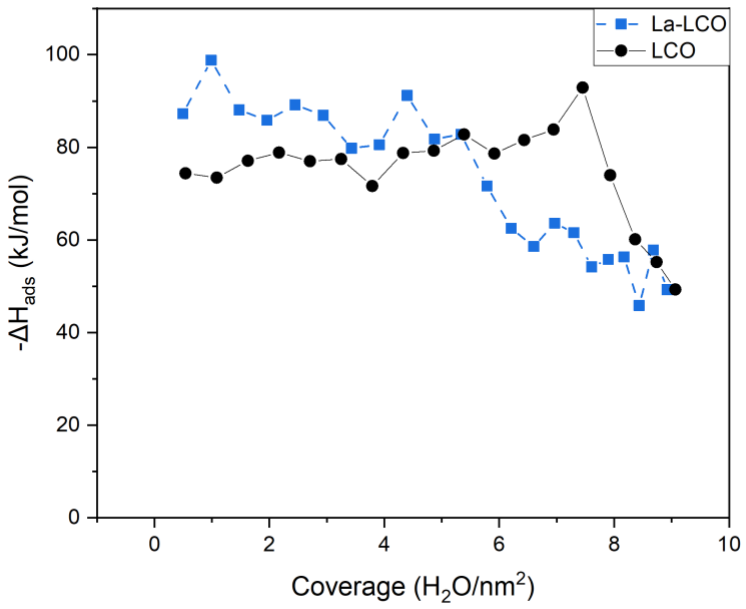

Figure 3.5. Heats of adsorption measured from DSC during the water adsorption experiment plotted against the surface water coverage for the undoped LCO and La-doped LCO nanoparticles calcined at 300°C for 3 hours.

Further required data for calculating surface and grain boundary energies is the final grain size and morphology after sintering. SEM images in **Figure 3.6** show the sintered nanoparticles after treatment at 700°C. The images show that the La-LCO maintains a smaller

crystallite size after sintering compared to the undoped LCO, which is supported by the BET results after sintering (**Table 3.2**). Initially the particles were more platelike in nature and from these images it appears the sintering has changed the morphology. The grain boundary area calculation requires an estimation of the shape factor to calculate the total grain boundary area before and after sintering.[28] To account for the morphology change, the shape factor after sintering was approximated as a tetrakaidecahedron at 3.55 because the particles are not completely spherical. The particles before sintering are platelike in shape as shown in the TEM image (**Figure 3.2**), so a shape factor of 5.7 was used for calculations.[47]

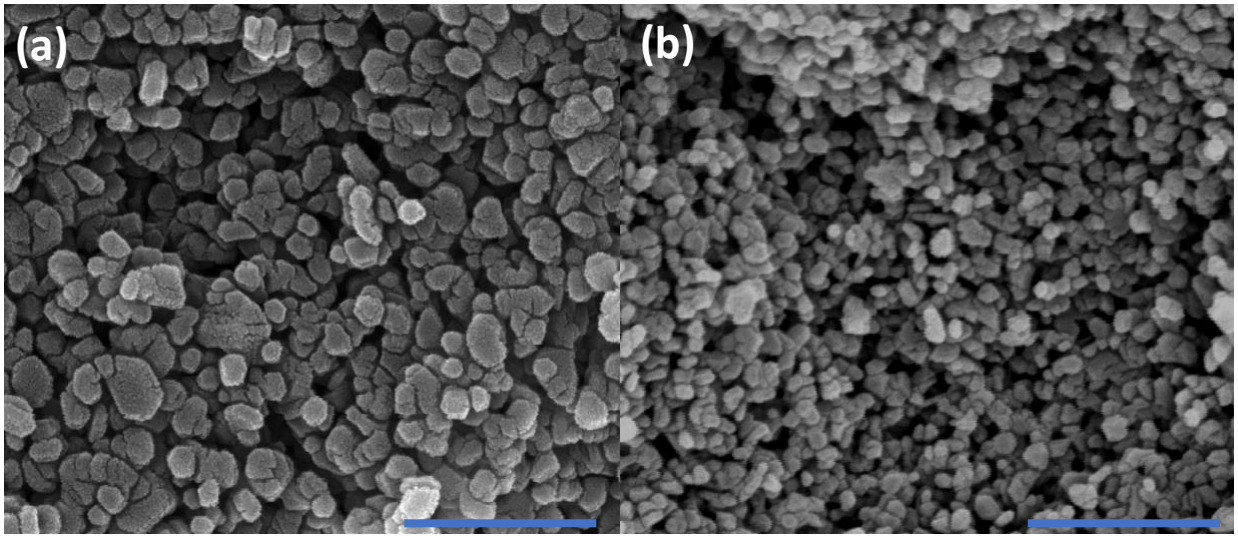

Figure 3.6. SEM images of (a) sintered LCO nanoparticles and (b) La-LCO nanoparticles. Scale bars indicate 500 nm.

With all this data, the interfacial energies of the materials can be calculated from **Equation 1** by solving the system of equations. The calculated surface and grain boundary energies for undoped LCO are 1.30 J/m^2 and 0.29 J/m^2, and 1.11 J/m^2 and 0.29 J/m^2 for the La-LCO, respectively. It is important to note these are average energies as each individual surface plane and grain boundary will have different energetic contributions. Maram et al. studied

surface energies for LCO measured by drop solution calorimetry and water adsorption.[21] They reported an anhydrous surface energy of 1.25 J/m^2, which is in excellent agreement with the undoped surface energy of 1.30 J/m^2 reported here. We are not aware of any other attempts to experimentally measure surface energies of LCO. The close agreement between two different calorimetric techniques reinforces the reliability of the sintering method and also indicates it is not a significant function of temperature, since drop solution calorimetry provides room temperature data and the sintering method assesses data in a range of temperatures.

Some of the most prevalent surfaces in LCO are the {001}, {104}, {110}, and {012}, with the {001} and {104} being the two with the lowest calculated surface energies.[23] Kramer and Ceder computationally studied LCO surfaces and calculated the {001} and {104} surface energies at 1.00 and 1.05 J/m^2, respectively.[22] However, the polar {001} surface is exceptionally sensitive to termination layer (Li, Co, or O), the degree of delithiation on the surface for a Li terminated surface, and the oxygen chemical potential. These factors could lead to {001} surfaces with varying surface energies and they also calculated higher surface energy surfaces like the {100} with a surface energy of 2.94 J/m^2. In general, the measured values in this paper are still in close agreement keeping in mind that they are average surface energies and there will of course be a fraction of higher energy surfaces.

Grain boundary energies are far less studied in the literature and especially rare to experimentally measure. Moriwake et al. studied a twin boundary computationally and experimentally by synthesizing and constructing a high symmetry twin grain boundary.[48] They found the experimentally observed structure and the most stable twin structure developed from first-principles calculations were very similar in nature and calculated a grain boundary energy of 0.3 J/m^2. This is also in excellent agreement with the experimentally measured value of 0.29

J/m^2 from this work. Although a twin boundary may be considered a simplistic grain boundary structural model, Fisher et al. have shown that it is a possible configuration in polycrystalline materials.[49] Additionally, it is possible that the tight repetitive stacking of the platelike nanoparticles leads to low index and highly stable grain boundaries, but that topic needs to be further explored in future work.

Overall, the interfacial energies experimentally determined in this work match the computational and experimental work done on surface energies previously. The novel experimental measurement of the average grain boundary energies that has not been previously reported are in the expected range and have good agreement with the limited computational work done. In addition, the lanthanum doped LCO nanoparticles have lower surface energies than the undoped particles. This reduction in surface energy helps maintain a smaller nanostructure, higher specific surface area, and more resistance to grain growth by limiting grain boundary mobility as shown in **Figure 3.7**. For all calcination temperatures studied, the La-doped samples consistently had lower crystallite sizes and higher surface areas. The addition of La helped lower the surface energy and reduce the thermodynamic driving force during sintering, as was previously reported in La-doped zirconia.[50] In addition, Hasan et al. explored several different dopants in $MgAl_2O_4$ to test the effect of ionic radius on resistance to grain growth.[51] Their results show that larger ionic radius dopants like La provide the greatest reduction in surface energy compared to smaller dopants like Y. This surface energy reduction provides more interfacial stability and maintains a smaller nanostructure in the ceramic materials, which in turn retains the unique nanoscale properties.

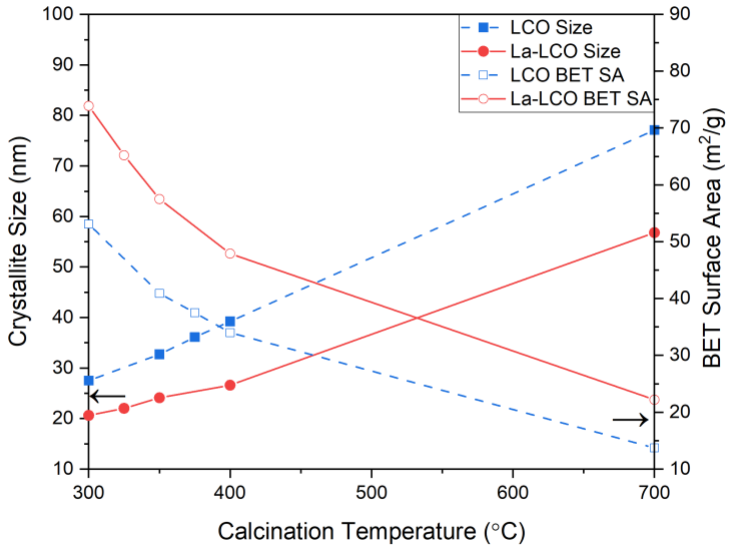

Figure 3.7. Crystallite size and BET surface area of undoped and La-doped LCO nanoparticles as a function of the calcination temperature.

Dopant Segregation to Surfaces

STEM-EELS was performed on the La-doped nanoparticles to confirm dopant segregation and the images are shown in **Figure 3.8a-c**. The EELS image shows a segregated green color near the surfaces of the nanoparticle representing lanthanum in **Figure 3.8b**. The center of the particles are more purple due to the overlapping Co (blue) and O (red) colors. The box scan plot depicted in the graph shows the ratio of La to Co intensity counts. There is a clear La intensity increase near the surface, confirming that La is enriched near the surface of the particles relative to the Co and O concentrations. It is worth noting again that the particles tend to be platelike in nature, so the fact that La is present in the center of the particles is expected. The platelets tend to lay on the {001} interfaces, so the La would segregate to both the top surface and bottom surface causing high La concentrations in the middle of the platelets due the electron transmission in TEM. Our previous studies confirmed this concept by imaging a nanoplatelet

looking axially down the Co layers and confirming segregation to the {001} surface.[24] **Figure 3.8c** shows a similar view of a platelike particle and the box scan results are shown in **Figure 3.9b**. The plot confirms the La segregation to both the {001} surfaces shown and a much lower La/Co ratio in the bulk of the particle. These images reveal that La has a strong segregation energy that thermodynamically drives the dopant to several types of interfaces.

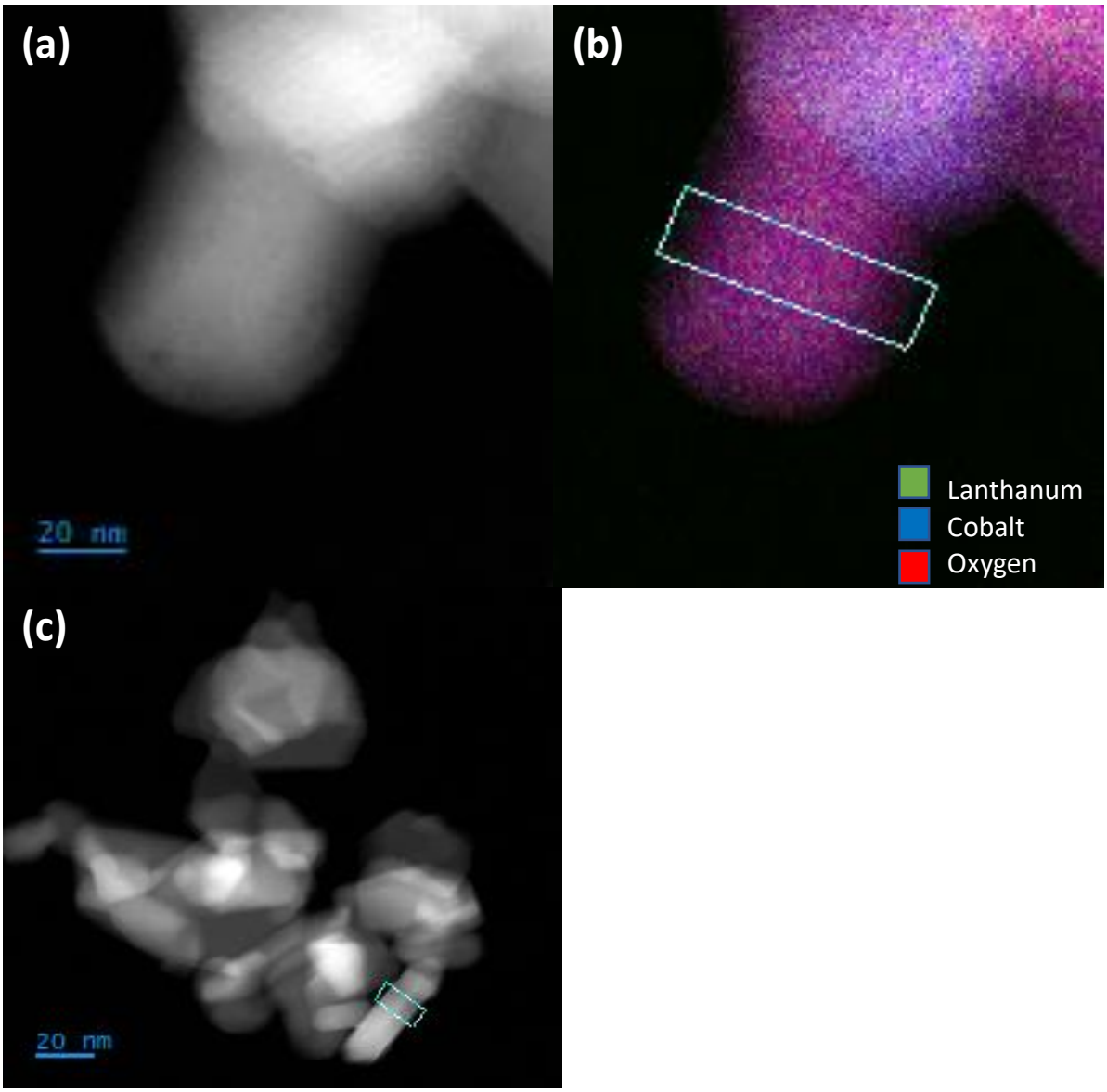

Figure 3.8. STEM-EELS images of 1% La-doped LCO nanoparticles calcined at 600°C. (a) and (c) depict the ADF images of the nanoparticles and (b) shows the EELS color mapping of (a)

(a)

with the La, Co, and O concentrations. Box scans from (b) are shown in **Figure 3.9a** and the scan from (c) is shown in **Figure 3.9b**.

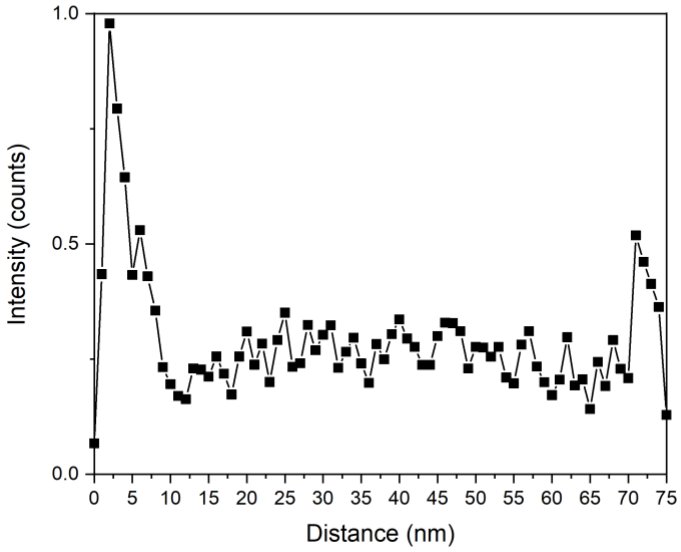

(b)

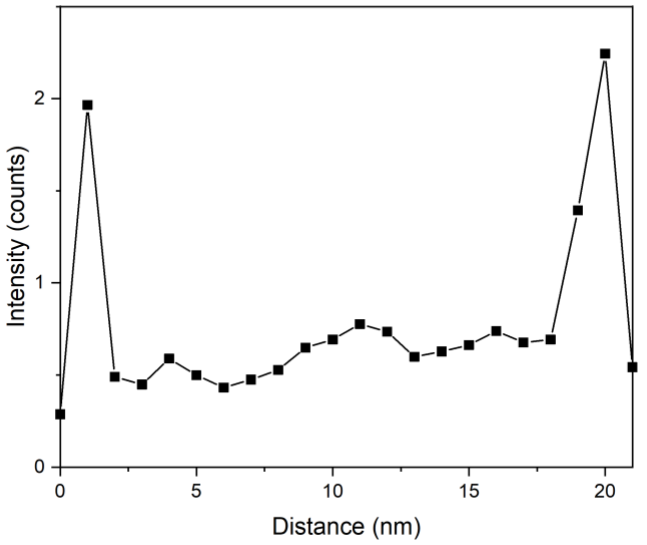

Figure 3.9. Box scan plots showing the La/Co ratio for the scans shown in **Figure 3.8**. (a) Box scan from **Figure 3.8b** and (b) box scan of **Figure 3.8c** showing the segregation to the {001} surface.

Effect of Dopant Content

Doping is an effective technique for stabilizing nanoparticles, but dopant chemistry and selection is a complex process for nanomaterials and depends on several factors. The enthalpy of segregation depends on the dopant and matrix size mismatch, oxidation state of the dopant, matrix solubility, and coordination number at the surface.[52,53] Chapter 2 explored dopant segregation in layered LCO nanoparticles and utilized atomistic simulations for dopant selection.[24] We found dopant segregation energy increased linearly with ionic size and increased further with aliovalent dopants at higher oxidation states. Specifically, lanthanum had one of the highest segregation energies of the dopants studied and it was experimentally confirmed that lanthanum segregates to grain boundaries and surfaces. From these experiments, lanthanum was chosen as the dopant for these sintering measurements, because of its strong thermodynamic driving force to interfaces. However, the fraction of dopant can be difficult to determine as interfacial sites can saturate from dopants with high segregation energies and precipitate secondary phases.[54] The precipitation of a secondary phase of $LaAlO_3$ in lanthanum doped $MgAl_2O_4$ spinel was confirmed due to the high segregation potential of the dopant.[55] Due to the high segregation energy of lanthanum, three samples of doped LCO were synthesized to study the sintering behavior and phase purity. **Figure 3.10** shows the DSC results from sintering pellets at the same conditions as the interfacial energy measurements. The 2% La-LCO sample has an endothermic heat effect before the onset of sintering and a slightly different curve shape compared to the 1% and 0.5% La-LCO samples. The two samples with lower doping

concentrations also have endothermic heat events before the sintering onset, but as was previously addressed this is due to the water desorption. The XRD patterns for all three samples calcined at 700°C were collected to look for common secondary phases of lanthanum and cobalt (**Figure 3.11**). The XRD patterns revealed the characteristic LCO diffraction patterns and the expected secondary phase of Co_3O_4 that results from the high fraction of cobalt near surfaces in the nanoparticles and slightly delithiated nanoparticles. The 2% La-LCO also has a few impurity peaks near a 2θ of 33 degrees that were attributed to $LaCoO_3$.[56,57] This a common phase transformation that occurs in lanthanum based solid state electrolytes when interfaced with cobalt containing active materials.[58] Therefore, the DSC and XRD data points to using a 1% La-doped LCO in order to maximize the interfacial thermodynamic stability during sintering, but avoid the precipitation of secondary phases.

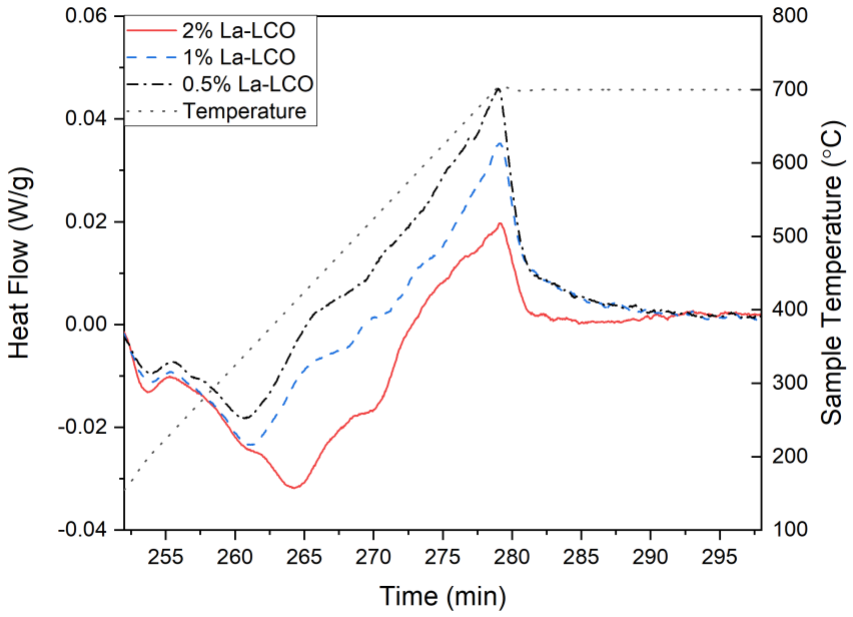

Figure 3.10. DSC sintering profiles of 0.5, 1.0, and 2.0 mole percent La-doped LCO up to 700°C.

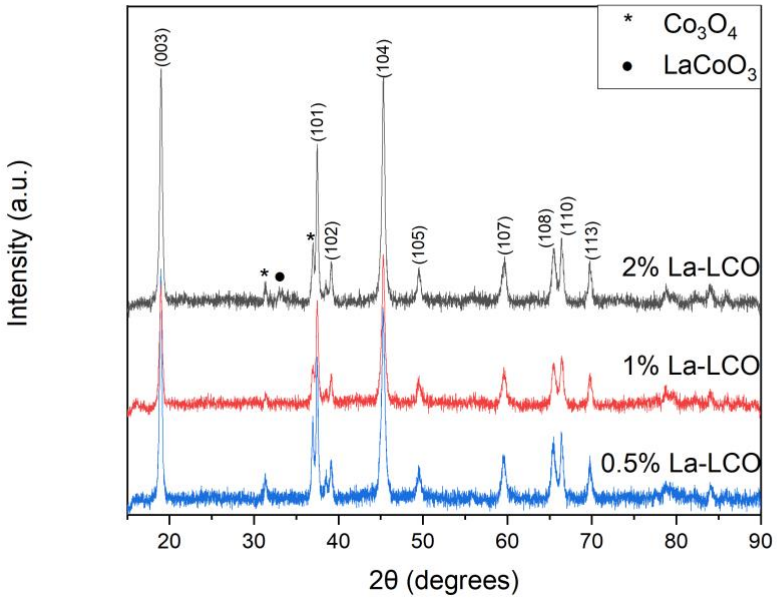

Figure 3.11. XRD patterns of 0.5, 1.0, and 2.0 mole percent La-doped LCO calcined at 700°C.

Data Implication and Limitations

The significance of these results show that the surface energy and morphology of the nanoparticles can be impacted and changed to give more favorable crystallographic structures. For example, the {001} surface is not an active surface for Li diffusion during intercalation/deintercalation, because Li ions prefer to move along Co layers and not across them.[59] Dopant segregation can be used to stabilize more {104} surfaces that are active surface planes for lithium diffusion and decrease the fraction of {001} surface planes. **Figure 3.1** does show higher intensity {104} XRD peaks compared to the {001} plane for the La-doped materials, but the {001} plane remains the highest intensity peak for the undoped LCO. This could be initial evidence that the morphology is changing in the doped LCO. However, the intensity of XRD peaks in nanoscale materials can be very sensitive to crystallite size and the TEM/SEM images don't show any drastic differences in morphology, so further investigation is

necessary to quantitatively compare surface planes. In addition, grain boundary networks can play a critical role in Li diffusion and the effect is amplified in nanostructures with even higher interfacial areas.[60,61] Careful and specific selection of segregating dopants that could enhance ionic and electronic conductivity at grain boundaries could drastically improve electrochemical performance of nanostructured cathodes. The thermodynamic understanding of cathode materials is critical for the progression of lithium ion batteries and further material development. Dopant segregation and interfacial engineering can play a critical role in designing stable battery materials with optimized morphologies for electrochemical performance.

Although these values all compared well to the literature values previously reported, the minimization method while solving for the energies is sensitive to subtle changes. Specifically, the initial crystallite size was difficult to measure with the platelike nature of the particles. The standard method is to use the Scherrer equation and Williamson-Hall plots to calculate crystallite size from XRD, but this becomes less accurate with anisotropic particles. TEM images were used to measure the thicknesses and widths of the particles to give an average crystallite size. The grain boundary area was calculated from the crystallite size and the assumed shape factors based on the observed particle morphology. The calculated interfacial energies are rather sensitive to the changes of the initial crystallite size and in turn the grain boundary area. The crystallite size measurements could be improved further to make the calculations more robust and improve accuracy.

Conclusion

The surface and grain boundary energies of undoped and 1 mole percent La-doped LCO were experimentally measured through the heats of sintering and water desorption. The La-doped LCO had lower surface energies compared to the undoped LCO nanoparticles due to the

La segregation to interfaces. This resulted in a resistance to grain growth and sintering in the doped samples and produced nanoparticles with smaller crystallite size and more specific surface area. A repeatable synthesis method for doped LCO nanoparticles was developed and La segregation was confirmed through STEM-EELS. The surface and grain boundary energy compared well with values from literature and confirmed the calorimetric technique is a useful method for cathode design in batteries. This could be especially valuable in designing optimal morphologies for lithium intercalation and improving electrochemical performance.

References

(1) Hausbrand, R.; Cherkashinin, G.; Ehrenberg, H.; Gröting, M.; Albe, K.; Hess, C.; Jaegermann, W. Fundamental Degradation Mechanisms of Layered Oxide Li-Ion Battery Cathode Materials: Methodology, Insights and Novel Approaches. *Mater. Sci. Eng. B* **2015**, *192* (C), 3–25. https://doi.org/10.1016/J.MSEB.2014.11.014.

(2) Bruce, P. G.; Scrosati, B.; Tarascon, J. M. Nanomaterials for Rechargeable Lithium Batteries. *Angew. Chemie - Int. Ed.* **2008**, *47* (16), 2930–2946. https://doi.org/10.1002/ANIE.200702505.

(3) Sotelo Martin, L. E.; Castro, R. H. R. Al Excess Extends Hall-Petch Relation in Nanocrystalline Zinc Aluminate. *J. Am. Ceram. Soc.* **2022**, *105* (2), 1417–1427. https://doi.org/10.1111/JACE.18176.

(4) Lu, L.; Shen, Y.; Chen, X.; Qian, L.; Lu, K. Ultrahigh Strength and High Electrical Conductivity in Copper. *Science (80-.).* **2004**, *304* (5669), 422–426. https://doi.org/10.1126/SCIENCE.1092905/SUPPL_FILE/PAPV2.PDF.

(5) Hammer, B.; Nørskov, J. K. Theoretical Surface Science and Catalysis—Calculations and Concepts. *Adv. Catal.* **2000**, *45* (C), 71–129. https://doi.org/10.1016/S0360-

0564(02)45013-4.

(6) Pender, J. P.; Jha, G.; Hyun Youn, D.; Ziegler, J. M.; Andoni, I.; Choi, E. J.; Heller, A.; Dunn, B. S.; Weiss, P. S.; Penner, R. M.; Buddie Mullins, C. Electrode Degradation in Lithium-Ion Batteries. *ACS Nano* **2020**, *14*, 59. https://doi.org/10.1021/acsnano.9b04365.

(7) Okubo, M.; Hosono, E.; Kim, J.; Enomoto, M.; Kojima, N.; Kudo, T.; Zhou, H.; Honma, I. Nanosize Effect on High-Rate Li-Ion Intercalation in LiCoO2 Electrode. *J. Am. Chem. Soc.* **2007**, *129* (23), 7444–7452. https://doi.org/10.1021/ja0681927.

(8) Jo, M.; Hong, Y.-S.; Choo, J.; Cho, J. Effect of LiCoO2 Cathode Nanoparticle Size on High Rate Performance for Li-Ion Batteries. *J. Electrochem. Soc.* **2009**, *156* (6), A430. https://doi.org/10.1149/1.3111031/XML.

(9) Jiang, Y.; Yan, P.; Yu, M.; Li, J.; Jiao, H.; Zhou, B.; Sui, M. Atomistic Mechanism of Cracking Degradation at Twin Boundary of LiCoO2. *Nano Energy* **2020**, *78*. https://doi.org/10.1016/J.NANOEN.2020.105364.

(10) Nagpure, S. C.; Babu, S. S.; Bhushan, B.; Kumar, A.; Mishra, R.; Windl, W.; Kovarik, L.; Mills, M. Local Electronic Structure of LiFePO4 Nanoparticles in Aged Li-Ion Batteries. *Acta Mater.* **2011**, *59* (18), 6917–6926. https://doi.org/10.1016/J.ACTAMAT.2011.07.043.

(11) Navrotsky, A.; Ma, C.; Lilova, K.; Birkner, N. Nanophase Transition Metal Oxides Show Large Thermodynamically Driven Shifts in Oxidation-Reduction Equilibria. *Science (80-.).* **2010**, *330* (6001), 199–201. https://doi.org/10.1126/SCIENCE.1195875/SUPPL_FILE/NAVROTSKY-SOM.PDF.

(12) Castro, R. H. R.; Gouvêa, D. Sintering and Nanostability: The Thermodynamic Perspective. *J. Am. Ceram. Soc.* **2016**, *99* (4), 1105–1121.

https://doi.org/10.1111/JACE.14176.

(13) Fischmeister, H.; Grimvall, G. Ostwald Ripening — A Survey. *Sinter. Relat. Phenom.* **1973**, 119–149. https://doi.org/10.1007/978-1-4615-8999-0_9.

(14) Chang, C. H.; Gong, M.; Dey, S.; Liu, F.; Castro, R. H. R. Thermodynamic Stability of SnO2 Nanoparticles: The Role of Interface Energies and Dopants. *J. Phys. Chem. C* **2015**, *119* (11), 6389–6397. https://doi.org/10.1021/JP512969K/ASSET/IMAGES/JP512969K.SOCIAL.JPEG_V03.

(15) Hasan, M. M.; Dholabhai, P. P.; Castro, R. H. R.; Uberuaga, B. P. Stabilization of MgAl2O4 Spinel Surfaces via Doping. *Surf. Sci.* **2016**, *649*, 138–145. https://doi.org/10.1016/J.SUSC.2016.01.028.

(16) Bangham, D. H. THE GIBBS ADSORPTION EQUATION AND ADSORPTION ON SOLIDS. *Trans. Faraday Soc.* **1937**, *33*, 805–811.

(17) Kirchheim, R. Reducing Grain Boundary, Dislocation Line and Vacancy Formation Energies by Solute Segregation. I. Theoretical Background. *Acta Mater.* **2007**, *55* (15), 5129–5138. https://doi.org/10.1016/J.ACTAMAT.2007.05.047.

(18) Nakajima, K.; Souza, F. L.; Freitas, A. L. M.; Thron, A.; Castro, R. H. R. Improving Thermodynamic Stability of Nano-LiMn2O4for Li-Ion Battery Cathode. *Chem. Mater.* **2021**, *33* (11), 3915–3925. https://doi.org/10.1021/ACS.CHEMMATER.0C04305/SUPPL_FILE/CM0C04305_SI_001.PDF.

(19) Leong, V. G. H.; Hong, S. S.; Castro, R. H. R. Improved Electrochemical Performance in Sc-Doped Nanocrystalline LiMn2O4. *Mater. Lett.* **2022**, *325*, 132824. https://doi.org/10.1016/J.MATLET.2022.132824.

(20) Wang, K.; Wan, H.; Yan, P.; Chen, X.; Fu, J.; Liu, Z.; Deng, H.; Gao, F.; Sui, M. Dopant Segregation Boosting High-Voltage Cyclability of Layered Cathode for Sodium Ion Batteries. *Adv. Mater.* **2019**, *31* (46). https://doi.org/10.1002/ADMA.201904816.

(21) Maram, P. S.; Costa, G. C. C.; Navrotsky, A. Experimental Confirmation of Low Surface Energy in LiCoO 2 and Implications for Lithium Battery Electrodes . *Angew. Chemie* **2013**, *125* (46), 12361–12364. https://doi.org/10.1002/ANGE.201305375.

(22) Kramer, D.; Ceder, G. Tailoring the Morphology of LiCoO2: A First Principles Study. *Chem. Mater.* **2009**, *21* (16), 3799–3809. https://doi.org/10.1021/cm9008943.

(23) Qian, D.; Hinuma, Y.; Chen, H.; Du, L. S.; Carroll, K. J.; Ceder, G.; Grey, C. P.; Meng, Y. S. Electronic Spin Transition in Nanosize Stoichiometric Lithium Cobalt Oxide. *J. Am. Chem. Soc.* **2012**, *134* (14), 6096–6099. https://doi.org/10.1021/ja300868e.

(24) Dahl, S.; Aoki, T.; Banerjee, A.; Uberuaga, B. P.; Castro, R. H. R. Atomistic Simulation Informs Interface Engineering of Nanoscale LiCoO2. *Chem. Mater.* **2022**. https://doi.org/10.1021/ACS.CHEMMATER.2C01246.

(25) Kang, S. *Sintering: Densification, Grain Growth and Microstructure*; Elsevier, 2004.

(26) Hayun, S.; Ushakov, S. V.; Navrotsky, A. Direct Measurement of Surface Energy of CeO2 by Differential Scanning Calorimetry. *J. Am. Ceram. Soc.* **2011**, *94* (11), 3679–3682. https://doi.org/10.1111/J.1551-2916.2011.04843.X.

(27) Castro, R. H. R.; T^ Orres, R. B.; Pereira, G. J.; Gouv^, D. Interface Energy Measurement of MgO and ZnO: Understanding the Thermodynamic Stability of Nanoparticles. *Chem. Mater* **2010**, *22*, 2502–2509. https://doi.org/10.1021/cm903404u.

(28) MENDELSON, M. I. Average Grain Size in Polycrystalline Ceramics. *J. Am. Ceram. Soc.* **1969**, *52* (8), 443–446. https://doi.org/10.1111/J.1151-2916.1969.TB11975.X.

(29) Wang, L.; Vu, K.; Navrotsky, A.; Stevens, R.; Woodfield, B. F.; Boerio-Goates, J. Calorimetric Study: Surface Energetics and the Magnetic Transition in Nanocrystalline CoO. **2004**. https://doi.org/10.1021/cm049040i.

(30) Jura, G.; Garland1, C. W. The Experimental Determination of the Surface Tension of Magnesium Oxide.

(31) McCormack, S. J.; Navrotsky, A. Thermodynamics of High Entropy Oxides. *Acta Mater.* **2021**, *202*, 1–21. https://doi.org/10.1016/J.ACTAMAT.2020.10.043.

(32) Castro, R. H. R.; Quach, D. V; Rock, P. A. Analysis of Anhydrous and Hydrated Surface Energies of Gamma-Al 2 O 3 by Water Adsorption Microcalorimetry. **2012**. https://doi.org/10.1021/jp309319j.

(33) Drazin, J. W.; Castro, R. H. R. Water Adsorption Microcalorimetry Model: Deciphering Surface Energies and Water Chemical Potentials of Nanocrystalline Oxides. **2014**. https://doi.org/10.1021/jp5016356.

(34) Adamson, A. W. An Adsorption Model for Contact Angle and Spreading. *J. Colloid Interface Sci.* **1968**, *27* (2), 180–187. https://doi.org/10.1016/0021-9797(68)90025-8.

(35) Ushakov, S. V.; Navrotsky, A. Direct Measurements of Water Adsorption Enthalpy on Hafnia and Zirconia. *Appl. Phys. Lett.* **2005**, *87* (16), 164103. https://doi.org/10.1063/1.2108113.

(36) Pecharsky, V. K.; Zavalij, P. Y. *Fundamentals of Diffraction*; 2003.

(37) Patterson, A. L. The Scherrer Formula for X-Ray Particle Size Determination. *Phys. Rev.* **1939**, *56* (10), 978. https://doi.org/10.1103/PhysRev.56.978.

(38) Kousika, A.; D'Aguanno, B.; Thomas, T. Size- and Temperature-Dependent Specific Heat Capacity and Diffusion Constants of Ultra-Small BaTaO2N Nanoparticles. *Appl. Nanosci.*

2020, *10* (3), 767–773. https://doi.org/10.1007/S13204-019-01146-7/TABLES/1.

(39) Snow, C. L.; Lee, C. R.; Shi, Q.; Boerio-Goates, J.; Woodfield, B. F. Size-Dependence of the Heat Capacity and Thermodynamic Properties of Hematite (α-Fe2o3). *J. Chem. Thermodyn.* **2010**, *42* (9), 1142–1151. https://doi.org/10.1016/J.JCT.2010.04.009.

(40) Gu, M. X.; Sun, C. Q.; Chen, Z.; Yeung, T. C. A.; Li, S.; Tan, C. M.; Nosik, V. Size, Temperature, and Bond Nature Dependence of Elasticity and Its Derivatives on Extensibility, Debye Temperature, and Heat Capacity of Nanostructures. https://doi.org/10.1103/PhysRevB.75.125403.

(41) Saeedian, M.; Mahjour-Shafiei, M.; Shojaee, E.; Mohammadizadeh, M. R.; Karegar Ave, N. Specific Heat Capacity of TiO2 Nanoparticles. *J. Comput. Theor. Nanosci.* **2012**, *9*, 616–620.

(42) Wu, X. M.; Wang, L.; Tan, Z. C.; Li, G. H.; Qu, S. S. Preparation, Characterization, and Low-Temperature Heat Capacities of Nanocrystalline TiO2 Ultrafine Powder. *J. Solid State Chem.* **2001**, *156* (1), 220–224. https://doi.org/10.1006/JSSC.2000.8991.

(43) Navrotsky, A. Calorimetry of Nanoparticles, Surfaces, Interfaces, Thin Films, and Multilayers. *J. Chem. Thermodyn.* **2007**, *39* (1), 1–9. https://doi.org/10.1016/J.JCT.2006.09.011.

(44) Spencer, E. C.; Ross, N. L.; Parker, S. F.; Woodfield, B. F.; Boerio-Goates, J.; Smith, S. J.; Olsen, R. E.; Kolesnikov, A. I.; Navrotsky, A.; Ma, C. Determination of the Magnetic Contribution to the Heat Capacity of Cobalt Oxide Nanoparticles and the Thermodynamic Properties of the Hydration Layers. *iopscience.iop.org* **2011**. https://doi.org/10.1088/0953-8984/23/20/205303.

(45) Schlangen, L. J. M.; Koopal, L. K.; Cohen Stuart, M. A.; Lyklema, J. Wettability:

Thermodynamic Relationships between Vapour Adsorption and Wetting. *Colloids Surfaces A Physicochem. Eng. Asp.* **1994**, *89* (2–3), 157–167. https://doi.org/10.1016/0927-7757(94)80115-0.

(46) Chafik, T.; Zaitan, H.; Harti, S.; Darir, A.; Achak, O. Determination of the Heat of Adsorption and Desorption of a Volatile Organic Compound Under Dynamic Conditions Using Fourier-Transform Infrared Spectroscopy. *Spectrosc. Lett.* **2007**, *40*, 763–775. https://doi.org/10.1080/00387010701429666.

(47) Hooshmand, P.; Bahrami, M.; Bagheri, N.; Jamshidian, M.; Malekshah, E. H. Effect of Tilt Angle on the Multi-Pipe Channel with Sinusoidal/Curved Walls-Numerical Modelling Based on Finite Volume Method. *Int. J. Numer. Methods Heat Fluid Flow* **2019**, *29* (5), 1590–1605. https://doi.org/10.1108/HFF-07-2018-0390.

(48) Moriwake, H.; Kuwabara, A.; Fisher, C. A. J.; Huang, R.; Hitosugi, T.; Ikuhara, Y. H.; Oki, H.; Ikuhara, Y. First-Principles Calculations of Lithium-Ion Migration at a Coherent Grain Boundary in a Cathode Material, LiCoO2. *Adv. Mater.* **2013**, *25* (4), 618–622. https://doi.org/10.1002/ADMA.201202805.

(49) Fisher, C. A. J.; Huang, R.; Hitosugi, T.; Moriwake, H.; Kuwabara, A.; Ikuhara, Y. H.; Oki, H.; Ikuhara, Y. High-Coincidence Twin Boundary in Lithium Battery Material LiCoO 2. *Nanosci. Nanotechnol. Lett.* **2012**, *4* (2), 165–168. https://doi.org/10.1166/NNL.2012.1301.

(50) Li, H.; Dey, S.; Castro, R. H. R. Kinetics and Thermodynamics of Densification and Grain Growth: Insights from Lanthanum Doped Zirconia. *Acta Mater.* **2018**, *150*, 394–402. https://doi.org/10.1016/J.ACTAMAT.2018.03.033.

(51) Hasan, M. M.; Dey, S.; Nafsin, N.; Mardinly, J.; Dholabhai, P. P.; Uberuaga, B. P.;

Castro, R. H. R. Improving the Thermodynamic Stability of Aluminate Spinel Nanoparticles with Rare Earths. *Chem. Mater.* **2016**, *28* (14), 5163–5171. https://doi.org/10.1021/ACS.CHEMMATER.6B02577/ASSET/IMAGES/ACS.CHEMMATER.6B02577.SOCIAL.JPEG_V03.

(52) Murdoch, H. A.; Schuh, C. A. Estimation of Grain Boundary Segregation Enthalpy and Its Role in Stable Nanocrystalline Alloy Design. https://doi.org/10.1557/jmr.2013.211.

(53) TASKER, P. W.; COLBOURN, E. A.; MACKRODT, W. C. Segregation of Isovalent Impurity Cations at the Surfaces of MgO and CaO. *J. Am. Ceram. Soc.* **1985**, *68* (2), 74–80. https://doi.org/10.1111/J.1151-2916.1985.TB15268.X.

(54) Castro, R. H. R. Interfacial Energies in Nanocrystalline Complex Oxides. *Curr. Opin. Solid State Mater. Sci.* **2021**, *25* (3), 100911. https://doi.org/https://doi.org/10.1016/j.cossms.2021.100911.

(55) Hasan, M. M.; Dholabhai, P. P.; Dey, S.; Uberuaga, B. P.; Castro, R. H. R. Reduced Grain Boundary Energies in Rare-Earth Doped MgAl2O4 Spinel and Consequent Grain Growth Inhibition. *J. Eur. Ceram. Soc.* **2017**, *37* (13), 4043–4050. https://doi.org/10.1016/J.JEURCERAMSOC.2017.04.073.

(56) Jain, A.; Ong, S. P.; Hautier, G.; Chen, W.; Richards, W. D.; Dacek, S.; Cholia, S.; Gunter, D.; Skinner, D.; Ceder, G.; Persson, K. A. Commentary: The Materials Project: A Materials Genome Approach to Accelerating Materials Innovation. *APL Materials*. American Institute of Physics Inc. July 18, 2013, p 11002. https://doi.org/10.1063/1.4812323.

(57) Patel, F.; Patel, S. La1-XSrxCoO3 (X=0, 0.2) Perovskites Type Catalyst for Carbon Monoxide Emission Control from Auto-Exhaust. *Procedia Eng.* **2013**, *51*, 324–329.

https://doi.org/10.1016/J.PROENG.2013.01.044.

(58) Ihrig, M.; Finsterbusch, M.; Laptev, A. M.; Tu, C. H.; Tran, N. T. T.; Lin, C. A.; Kuo, L. Y.; Ye, R.; Sohn, Y. J.; Kaghazchi, P.; Lin, S. K.; Fattakhova-Rohlfing, D.; Guillon, O. Study of LiCoO2/Li7La3Zr2O12:Ta Interface Degradation in All-Solid-State Lithium Batteries. *ACS Appl. Mater. Interfaces* **2022**, *14* (9), 11288–11299. https://doi.org/10.1021/ACSAMI.1C22246.

(59) Takeuchi, S.; Tan, H.; Bharathi, K. K.; Stafford, G. R.; Shin, J.; Yasui, S.; Takeuchi, I.; Bendersky, L. A. Epitaxial LiCoO 2 Films as a Model System for Fundamental Electrochemical Studies of Positive Electrodes. **2015**. https://doi.org/10.1021/am508512q.

(60) Bates, J. B.; Dudney, N. J.; Neudecker, B. J.; Hart, F. X.; Jun, H. P.; Hackney, S. A. Preferred Orientation of Polycrystalline LiCoO 2 Films. *J. Electrochem. Soc.* **2000**, *147* (1), 59–70.

(61) Xia, H.; Lu, L. Texture Effect on the Electrochemical Properties of LiCoO2 Thin Films Prepared by PLD. *Electrochim. Acta* **2007**, *52* (24), 7014–7021. https://doi.org/10.1016/J.ELECTACTA.2007.05.019.

Chapter 4: Enhanced Thermodynamic Stability of Delithiated $LiCoO_2$ by Dopant Segregation

Abstract

The intercalation and deintercalation process of lithium ion batteries inevitably causes capacity fading due to the irreversibility of lithium intercalation into the cathode. This problem is exacerbated in nanoscale cathode materials due to the high surface area and reactivity of the surface. Improving the stability of nanoscale cathode materials is important and understanding the delithiated states is crucial in the design of the nanoparticles, but delithiated states of cathodes are difficult to study because of the inherent instability. This work utilized a water adsorption microcalorimetry methodology to measure the surface energies of stoichiometric and delithiated $LiCoO_2$ (LCO) nanoparticles. Lanthanum doped LCO nanoparticles were also synthesized to study the effect of dopant segregation on the surface energies of delithiated states. The surface energies of the undoped LCO were measured to be 1.23 and 1.33 J/m^2 calculated by two different methods and the La-doped LCO was determined to be 1.07 and 1.09 J/m^2. The surface energies are again confirmed to decrease due to La segregation as was found in Chapter 3. The $Li_{0.71}CoO_2$ nanoparticles had surface energies of 1.02 and 1.07 J/m^2 and La-$Li_{0.57}CoO_2$ had surface energies of 1.08 and 1.04 J/m^2. The La doping helps stabilize the energetic landscape of the surfaces compared to the undoped nanoparticles that see a considerable decrease in surface energy upon delithiation. This stabilization of the surface structures could be very beneficial in improving the reversibility of Li intercalation into nanoparticles, because of the high fraction of surfaces in nanoscale materials.

Introduction

Lithium ion batteries are a growing part of the energy storage landscape and continue to progress into more applications.[1] The degradation of materials, transition metal dissolution, and intergranular cracking leading to capacity fading continue to limit the overall effectiveness and prevalence of lithium ion technology.[2] In the pursuit of improving battery technology, nanomaterials could be an effective method for enhancing Li diffusion and expanding the application of the technology as it helps improve properties in other ceramics.[3,4]

However, as the scale of cathode materials decreases to the nanoscale, many of the degradation mechanisms can be exacerbated.[5–7] Most of the issues emerge from the instability at interfaces, which constitutes a greater volume fraction when particle sizes are below 20 nm. Surface energies play a critical role in thermodynamic and electrochemical stability at this scale as can be seen by problems like cycling induced coarsening.[8] One method for controlling surface stability is decreasing the surface energies through dopant segregation and promoting surface excess following the Gibbs adsorption isotherm.[9,10] Nakajima et al. recently explored Sc-doped $LiMn_2O_4$ nanoparticles and confirmed Sc segregates to interfaces and decreases the surface energy.[11] Leong et al. electrochemically cycled the nanoparticles to find the doped material maintained ~97% of the initial capacity compared to 88% retention for the undoped LMO.[12] Combined, the studies support that designed dopant segregation can help improve capacity retention in nanoparticles by lowering the surface energies in the stoichiometric LMO. However, the thermodynamic stability of cathodes at the delithiated state is likely more relevant in the scenario of an operating battery than the original stoichiometric states. This begs the question whether the surface energy is impacted by delithiation and how the segregated dopants do help stabilize the nanomaterials in this state.

This work strives to experimentally measure the surface energies of stoichiometric and delithiated $LiCoO_2$ (LCO) nanoparticles, and to further explore the stabilization effect of dopant segregation in both conditions. While one other group has attempted to experimentally measure average surface energies of LCO, delithiated states have only been studied with DFT, without addressing the effects of doping on LCO surface energies.[13–15] In this work, water adsorption and calorimetry are used to measure the surface energies of LCO nanoparticles and La-doped LCO nanoparticles. The nanoparticles were also chemically delithiated to synthesize nanoparticle stoichiometries of $Li_{0.71}CoO_2$ and La-$Li_{0.57}CoO_2$. This is an effective method for quantitatively measuring the difference in surface energetics for nanoparticles with manipulated interfaces. This method differs from the calorimetry method previously described in Chapter 3 where the heat of sintering was measured to determine interfacial energies. Although that methodology can provide grain boundary energies, it also requires high temperatures in the heating profile in order to measure a significant amount of heat from the sintering profile. The water adsorption method is run at room temperature and can therefore be utilized to study the surface energies of more sensitive samples like delithiated structures. Specifically, the ability to measure the surface energies with very little material processing is useful for measuring the more reactive delithiated states of the cathode.

Experimental Section

Synthesis

$LiCoO_2$ (LCO) nanoparticles were synthesized by adapting the hydrothermal synthesis methods developed by Okubo et al.[6] A 100 mL precursor solution of 20 mmol of $Co(NO_3)_2{\cdot}6H_2O$ was slowly poured into 100 mL of room temperature 5 M NaOH solution. After the coprecipitation of the pink $Co(OH)_2$ nanoparticles, the suspension was stirred for ~20

minutes and then added to 1800 mL of deionized (DI) water. The diluted suspension was stirred for ~48 hours and air was bubbled through the particles to oxidize the nanoparticles into the brown CoOOH nanoparticles. The CoOOH nanoparticles were then centrifuged and washed five times with DI water to remove all NaOH and the particles were dried at 80°C overnight. For the doped nanoparticles, 1 mol percent of the Co precursor was replaced with $La(NO_3)_3 \cdot 6H_2O$ to yield a La doped CoOOH. Then 500 mg of the ground CoOOH precursor was added to 133 mL of 1 M LiOH in a 200 mL autoclave with a PTFE liner (4748A, Parr Instrument Company). After stirring, the sealed suspension in the autoclave was placed in the furnace at 100°C, heated to 180°C at a rate of 0.5°C/min, held for 12 hours, and cooled to 100°C at 1°C/min. The suspension was then removed and cooled to room temperature. The particles were centrifuged and washed with DI water four times to remove any excess LiOH and dried at 80°C overnight. The hydrothermal process results in the dissolution of CoOOH particles and the nucleation and crystallization of the LCO phase. The dried pellets were ground with a mortar and pestle and then calcined at 300°C for 3 hours in air to promote the complete oxidation of the LCO nanoparticles.

The synthesized samples were also taken through a chemical delithiation process to remove a fraction of the lithium. 100 mg of the calcined LCO nanoparticles was added to 5 mL of 1.0 M HNO_3 and 0.1 M HNO_3. The suspensions were then agitated every ~5 minutes and left in the nitric acid solutions for 5, 10, and 30 minutes. After the nitric acid treatment, the suspensions were diluted into 10 mL of DI water and centrifuged immediately. The suspensions were washed three times with DI water to remove all the nitric acid and dissolved lithium and then dried at 80°C overnight.

Characterization

The phase of the crystalline nanoparticle was determined with a Bruker AXS D8 Advance powder diffractometer (Bruker Corp., CuKα radiation, λ=1.5406 Å) at a 40kV voltage and emission current of 40 mA. The Match and Jade MDI software were used to identify the crystal phase of the nanoparticles. Inductively coupled plasma mass spectrometry (ICP-MS, Agilent-7900) was conducted to determine the stoichiometry of the Li, Co, and La in the as synthesized and delithiated nanoparticles. The instrument utilizes a quartz spray chamber, MicroMist concentric gas nebulizer, and nickle sampler with skimmer cones. The argon carrier gas flow rate was 1.0 L/min with a helium flow of 4.5 mL/min in helium mode to prevent polyatomic interferences.

Water Adsorption

The water adsorption experiments and microcalorimetry measurements were used to quantitatively determine the average surface energies of different materials. The measurement of solid surface energies has been achieved through several different methods including elastic modulus, wetting angle, and calorimetric techniques.[16–20] However, measuring true anhydrous surface energies of solids can be a difficult due to the adsorbed gas and vapor species on surfaces. An effective degassing method must be used to prepare nanoparticle surfaces for energetic measurements.

Fang et al. proposed a method for measuring the surface energies of nanoparticles through an enclosed apparatus using the vapor pressure of water.[21] They proposed **Equation 1** for calculating the surface energy of nanomaterials, γ_0, where R is the ideal gas constant, T is the

$$\gamma - \gamma_f = \frac{RT\sum n}{A}\ln\frac{P_f}{P} \quad \textbf{(1)}$$

temperature, n is the number of water molecules adsorbed to the surface at a specific time, A is the total surface area of the nanoparticles, P is the vapor pressure at time t, P_f is the final vapor pressure at equilibrium, and γ_f is the final surface energy at equilibrium. For particles with saturated surfaces, the surface energy is 0.072 J/m^2 since the surface approaches the surface energy of water. One has to be careful to ensure high relative pressures of water vapor are achieved to ensure the surface water has fully transitioned from ice-like surface structure to the liquid-like surface water.[22] Therefore, to determine the surface energy P, P_f, and n need to be measured by measuring the water vapor pressure as water is dosed onto the surface and calculating n from the ideal gas law. Fang et al. also confirmed in previous studies that the treatment of water vapor as an ideal gas for the adsorption experiments is a valid approximation.[23]

In the previous case, the surface energy is calculated from the water adsorption behavior and water vapor pressure alone. However, secondary methods of calculating surface energies can be useful to corroborate the surface energy results. Water adsorption measurements result in a layer of adsorbed water molecules on the surface of the solid that follows the Gibbs adsorption equation (**Equation 2**).[24] In this case, γ is the surface energy, S_a^σ is the excess entropy per surface area, T is temperature, Γ_i is the excess adsorbed amount of species i per surface area, and

$$d\gamma = -S_a^\sigma dT - \sum_i \Gamma_i \mu_i \quad \textbf{(2)}$$

μ_i is the chemical potential of species i. For pure vapor adsorption onto an insoluble solid surface, the surface excess entropic term is zero and only the second term remains. The surface energy in this case is dependent on the integral of the surface excess of water vapor, because it is only single species adsorption.

However, this model falls short in characterizing the complete adsorption process that takes place at high water coverages that are necessary to reach the 0.072 J/m^2 surface energy. Adamson and Schlangen et al. describe the process of the two stage adsorption transitioning from a dissociative chemisorption stage to a physisorption water layer.[24,25] **Equation 2** only describes the initial thin adsorbed film, so a more comprehensive equation is necessary to describe the solid-liquid interface and the liquid-vapor interface. Quach et al. proposed **Equation 3** to describe the Gibbs free energy associated with the water adsorption process, where n_{ads} is

$$\Delta G = G(Surface, n_{ads}H_2O(adsorbed) - G(Surface) - n_{ads}\mu_{H_2O} \quad \textbf{(3)}$$

the number of adsorbed molecules and μ_{H_2O} is the chemical potential of water.[26] Similar to **Equation 2**, if the bulk energy remains unchanged and adsorption is reversible, the entropic and pV terms can be neglected. **Equation 3** then becomes **Equation 4**, where γ^s is the surface energy at some

$$\gamma^s = \gamma_0^s + \theta\Delta H_{ads} \quad \textbf{(4)}$$

surface coverage, γ_0^s is the anhydrous surface energy, θ is the surface coverage in moles of H_2O, and ΔH_{ads} is the heat of adsorption (kJ/mol) of water vapor onto the surface. It's important to note that the heat of adsorption is dependent on the surface coverage term, θ, as heats of adsorption tend to be much more exothermic at lower surface coverages. **Equation 4** specifically uses the thermodynamic properties of water adsorption to calculate the surface energy. This provides a secondary method to corroborate **Equation 1** proposed by Fang et al. that reaches the surface energy from a different quantitative measure. Additionally, the calculations are not limited by knowing which adsorption layer is present throughout the experiment when using the

heat of adsorption. Regardless of the adsorption mechanism, the DSC will capture all heat associated with the water interacting with the surface.

An important part of the microcalorimetry method is to understand the surface interfaces and equilibrium states of the surface at high water coverages. As was previously mentioned, it's imperative to continue the measurement until the surface has reached high enough coverages for the surface to resemble liquid-like water layer. At this point the surface energy has reached the surface tension of water and is equivalent to 0.072 J/m^2. At this point, the surface energy will no longer change since the chemical potential change of water molecules will have a negligible effect on the surface. When the surface reaches a liquid-like state in the microcalorimetry method, the heat of adsorption should equal the heat of a water molecule adsorbing to a water droplet. This value is equivalent to the enthalpy of liquefaction of water (-44 kJ/mol) as proven by previous water adsorption experiments.[27] The heat of adsorption converges to -44 kJ/mol at relatively low coverages with surfaces that are mostly hydrophilic in nature, but the heat of adsorption can also deviate to less negative values if there are enough hydrophobic sites present.[28] This is a common occurrence for nanoparticles that have a wide array of surface planes and have varying surface chemistries depending on synthesis method. For this set of experiments, both **Equation 1** and **Equation 4** were used to calculate the surface energy of the doped and undoped nanoparticles.

For this experiment, a 3Flex Surface Analyzer (Micromeritics Instrument Corporation) was used for the water adsorption measurements and a Sensys Evolution DSC (Setaram Inc.) for the calorimetric measurements. A total surface area of about 2 m^2 is necessary to measure the heats of adsorption, so the BET surface area was measured and enough powder was weighed out to reach at least 2 m^2 of surface area. The powder was then hand pressed into 2 mm diameter

pellets of about 10-15 mg to ensure the nanoparticles stay in the sample tube during degassing. The sample tubes were then attached to the DSC and 3 Flex and degassed under vacuum and temperature. The samples were degassed for 12 hours and a degassing temperature of 180°C was used for the delithiated samples and 300°C for the stoichiometric samples. Toward the end of the degassing segment, oxygen was introduced into the sample tube for ~20 minutes and then vacuum was reintroduced. This process was repeated two more times to ensure the surface was clean and then oxygen was backfilled again for ramping the temperature back to 25°C. The oxygenated environment ensures the nanoparticles are fully oxidized and there is no cobalt reduction near the surface. Once the sample tube equilibrates to 25°C, the vacuum is reestablished for ~1 hour and the BET measurement and water dosing starts. The 3Flex introduced water vapor at a rate of 2 μmol per dose and the equilibration time was set to 2 hours, 1 hour, and 0.5 hour. The DSC measured the heat of adsorption for each dose and the equilibration time was reduced as the experiment proceeded, because the initial heats of adsorption at lower partial pressures tend to require longer times to capture the entire heat effect of adsorption. The experiment proceeded until a vapor pressure ($\frac{p}{p_o}$) of ~0.72 was reached. For more background on the microcalorimetry method, the reader is referred to past publications.[26,27]

Results and Discussion

The doped and undoped nanoparticles were synthesized with the hydrothermal method described and then calcined at 300°C. The XRD patterns of the nanoparticles are shown in **Figure 4.1** and confirm the presence of the LCO phase. Dopant segregation can cause the formation of the La secondary phases if the segregation enthalpy is too high,[29] but none of the expected La rich secondary phases seen in other cases (La_2O_3, $LaCoO_3$) are observed here.[30,31] The peak broadening in the samples confirm the nanoscale nature of the particles through

estimation by the Scherrer formula.[32,33] The TEM images shown in Chapter 2 and 3 also confirm the nanoscale nature of the particles with the nanoplatelet morphology. A secondary phase of Co_3O_4 has been detected in LCO samples calcined at elevated temperatures, but appear to only be present in dilute concentrations in these samples and have much lower intensities than the LCO peaks.

The calcined nanoparticles were also taken through a chemical delithiation in 1.0 M and 0.1 M HNO_3 and the ICP-MS results of the nitric acid washing are shown in **Table 1**. The ICP measurements reveal nearly stoichiometric nanoparticles were synthesized with an undoped LCO Li/Co ratio of 1.02 and a La-doped LCO ratio of 0.96. The washing with 1.0 M nitric acid significantly delithiated the samples to a Li/Co concentration of 0.37 to 0.25 for 5 to 30 minutes of acid washing. LCO structures delithiated below a Li/Co content of 0.5 go through a phase transition and LCO particles are electrochemically unstable below this point due to the overlapping energy states of Co and O that cause oxygen gas formation.[34–36] For this reason, a lower concentration of 0.1 M nitric acid was used to delithiate the LCO samples and produced Li/Co values ranging from 0.71 to 0.53 for a 5 to 30 minute wash. Similarly, the La-doped LCO nanoparticles had a Li/Co content ranging from 0.58 to 0.55. The La-doped nanoparticles had a greater amount of delithiation compared to the undoped nanoparticles. Another concern is the degree of Co and La dissolution, but the Co concentration remained consistent in the undoped samples studied and the La-doped LCO particles maintained a La/Co ratio of 0.011. These results show there was minimal Co and La dissolution and matches the initial doping level that substituted 1 mol percent of Co for the La in the coprecipitation. The samples with a wash time of 5 minutes in the acid were used for the water adsorption analysis to limit any structural or chemical changes induced by the acid at long residence times. Additionally, the XRD patterns in

Figure 4.1 show that the crystal structure was maintained after delithiation and the intensity and positions of the peaks are all generally the same as before the acid wash. Chemical delithiation was chosen for lithium removal because it is easier to collect the particles afterwards and can be easily scaled to larger amounts. Chemical delithiation yields similar particles to electrochemical delithiation, and although they might not be identical it is quite common to study structural and thermodynamic properties of these materials.[37–40]

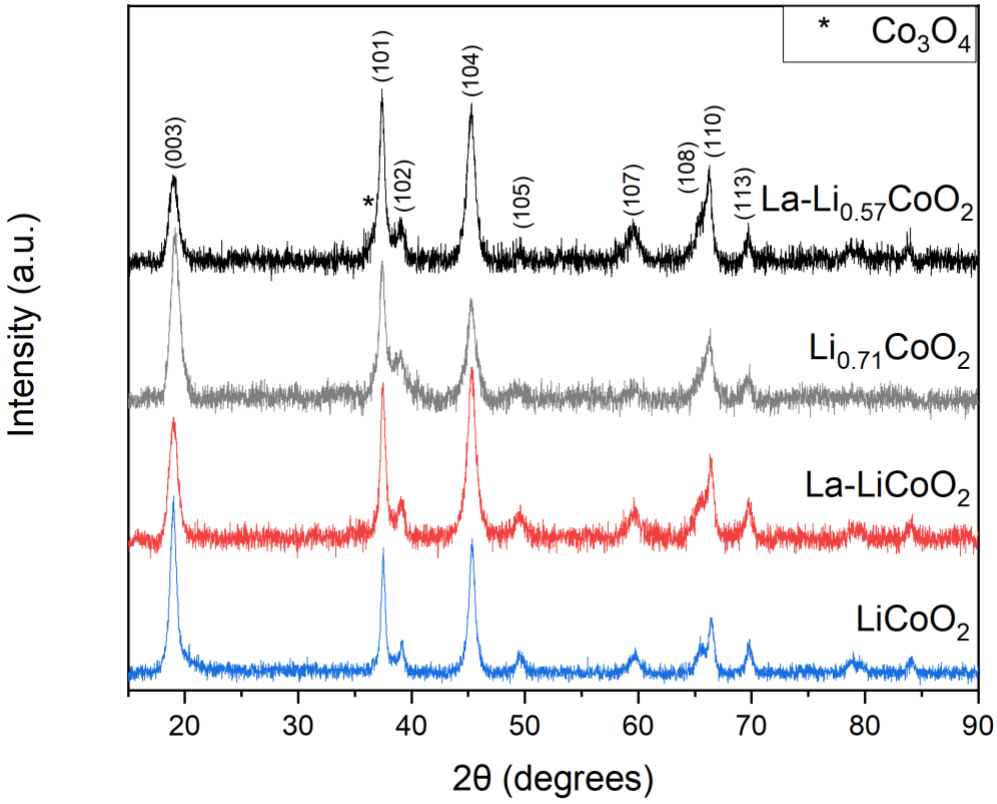

Figure 4.1. XRD patterns of the undoped and La-doped LCO nanoparticles calcined at 300°C and the patterns for the chemically delithiated nanoparticles of $Li_{0.71}CoO_2$ and La-$Li_{0.57}CoO_2$. The * indicates the peak corresponding to the Co_3O_4 phase.

Table 4.1. ICP-MS results of the nitric acid washed LCO and La-doped LCO nanoparticles.

Sample	Acid Concentration	Time (min)	Li/Co	La/Co
LCO	0.1 M	0	1.02	—
		5	0.71	—
		10	0.71	—
		30	0.53	—
	1.0 M	5	0.37	—
		10	0.26	—
		30	0.21	—
1% La-LCO	0.1 M	0	0.96	0.011
		5	0.57	0.011
		10	0.58	0.011
		30	0.55	0.011

The four samples chosen for water adsorption were the nearly stoichiometric undoped LCO (Li/Co=1.02) and La-doped LCO (Li/Co=0.96), and the delithiated nanoparticles of $Li_{0.71}CoO_2$ and La-$Li_{0.57}CoO_2$ after 5 minutes of acid washing in 0.1 M HNO_3. After the samples were properly degassed, the water adsorption measurement was started and the adsorption isotherms are shown in **Figure 4.2**. The isotherms match a Type II isotherm with an initial steep sloped linear section at very low relative pressures.[41] This behavior follows the same adsorption behavior as oxides measured previously, although the initial linear section appears to go to higher water coverages compared to some oxides like the Al_2O_3 isotherm.[26,42] In particular, the stoichiometric LCO goes to the highest water coverages at low relative pressures, which is an initial sign that it may have a higher surface energy. In this case, it takes more adsorbed water species to cover the surface and satisfy the high energy sites on the surface before the relative pressure starts increasing. Additionally, the water coverage is higher than the other three samples until higher relative pressures (>0.3) when the uncertainty of the measurement begins to increase. In general, the other three samples exhibit similar isotherms and all of them display the same adsorption behavior over the range of relative pressures.

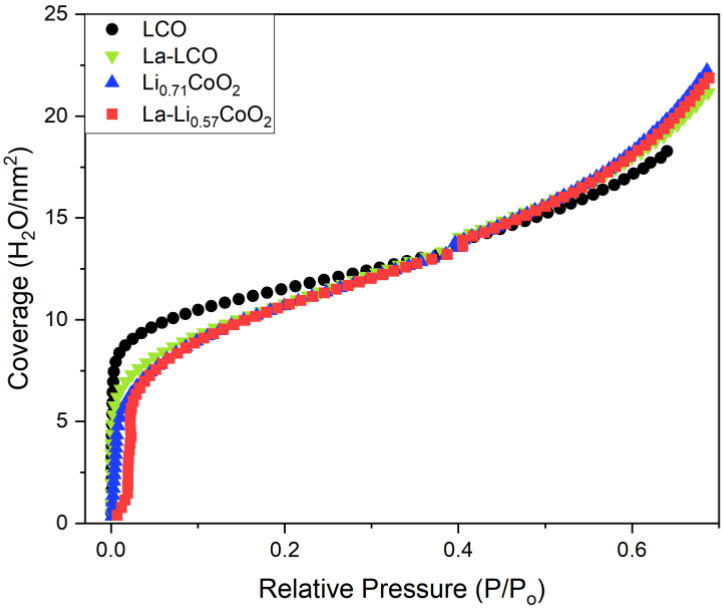

Figure 4.2. Water adsorption isotherms for the doped and undoped LCO nanoparticles and the delithiated structures.

The heats of adsorption were concurrently measured during the water adsorption experiment to quantify the heat released while water adsorbed to the surface. **Figure 4.3a** shows the heat of adsorption plotted against the water coverage for the stoichiometric LCO and La-LCO. The initial heats of adsorption at lower water coverages are more exothermic than the heats at higher water coverages. This is due to the highly reactive nature of anhydrous surface sites and the large amount of energy released from the first monolayer of adsorbed water. The initial heat of adsorption for the undoped LCO is -71 kJ/mol and reaches a minimum of -89 kJ/mol, and the initial heat of adsorption for La-LCO is -79 kJ/mol and a minimum of -90 kJ/mol. The high enthalpies of adsorption are also consistent with the chemisorption model previously introduced and the dissociative behavior of water in this stage.[43,44] This matches the results from Cherkashinin et al. where they showed a dissociative water adsorption process on the surface of

LCO.[45] They showed that water is able to dissociate into hydroxyl groups when bound to surface defects like oxygen vacancies and reactive surface Li atoms. Kim also showed a water adsorption mechanism demonstrating water adsorbing to surface lithium at the {003} surface plane.[46] The curves then increase sharply to the heat of liquefaction of water (-44 kJ/mol) when the surface becomes more liquid-like and water molecules are adsorbing onto water. The La-LCO increases first around a coverage of ~6 H_2O/nm^2 and the undoped LCO increases later around ~8 H_2O/nm^2. This difference suggests that more water coverage is necessary to stabilize the anhydrous surfaces of the undoped LCO and this corroborates the results observed in the linear portion of the adsorption isotherm (**Figure 4.2**). This transition from highly exothermic heats to the heat of liquefaction captures the transition from chemisorption to the physisorption stage.

These data points have some variability in the values from low to high water coverages that is a new adsorption behavior not previously recorded through this method. The materials studied in past experiments have exhibited more of an exponential increase in heats of adsorption with respect to the water coverage with less variability between consecutive data points.[47,48] However, most of the morphologies studied can be approximated as spherical or nearly spherical as a tetrakaidecahedron. This synthesis method yields nanoplatelet structures with large differences in aspect ratios between the thin thicknesses and large specific surface areas of the length and width. We hypothesize that the plate-like morphology of the particles yields more highly exothermic values at low coverages for the heat of adsorption instead of seeing a gradual increase in the heats of adsorption. These more exothermic values lead to a sigmoidal-like shape in the heats of adsorption compared to an exponential due to the high fraction of a few surface planes. Although the surface planes may be similar, the individual adsorption sites can vary and

cause the fluctuations in the enthalpies measured even at high water coverages. As explained before, water can form structures on the surface of oxides due to the strong hydrogen bonding of water.[22,26] The anisotropic growth of water or ice-like structures on the surface of different materials has been observed and shows that water can preferentially grow long interconnected chains from certain surface planes or morphologies.[49,50] These evolving surface structures can lead to metastable states that lower or raise the heat of adsorption as the water restructures itself on the surface. It's important to note that this data isn't being fitted with any functional equation and only the cumulative effect of the heats of adsorption are being taken into account.

Figure 4.3b shows the heats of adsorption for the delithiated nanoparticles of $Li_{0.71}CoO_2$ and La-$Li_{0.57}CoO_2$. Both of these samples have a less abrupt transition from the dissociative water adsorption phase to the physisorption stage. Additionally, the shape of the curves, the La-$Li_{0.57}CoO_2$ especially, tend to be more exponential in shape compared to the stoichiometric samples. The delithiation of the samples seems to have created a larger distribution of adsorption sites, which leads to highly exothermic heats in the anhydrous state and a more gradual transition to the liquid-like surface coverage. The delithiated La-LCO has some high energy sites in the anhydrous state that leads to the greatest exothermic heats at low water coverages of -112 kJ/mol and -79 kJ/mol for the $Li_{0.71}CoO_2$. The higher heats of adsorption could be due to the higher degree of delithiation in the doped sample and the introduction of more surface defects. This would follow the dissociative model developed by Cherkashinin et al. where dissociation of water primarily happened at surface defects like oxygen vacancies and surface lithium.[45] The two curves follow similar adsorption behaviors after the very low coverage region (>2 H_2O/nm^2) by converging to -44 kJ/mol and following similar behavior in the isotherm as well (**Figure 4.2**).

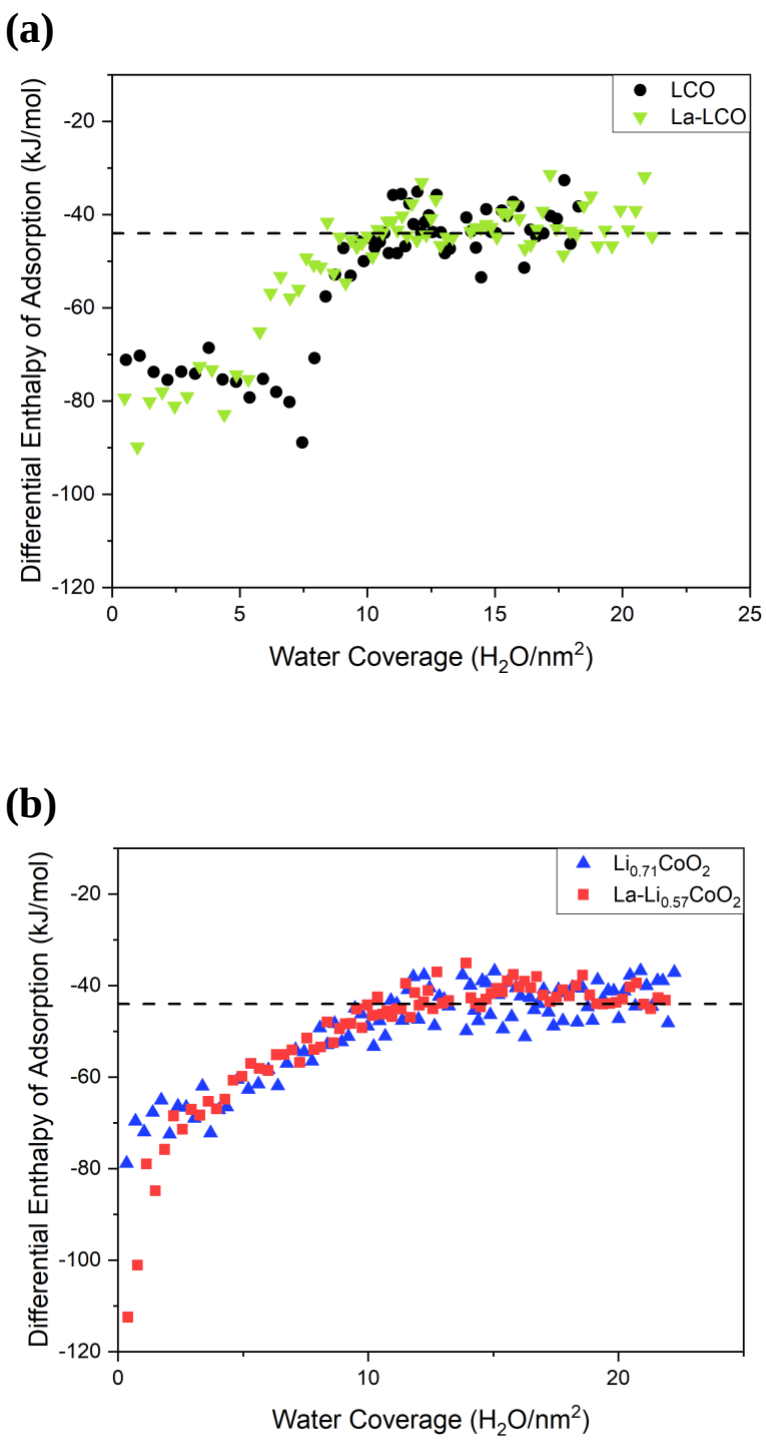

Figure 4.3. Differential enthalpies of adsorption measured with the water coverage for (a) LCO and La-LCO, and (b) $Li_{0.71}CoO_2$ and La-$Li_{0.57}CoO_2$.

The surface energies were then calculated from the water adsorption data and the microcalorimetry data. **Equation 4** was used to calculate the surface energy from the heats of adsorption and **Equation 1** developed by Fang et al. was used to calculate surface energies from the water adsorption data alone. The results are summarized in **Table 4.2** for all four of the samples. The surface energies from microcalorimetry were calculated by finding the point where the heats of adsorption intersect with the heat of liquefaction at -44 kJ/mol. The surface energy at this point is set to 0.072 J/m^2 and is equivalent to the variable, γ^s. From this boundary condition, the water coverage and heats of adsorption were cumulatively added to each other to reach the anhydrous surface energy, γ_0^s. A similar method of establishing the boundary condition where the surface becomes liquid-like and the energy reaches 0.072 J/m^2 was used for the Fang surface energies. Determining the relative pressure or water coverage value where the surface reaches the surface tension of water, is difficult from just looking at the adsorption isotherms. The calorimetry data is one of the best indicators of the correct water coverage point where the surface becomes liquid-like. The water adsorption data can also be used by calculating surface energy from the relative pressure data with no assumption of the boundary conditions through **Equation 1** and plotting it against the water coverage data. **Figure 4.4** shows the derivative of the calculated energies to look for inflection points where the rate of change of the energies begins to decrease after the plateau between coverages of 7 and 11 H_2O/nm^2. This range is of specific interest since the heat of adsorption data nears -44 kJ/mol in this region and the inflection after the plateau indicates a change in the water adsorption mechanism. The LCO and La-LCO are the easiest to determine where the rate of change begins decreasing significantly after the plateaus near coverage of 10 and 9 H_2O/nm^2, respectively. The delithiated samples have continuous decreases in the derivatives and inflection points are more difficult to establish, so the

second derivative was plotted and showed an inflection near 9.5 H_2O/nm^2. All of these values were compared to the heats of adsorption and had good agreement with the water coverage where the heats converged to -44 kJ/mol. Using the set of data from **Figure 4.3** and **Figure 4.4** the boundary conditions for each sample were set and are in **Table 4.2**.

Table 4.2. Anhydrous surface energies of all four LCO samples calculated from **Equation 1** and **Equation 4** and the water coverage value where the surface energy is equivalent to 0.072 J/m^2.

Sample	Surface Energy (microcalorimetry) (J/m^2)	Surface Energy (Fang Eqn.) (J/m2)	Water Coverage @ γ=0.072 J/m^2 (H_2O/nm^2)
LCO	1.23	1.33	10.08
$Li_{0.71}CoO_2$	1.02	1.07	9.47
La-LCO	1.07	1.09	8.92
La-$Li_{0.57}CoO_2$	1.08	1.04	9.53

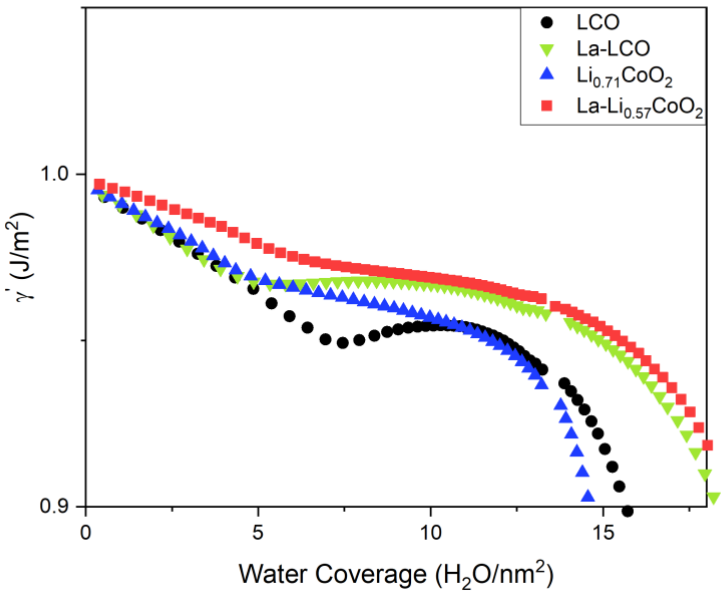

Figure 4.4. Derivative of the surface energy calculated from **Equation 1** for all four samples as a function of water coverage.

The surface energy of the undoped LCO nanoparticles was consistently higher for both methods compared to the other three samples. The La-doped surface energies were reduced from 1.23 J/m^2 to 1.07 J/m^2 for the calorimetric data and from 1.33 J/m^2 to 1.09 J/m^2 with the equation from Fang. The decrease in surface energy is expected from the La segregation to interfaces and following results from previous studies.[11,51] These results also follow the previous results utilizing the heat of sintering to determine the interfacial energies in Chapter 3. Those results produced a surface energy of 1.30 J/m^2 for the undoped LCO and 1.11 J/m^2 for the La-doped LCO. These values are in good agreement with the water adsorption measurement and provide more direct evidence that the La helps stabilize the nanoparticle surfaces. Experimental measurements of LCO surface energies through drop solution calorimetry and water adsorption were also attempted by Maram et al.[13] They calculated an anhydrous surface energy of 1.25 J/m^2 which is also in excellent agreement with the previous measurements. Additionally, several groups have computationally studied LCO surface energies and reported values of ~1.0 J/m^2 for {001} surfaces, ~1.1 for {104} surfaces, and ~2.2 J/m^2 for {110} surfaces.[15,52] It's important to note that the experimental methods measure average surface energies, but the surfaces contained in the nanoplatelets are predominately {001} and {104} with a few other low index surfaces. The surface energies measured for the nanoplatelet morphology matches well with this assumption assuming predominately low energy surfaces in the 1.0-1.1 J/m^2 range with a fraction of higher energy surfaces that raise the overall average surface energy. Overall, the experimental measurements are consistent with previous experimental and theoretical work measuring the surface energies.

The delithiated LCO sample also decreased in surface energy relative to the stoichiometric LCO. The $Li_{0.71}CoO_2$ decreased to a surface energy of 1.02 J/m^2 for the

calorimetry method and to 1.07 J/m^2 for the Fang equation. Intuitively, one might expect a surface energy increase for the delithiated sample due to the reported degradation mechanisms that occur in LCO during battery cycling.[53] Kramer and Ceder actually reported DFT calculations showing the opposite effect for {001} surfaces and discovered surface energies decrease as surfaces are delithiated.[52] The polar {001} surface has a few different termination layers (Li, Co, O), but the Li layer termination is the most stable as the O termination requires a strongly reducing environment to be stable and under coordinated surface Co is unfavorable.[54] Therefore, the most likely surface termination is at a Li layer, so constructed surfaces were made with a half monolayer (1/2 ML) of Li on the top and bottom surface for the fully stoichiometric LCO case which yielded a surface energy of ~1.0 J/m^2. They also studied Li terminations that reduced the surface Li to a 3/8 ML, 1/4 ML, and 1/8 ML and saw a corresponding decrease in surface energy with less surface Li. The 3/8 ML slightly decreased surface energy to ~0.95 J/m^2 and the 1/4 ML stability window ranges from a surface energy of 0.6-0.95 J/m^2. The acid washing of the {001} surface leads to chemical delithation and a consequent reduction in average surface energy of the $Li_{0.71}CoO_2$ from the decrease in {001} surface energies. Future studies will address this effect further by doing more surface energy measurements on delithiated samples of LCO.

Contrastingly, there was essentially no change to the La-doped sample that was delithiated to La-$Li_{0.57}CoO_2$. The surface energies of La-$Li_{0.57}CoO_2$ were 1.08 J/m^2 for the calorimetry data and 1.04 J/m^2 for the Fang method, which are very close to the values for the stoichiometric La-LCO. This is an interesting result that shows the stabilization effect of dopant segregation at surfaces. The undoped LCO saw a reduction of 0.21-0.26 J/m^2 upon delithiation to a Li content of 0.71, but the La-doped sample saw changes <0.05 J/m^2 for delithiation to 0.57. If

there was no stabilization effect of the La, one would expect a more significant decrease in surface energy relative to the undoped LCO due to the higher degree of delithiation. The dilute doping of surface La must stabilize the surface energy to prevent large fluctuations in the surface stability regardless of lithium content at these Li levels studied.

The surface energies were also plotted as a function of water coverage for both methods with the calorimetry method shown in **Figure 4.5a** and the surface energies calculated from the Fang equation shown in **Figure 4.5b**. Both figures show the undoped LCO has the highest surface energy regardless of the water coverage. As expected from the data in **Table 4.2**, the other three samples follow similar surface energy trends since they have very close anhydrous surface energies. The two figures demonstrate the difference in the two calculation methods comparing the calorimetry data to the pure water adsorption data. Both methods have the same boundary condition declaring the surface energy equivalent to 0.072 J/m^2 at a given coverage and approach the anhydrous surface energy at very low water coverages. However, **Equation 1** has a greater dependence on the water coverage at higher water coverages and has smaller effect on surface energies at low coverages. The surface energies from **Equation 4** have more of a linear dependence on the water coverage due to the cumulative summing of the heats of adsorption. Although there are differences in the water coverage dependence, both equations used were able to provide surface energies consistent with each other.

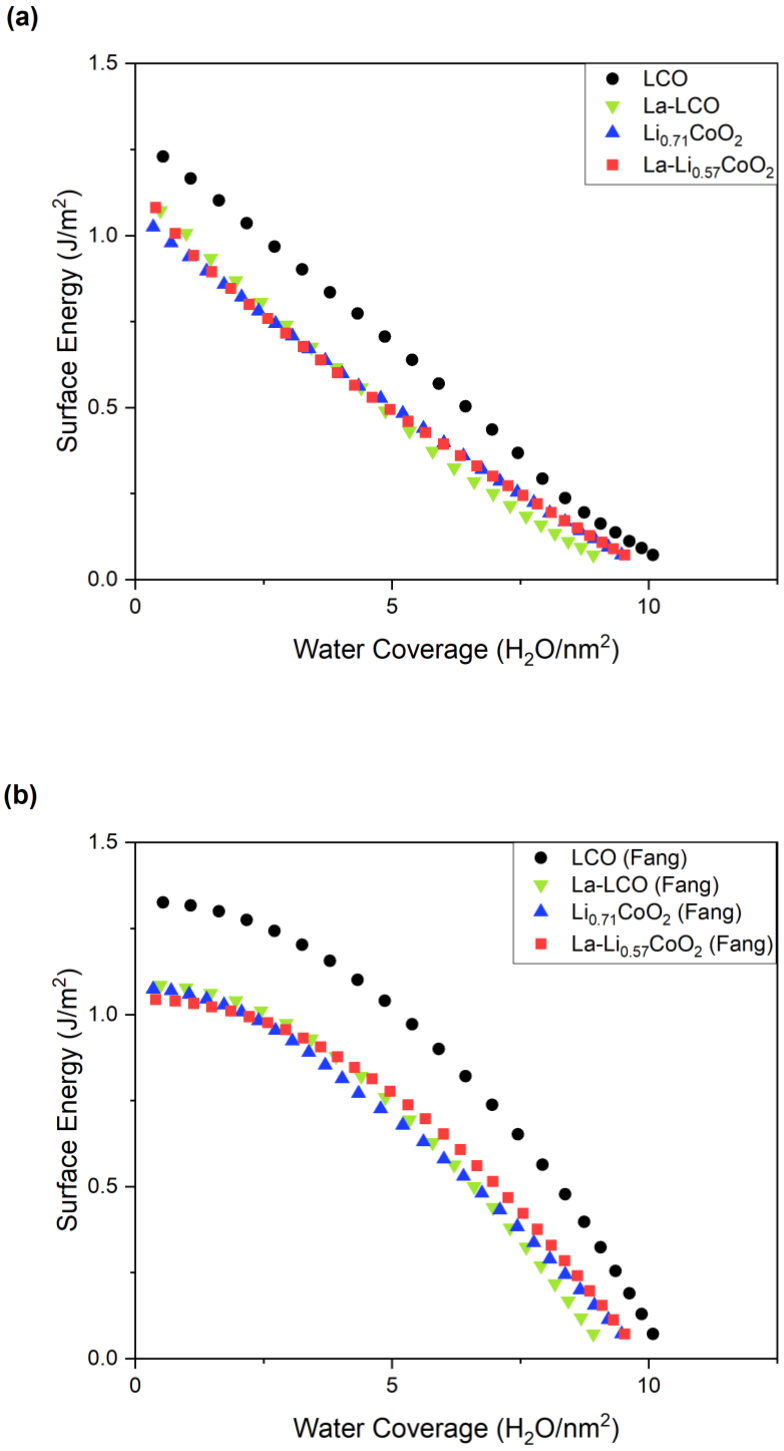

Figure 4.5. The measured surface energy of all four samples as a function of the water coverage for (a) the calorimetry method (**Equation 4**) and (b) the Fang method (**Equation 1**).

The surface energy measurements demonstrated the effectiveness of doping and the utility of using multiple models for surface energy calculations. The La-doped LCO had lower surface energies than the undoped LCO and confirmed the stabilization effect of the dopant segregation. Additionally, the water adsorption proved that the delithiated undoped LCO decreases in surface energy relative to the stoichiometric material while the La-doped nanoparticles have consistent surface energies upon delithiation. It might be argued that this surface energy reduction could be beneficial for the stabilization of the nanoparticles in the undoped case. However, lithium intercalation from the anode into the cathode is a crucial part of lithium ion battery operation and the capacity of a cathode material is proportional to the amount of available Li for intercalation.[36] If there are {001} surfaces that are no longer thermodynamically favorable sites for lithium intercalation, this could lead to a decrease in performance of the cell. This is a minimal issue in bulk LCO cathodes with low surface area, but the fraction of atoms located at or near surfaces in nanomaterials or even microscale increases significantly. The La stabilization of the surface energy could lead to a more reversible Li intercalation process and improve the long term cycling behavior of the cell, because the Li is thermodynamically stable enough to go back to the {001} surfaces. Capacity fading is a severe problem in nanomaterials and this framework of surface stabilization could improve their utility and application in lithium ion batteries.

Conclusion

The water adsorption measurements demonstrated a useful technique for quantifying the surface energies of nanoparticles and proved to be an effective model for screening doped materials. Both of the techniques using microcalorimetry and only water adsorption data corroborated the surface energy results showing a clear decrease in surface energy for 1 mol %

La-LCO compared to undoped LCO nanoparticles. Additionally, the adsorption data showed surface energy decreases upon delithiation to $Li_{0.71}CoO_2$ and confirmed the previous DFT results from Kramer and Ceder. However, La-doped materials delithiated to La-$Li_{0.57}CoO_2$ have consistent surface energy values compared to the fully stoichiometric LCO due to the stabilization effect of La segregation. The trends in these values also continued from the anhydrous state to the fully hydrated values converging to the surface tension of water. This La-doped stabilization effect could be used to enhance the long term cyclability of nanoscale lithium ion cathode materials and will be the focus of future work.

References

(1) Kim, T.; Song, W.; Son, D. Y.; Ono, L. K.; Qi, Y. Lithium-Ion Batteries: Outlook on Present, Future, and Hybridized Technologies. *J. Mater. Chem. A* **2019**, *7* (7), 2942–2964. https://doi.org/10.1039/C8TA10513H.

(2) Pender, J. P.; Jha, G.; Hyun Youn, D.; Ziegler, J. M.; Andoni, I.; Choi, E. J.; Heller, A.; Dunn, B. S.; Weiss, P. S.; Penner, R. M.; Buddie Mullins, C. Electrode Degradation in Lithium-Ion Batteries. *ACS Nano* **2020**, *14*, 59. https://doi.org/10.1021/acsnano.9b04365.

(3) Sotelo Martin, L. E.; Castro, R. H. R. Al Excess Extends Hall-Petch Relation in Nanocrystalline Zinc Aluminate. *J. Am. Ceram. Soc.* **2022**, *105* (2), 1417–1427. https://doi.org/10.1111/JACE.18176.

(4) Hammer, B.; Nørskov, J. K. Theoretical Surface Science and Catalysis—Calculations and Concepts. *Adv. Catal.* **2000**, *45* (C), 71–129. https://doi.org/10.1016/S0360-0564(02)45013-4.

(5) Bruce, P. G.; Scrosati, B.; Tarascon, J. M. Nanomaterials for Rechargeable Lithium Batteries. *Angew. Chemie - Int. Ed.* **2008**, *47* (16), 2930–2946.

https://doi.org/10.1002/ANIE.200702505.

(6) Okubo, M.; Hosono, E.; Kim, J.; Enomoto, M.; Kojima, N.; Kudo, T.; Zhou, H.; Honma, I. Nanosize Effect on High-Rate Li-Ion Intercalation in LiCoO2 Electrode. *J. Am. Chem. Soc.* **2007**, *129* (23), 7444–7452. https://doi.org/10.1021/ja0681927.

(7) Jo, M.; Hong, Y.-S.; Choo, J.; Cho, J. Effect of LiCoO2 Cathode Nanoparticle Size on High Rate Performance for Li-Ion Batteries. *J. Electrochem. Soc.* **2009**, *156* (6), A430. https://doi.org/10.1149/1.3111031/XML.

(8) Nagpure, S. C.; Babu, S. S.; Bhushan, B.; Kumar, A.; Mishra, R.; Windl, W.; Kovarik, L.; Mills, M. Local Electronic Structure of LiFePO4 Nanoparticles in Aged Li-Ion Batteries. *Acta Mater.* **2011**, *59* (18), 6917–6926. https://doi.org/10.1016/J.ACTAMAT.2011.07.043.

(9) Kirchheim, R. Reducing Grain Boundary, Dislocation Line and Vacancy Formation Energies by Solute Segregation. I. Theoretical Background. *Acta Mater.* **2007**, *55* (15), 5129–5138. https://doi.org/10.1016/J.ACTAMAT.2007.05.047.

(10) Bangham, D. H. THE GIBBS ADSORPTION EQUATION AND ADSORPTION ON SOLIDS. *Trans. Faraday Soc.* **1937**, *33*, 805–811.

(11) Nakajima, K.; Souza, F. L.; Freitas, A. L. M.; Thron, A.; Castro, R. H. R. Improving Thermodynamic Stability of Nano-LiMn2O4for Li-Ion Battery Cathode. *Chem. Mater.* **2021**, *33* (11), 3915–3925. https://doi.org/10.1021/ACS.CHEMMATER.0C04305/SUPPL_FILE/CM0C04305_SI_001.PDF.

(12) Leong, V. G. H.; Hong, S. S.; Castro, R. H. R. Improved Electrochemical Performance in Sc-Doped Nanocrystalline LiMn2O4. *Mater. Lett.* **2022**, *325*, 132824.

https://doi.org/10.1016/J.MATLET.2022.132824.

(13) Maram, P. S.; Costa, G. C. C.; Navrotsky, A. Experimental Confirmation of Low Surface Energy in LiCoO 2 and Implications for Lithium Battery Electrodes . *Angew. Chemie* **2013**, *125* (46), 12361–12364. https://doi.org/10.1002/ANGE.201305375.

(14) Ceder, G.; Van Der Ven, A. Phase Diagrams of Lithium Transition Metal Oxides: Investigations from First Principles. *Electrochim. Acta* **1999**, *45* (1), 131–150. https://doi.org/10.1016/S0013-4686(99)00199-1.

(15) Qian, D.; Hinuma, Y.; Chen, H.; Du, L. S.; Carroll, K. J.; Ceder, G.; Grey, C. P.; Meng, Y. S. Electronic Spin Transition in Nanosize Stoichiometric Lithium Cobalt Oxide. *J. Am. Chem. Soc.* **2012**, *134* (14), 6096–6099. https://doi.org/10.1021/ja300868e.

(16) Bikerman, J. J. Surface Energy of Solids. *Phys. Status Solidi* **1965**, *10* (1), 3–25. https://doi.org/10.1002/pssb.19650100102.

(17) Kendall, K.; Alford, N. M.; Birchall, J. D. A New Method for Measuring the Surface Energy of Solids. *Nature* **1987**, *325* (6107), 794–796. https://doi.org/10.1038/325794a0.

(18) Triantafyllou, G.; Angelopoulos, G. N.; Nikolopoulos, P. Surface and Grain-Boundary Energies as Well as Surface Mass Transport in Polycrystalline Yttrium Oxide. *J. Mater. Sci.* **2010**, *45* (8), 2015–2022. https://doi.org/10.1007/S10853-009-4013-7/TABLES/5.

(19) McHale, J. M.; Auroux, A.; Perrotta, A. J.; Navrotsky, A. Surface Energies and Thermodynamic Phase Stability in Nanocrystalline Aluminas. *Science (80-.).* **1997**, *277* (5327), 788–789. https://doi.org/10.1126/SCIENCE.277.5327.788/ASSET/3A6BDCD6-FC2E-4F3B-AC87-01630DAC7C8B/ASSETS/GRAPHIC/SE3275545004.JPEG.

(20) Castro, R. H. R.; Ushakov, S. V.; Gengembre, L.; Gouvêa, D.; Navrotsky, A. Surface Energy and Thermodynamic Stability of γ-Alumina: Effect of Dopants and Water. *Chem.*

Mater. **2006**, *18* (7), 1867–1872. https://doi.org/10.1021/CM052599D/ASSET/IMAGES/LARGE/CM052599DF00004.JPEG.

(21) Fang, X.; Li, B.; Chernyshova, I. V.; Somasundaran, P. Ranking of As-Received Micro/Nanoparticles by Their Surface Energy Values at Ambient Conditions. *J. Phys. Chem. C* **2010**, *114* (36), 15473–15477. https://doi.org/10.1021/JP105720Z/SUPPL_FILE/JP105720Z_SI_001.PDF.

(22) Asay, D. B.; Kim, S. H. Evolution of the Adsorbed Water Layer Structure on Silicon Oxide at Room Temperature. **2005**. https://doi.org/10.1021/jp053042o.

(23) Fang, X.; Li, B.; Wu, J.; Maldarelli, C.; Sokolov, J. C.; Rafailovich, M. H.; Somasundaran, P. Imaging and Estimating the Surface Heterogeneity on a Droplet Containing Cosolvents. *J. Phys. Chem. B* **2009**, *113* (29), 9636–9639. https://doi.org/10.1021/JP904272A/ASSET/IMAGES/LARGE/JP-2009-04272A_0002.JPEG.

(24) Schlangen, L. J. M.; Koopal, L. K.; Cohen Stuart, M. A.; Lyklema, J. Wettability: Thermodynamic Relationships between Vapour Adsorption and Wetting. *Colloids Surfaces A Physicochem. Eng. Asp.* **1994**, *89* (2–3), 157–167. https://doi.org/10.1016/0927-7757(94)80115-0.

(25) Adamson, A. W. An Adsorption Model for Contact Angle and Spreading. *J. Colloid Interface Sci.* **1968**, *27* (2), 180–187. https://doi.org/10.1016/0021-9797(68)90025-8.

(26) Castro, R. H. R.; Quach, D. V; Rock, P. A. Analysis of Anhydrous and Hydrated Surface Energies of Gamma-Al 2 O 3 by Water Adsorption Microcalorimetry. **2012**. https://doi.org/10.1021/jp309319j.

(27) Drazin, J. W.; Castro, R. H. R. Water Adsorption Microcalorimetry Model: Deciphering Surface Energies and Water Chemical Potentials of Nanocrystalline Oxides. **2014**. https://doi.org/10.1021/jp5016356.

(28) Bolis, V.; Fubini, B.; Marchese, " Leonard0; Martra, G.; Costat, D. Hydrophilic and Hydrophobic Sites on Dehydrated Crystalline and Amorphous Silicas. *J. CHEM. SOC. FARADAY TRANS* **1991**, *87* (3), 497–505.

(29) Castro, R. H. R. Interfacial Energies in Nanocrystalline Complex Oxides. *Curr. Opin. Solid State Mater. Sci.* **2021**, *25* (3), 100911. https://doi.org/https://doi.org/10.1016/j.cossms.2021.100911.

(30) Hasan, M. M.; Dholabhai, P. P.; Dey, S.; Uberuaga, B. P.; Castro, R. H. R. Reduced Grain Boundary Energies in Rare-Earth Doped MgAl2O4 Spinel and Consequent Grain Growth Inhibition. *J. Eur. Ceram. Soc.* **2017**, *37* (13), 4043–4050. https://doi.org/10.1016/J.JEURCERAMSOC.2017.04.073.

(31) Ihrig, M.; Finsterbusch, M.; Laptev, A. M.; Tu, C. H.; Tran, N. T. T.; Lin, C. A.; Kuo, L. Y.; Ye, R.; Sohn, Y. J.; Kaghazchi, P.; Lin, S. K.; Fattakhova-Rohlfing, D.; Guillon, O. Study of LiCoO2/Li7La3Zr2O12:Ta Interface Degradation in All-Solid-State Lithium Batteries. *ACS Appl. Mater. Interfaces* **2022**, *14* (9), 11288–11299. https://doi.org/10.1021/ACSAMI.1C22246.

(32) Pecharsky, V. K.; Zavalij, P. Y. *Fundamentals of Diffraction*; 2003.

(33) Patterson, A. L. The Scherrer Formula for X-Ray Particle Size Determination. *Phys. Rev.* **1939**, *56* (10), 978. https://doi.org/10.1103/PhysRev.56.978.

(34) Reimers, J. N.; Dahn, J. R. Electrochemical and In Situ X-Ray Diffraction Studies of Lithium Intercalation in Li x CoO2. *J. Electrochem. Soc.* **1992**, *139* (8), 2091–2097.

https://doi.org/10.1149/1.2221184/XML.

(35) Ohzuku, T.; Ueda, A. Solid-State Redox Reactions of LiCoO2 (R3m) for 4 Volt Secondary Lithium Cells. *J. Electrochem. Soc.* **1994**, *141* (11), 2972–2977. https://doi.org/10.1149/1.2059267/XML.

(36) Liu, C.; Neale, Z. G.; Cao, G. Understanding Electrochemical Potentials of Cathode Materials in Rechargeable Batteries. *Mater. Today* **2016**, *19* (2), 109–123. https://doi.org/10.1016/J.MATTOD.2015.10.009.

(37) Takahashi, Y.; Kijima, N.; Dokko, K.; Nishizawa, M.; Uchida, I.; Akimoto, J. Structure and Electron Density Analysis of Electrochemically and Chemically Delithiated LiCoO2 Single Crystals. *J. Solid State Chem.* **2007**, *180* (1), 313–321. https://doi.org/10.1016/J.JSSC.2006.10.018.

(38) Gupta, R.; Manthiram, A. Chemical Extraction of Lithium from Layered LiCoO2. *J. Solid State Chem.* **1996**, *121* (2), 483–491. https://doi.org/10.1006/JSSC.1996.0067.

(39) Furushima, Y.; Yanagisawa, C.; Nakagawa, T.; Aoki, Y.; Muraki, N. Thermal Stability and Kinetics of Delithiated LiCoO2. *J. Power Sources* **2011**, *196* (4), 2260–2263. https://doi.org/10.1016/J.JPOWSOUR.2010.09.076.

(40) Venkatraman, S.; Choi, J.; Manthiram, A. Factors Influencing the Chemical Lithium Extraction Rate from Layered LiNi1-y-ZCoyMnzO2 Cathodes. *Electrochem. commun.* **2004**, *6* (8), 832–837. https://doi.org/10.1016/J.ELECOM.2004.06.004.

(41) Khalfaoui, M.; Knani, S.; Hachicha, M. A.; Lamine, A. Ben. New Theoretical Expressions for the Five Adsorption Type Isotherms Classified by BET Based on Statistical Physics Treatment. *J. Colloid Interface Sci.* **2003**, *263* (2), 350–356. https://doi.org/10.1016/S0021-9797(03)00139-5.

(42) Quach, D. V.; Bonifacio, A. R.; Castro, R. H. R. Water Adsorption and Interface Energetics of Zinc Aluminate Spinel Nanoparticles: Insights on Humidity Effects on Nanopowder Processing and Catalysis. *J. Mater. Res.* **2013**, *28* (15), 2004–2011. https://doi.org/10.1557/JMR.2013.192.

(43) Huang, Y.; Ling, C.; Jin, M.; Du, J.; Zhou, T.; Wang, S. Water Adsorption and Dissociation on Ni Surface: Effects of Steps, Dopants, Coverage and Self-Aggregation. *Phys. Chem. Chem. Phys.* **2013**, *15* (41), 17804–17817. https://doi.org/10.1039/C3CP53644K.

(44) Li, X.; Wang, B.; Zhang, T. Y.; Su, Y. Water Adsorption and Dissociation on BaTiO3 Single-Crystal Surfaces. *J. Phys. Chem. C* **2014**, *118* (29), 15910–15918. https://doi.org/10.1021/JP5051386/ASSET/IMAGES/LARGE/JP-2014-051386_0011.JPEG.

(45) Cherkashinin, G.; Jaegermann, W. Dissociative Adsorption of H2O on LiCoO2 (00l) Surfaces: Co Reduction Induced by Electron Transfer from Intrinsic Defects. *J. Chem. Phys.* **2016**, *144*, 184706. https://doi.org/10.1063/1.4948610.

(46) Kim, Y. Water Adsorption on the Surface of Ni- and Co-Based Layer-Structured Cathode Materials for Lithium-Ion Batteries. *Int. J. Quantum Chem.* **2018**, *118* (14). https://doi.org/10.1002/QUA.25591.

(47) Ma, Y.; Castro, R. H. R.; Zhou, W.; Navrotsky, A. Surface Enthalpy and Enthalpy of Water Adsorption of Nanocrystalline Tin Dioxide: Thermodynamic Insight on the Sensing Activity. *J. Mater. Res.* **2011**, *26* (7), 848–853. https://doi.org/10.1557/JMR.2010.97.

(48) Wu, L.; Dey, S.; Gong, M.; Liu, F.; Castro, R. H. R. Surface Segregation on Manganese Doped Ceria Nanoparticles and Relationship with Nanostability. *J. Phys. Chem. C* **2014**,

118 (51), 30187–30196. https://doi.org/10.1021/JP508663P/ASSET/IMAGES/LARGE/JP-2014-08663P_0008.JPEG.

(49) Pérez-Hernández, G.; Schmidt, B. Anisotropy of the Water–Carbon Interaction: Molecular Simulations of Water in Low-Diameter Carbon Nanotubes. *Phys. Chem. Chem. Phys.* **2013**, *15* (14), 4995–5006. https://doi.org/10.1039/C3CP44278K.

(50) Yamada, T.; Tamamori, S.; Okuyama, H.; Aruga, T. Anisotropic Water Chain Growth on Cu(110) Observed with Scanning Tunneling Microscopy. **2006**. https://doi.org/10.1103/PhysRevLett.96.036105.

(51) Hasan, M. M.; Dey, S.; Nafsin, N.; Mardinly, J.; Dholabhai, P. P.; Uberuaga, B. P.; Castro, R. H. R. Improving the Thermodynamic Stability of Aluminate Spinel Nanoparticles with Rare Earths. *Chem. Mater.* **2016**, *28* (14), 5163–5171. https://doi.org/10.1021/ACS.CHEMMATER.6B02577/ASSET/IMAGES/ACS.CHEMMATER.6B02577.SOCIAL.JPEG_V03.

(52) Kramer, D.; Ceder, G. Tailoring the Morphology of LiCoO2: A First Principles Study. *Chem. Mater.* **2009**, *21* (16), 3799–3809. https://doi.org/10.1021/cm9008943.

(53) Hausbrand, R.; Cherkashinin, G.; Ehrenberg, H.; Gröting, M.; Albe, K.; Hess, C.; Jaegermann, W. Fundamental Degradation Mechanisms of Layered Oxide Li-Ion Battery Cathode Materials: Methodology, Insights and Novel Approaches. *Mater. Sci. Eng. B* **2015**, *192* (C), 3–25. https://doi.org/10.1016/J.MSEB.2014.11.014.

(54) Hu, L.; Xiong, Z.; Ouyang, C.; Shi, S.; Ji, Y.; Lei, M.; Wang, Z.; Li, H.; Huang, X.; Chen, L. Ab Initio Studies on the Stability and Electronic Structure of LiCoO 2 (003) Surfaces. *Phys. Rev. B - Condens. Matter Mater. Phys.* **2005**, *71* (12), 125433.

https://doi.org/10.1103/PhysRevB.71.125433.

Chapter 5: Conclusion and Future Works

Conclusion

The interfacial stability of LCO nanoparticles was improved through dopant segregation utilizing computational and experimental approaches. Molecular static calculations developed an energetic map of segregation potentials for divalent, trivalent, and quadrivalent dopants (Chapter 2). The calculations also demonstrated the dependence of the dopant segregation energy on the specific structure and chemistry of the interface for the four structures studied (grain boundaries and surfaces). This methodology informed the synthesis protocol for La-doped LCO nanoparticles, as lanthanum is a dopant with high segregation energy to all interfaces. La-doped and undoped LCO nanoparticles were synthesized and confirmed to have La segregation to surfaces and grain boundaries. In Chapter 3, the interfacial energies were determined from measuring the heat released during microstructural evolution in a DSC. The results showed a reduction in surface energy for La-doped LCO and confirmed the stabilization effect of dopant segregation. The La also provided resistance to coarsening and the doped nanoparticles maintained high specific surface areas with smaller crystallite sizes. The delithiated nanoparticles were studied with a water adsorption apparatus and showed a decrease in surface energy upon removal of lithium from undoped nanoparticles. Contrastingly, the La-doped nanoparticles maintained a similar surface energy after delithiting to Li/Co levels of 0.57. This surface stabilization could play a critical role in the application of nanoscale cathode materials in lithium ion batteries. The dopant segregation helps create a more stable energy landscape for nanoparticles that could help reduce some of the degradation mechanisms seen in batteries (transition metal dissolution, coarsening, intergranular cracking, etc.) causing capacity fading. Overall, the thermodynamic stability of LCO nanoparticles was improved and further

understanding of nanoparticle stability could help expand the application of nanostructured cathode materials.

Future Works

This work can be utilized to explore a number of new directions in the interfacial design of nanomaterials. Although some initial electrochemical studies were performed with promising results, they were not included here and need to be explored further. Electrochemical cycling experiments could demonstrate how dopants reduce capacity fading and improve the long term cycling behavior of batteries. Additionally, it could show us how different dopants impact the charge transfer resistance of lithium in the battery. For example, large ionic radius dopants like lanthanum might provide thermodynamic stability, but also cause more resistance for lithium diffusion due to the large size of the dopant. In this case, a smaller dopant like scandium might provide some interfacial stability and resistance to coarsening, while having less of an impact on the cycling behavior.

Similar to the electrochemical work, designing ionically and electronically conductive grain boundaries could greatly expand the use of nanomaterials. Many researchers are expanding into solid state battery systems because of their safety features, but grain boundaries can provide resistance to charge transfer. A more in depth study into how dopants can change the conductivity and electronic nature of the grain boundaries to facilitate lithium diffusion and electron flow would help progress the understanding of grain boundary structures. Some molecular dynamics and Monte Carlo simulations could help with designing specific surfaces and grain boundaries. This study was limited by using a Buckingham-Coulomb potential with set oxidation states of the Co and O atoms in order to find compatible potentials for the ten dopants studied. A subset of dopants studied with a charge transfer model would help take into account

the electronic nature of the Co and O to capture their oxidation state changes when interfaced with dopants. Delithiated structures and the effect of doping could also be studied with a charge transfer model to see interfacial and structural reconstructions as a function of lithium content.